Neutron and Synchrotron X-ray Studies of Magnetic Nanostructures

Thesis submitted in accordance with the requirement of
the University of Liverpool for the degree of Doctor in Philosophy

by

Raymond Fan

Oliver Lodge Laboratory

April 2008

Neutron and Synchrotron X-Ray Studies of Magnetic Nanostructures

Raymond Fan

Thesis for submission for the degree of Doctor of Philosophy

April 2008

Structural and magnetic studies of magnetic nanostructures have been performed using x-ray diffraction (XRD), x-ray reflectivity (XRR), polarised neutron reflectivity (PNR), small angle neutron scattering (SANS), transmission electron microscopy (TEM) and bulk magnetometry (SQUID) techniques.

XRD, XRR and TEM were employed to determine the physical structure of Fe/MgO multilayers. The crystalline coherence was confined within two bilayers, and a wavy roughness was observed using TEM. The magnetic coupling between Fe blocks was studied using PNR and SQUID magnetometry. FM coupling was found for thick (20Å) MgO spacer layers in the virgin state. However, unexpectedly, no magnetic correlations were found for thin MgO (6 Å) in the virgin state, and frozen in FM moments were observed when returned to the coercive state.

Record 40% room temperature giant magnetoresistance (GMR) can be obtained by heat treating nanogranular Co/Ag alloys, and the dependence of the GMR on annealing conditions is complex. Structural and magnetic studies were performed using XRD and SANS. The results show that the complex behavior is due to a phase separation between the two materials at low annealing temperature, and an agglomeration of the nanoparticles at higher temperature.

The effect of oxidation on Co nanoparticles in a Ag matrix was examined using SANS and SQUID magnetometry. Oxidation creates a CoO shell around the Co nanoparticles, and at the same time removes FM Co magnetic impurities from the matrix. This has an important effect on the magnetic interactions. At a low level of oxidation the removal of impurities reduces the RKKY-like interactions between nanoparticles, and as the CoO shell reaches a critical thickness exchange bias takes over.

Ordered arrays of Co and Fe_2O_3 nanoparticles were studied using TEM and SANSPoL. Although hexagonal ordering is obtained over small areas using self-assembly techniques, the statistical averaging of SANS reveals only short-range order from hard spheres. The magnetic structures determined using SANPoL explain why there is exchange bias and magnetic anisotropy for Co, but not for Fe_2O_3.

Acknowledgments

It is finally the end of a wonderful experience. I would love to say, I did it all by myself. Unfortunately, this is so far from the truth. I have had wonderful help along the way and it has been an unbelievable 3 years. To whose whom I have failed to mention and to those I have not given the proper credit; I apologise. What I write here cannot come close to how I feel as to your contribution and efforts.

The first and the most important person I wish to thank is my supervisor, Jon Goff. If it not for Jon, I highly doubt that I could have completed this thesis. He has given me the freedom to test out some of my "innovative" ideas whilst keeping me on track on the thesis work. I cannot thank him enough for his incredible patience and I have enjoyed every second working with him.

I would like to thank Simon Lee for hours of discussion on physic as well as many other interesting subjects. He has helped me through almost everything in my P.H.D.; from experiment analysis to computing, and anything that crossed our minds at the time. Additionally there were his gentle kicks at the "proper part" of my body; in attempt to remind me to work. Without him I am almost certain that I will still be working on my analysis at this moment.

A special thank to Jose de Toro, who has taught me many basic concepts in nano-scale magnetism as well as some of the most important words in Spanish. My short time with him was highly enjoyable.

Then there is the office; everyone in there has made my experience much more enjoyable. Who can forget the endless beautiful stories from Johnny-Long-Lunch. Ben has been an excellent fun to be around with, the odd drinking section and the world class darts sections. Also there is Michael; I must thank him for all the lessons on many different subjects. Alex and Andrea have kept me sane throughout my time in the office as they are some of the most cheerful persons I have ever met. A special thank to Markos and Keith who always willing to help for any problems I may have. And I must apologise to Dave for taking so much of his desk space.

Out of the workplace I must hank all my flatmates for being so wonderful and they have given me a second place to call "home". Special thanks to Wilson who took care of many things for me when I was away for experiment as well as being such a wonderful distraction from time to time.

Finally, I must thank Mun and Dad for being wonderfully supportive throughout. Last but not least, a big thanks to my sister, as she always reminds me,"what are you going to do without your sister"?

Contents

Chapter 1

Introduction

1.1 Introduction

In recent years the development of nanoscale fabrication techniques has opened up the field of magnetoelectronics and enabled the creation of a new type of electronic device. For example, the growth of single-crystal thin films using molecular beam epitaxy (MBE) allows the tailoring of physical properties, since the artificial periodicity can be controlled on the atomic scale. The most notable application is the spin valve, which is now employed in the read heads in computers. The ability to produce nanogranular samples by sputtering and ordered arrays of magnetic nanoparticles using self assembly, has led to further applications in ultrahigh-density magnetic recording media and medicine.

The technology of the 20^{th} century was dominated by semiconductors, which rely primarily on the charge of the electron. However, the revolutionary devices now employed in magnetic recording media depend on the spin as well as the charge of the electron. The two physical phenomena of most importance for these applications are giant magnetoresistance and exchange bias. In both cases the device performance depends on the details of the magnetic ordering on an atomic scale, and on the nature of any interactions between components.

In this thesis I employ advanced neutron scattering techniques to examine the magnetic ordering and interactions in nanostructures that are very close to those actually used in devices, and the results provide a better understanding of the performance.

1.2 Fabrication of nanostructures

MBE was developed in the early 1970s as a way of producing high-purity epitaxial layers. In MBE elements are deposited onto a heated crystalline substrate in the form of 'molecular beams'. The 'molecular beams' are typically obtained from thermally evaporated elemental sources. In order to obtain high-purity layer the entire process is done in an ultra-high vacuum environment. Furthermore the beam can be shuttered in a fraction of a second, enabling an atomically sharp transition from one material to the other. MBE enables the production of high quality single-crystal and thin films making it ideal for scattering studies.

Sputtering is a process where atoms are ejected from a solid target due to bombardment of energetic ions. Some of these ejected atoms are ionized and they are accelerated in an electric field onto a substrate to form a thin film. For most sputtering growth the chamber is filled with an inert gas such as argon. However if a reactive gas such as oxygen is introduced into the chamber, chemical reaction can occur on the target surface, in-flight or on the substrate and new compounds can be grown on the substrate. One advantage of sputter deposition over MBE is that even the highest melting point materials are easily sputtered while evaporation of these materials can be problematic. However, sputtered films usually have poor crystallinity, and it is very difficult to an deposit insulator.

Nanoscale structures are often difficult to fabricate in large quantities, and self assembly offers a promising method of producing nanoscale devices without the need of manipulate the nano-scale structure itself. Self assembly is a term widely used in chemistry and materials science to describe processes where a disordered system forms an organized structure or pattern as a consequence of specific local interactions among the components without external interference. Self assembly covers a wide range of fabrication techniques including molecular self assembly, self assembly through lithography and self assembly of nanoparticles via evaporation.

1.3 Giant magnetoresistance (GMR)

GMR is a type of magnetioresistance (MR) effect observed in interfacial structures composed of ferromagnetic and nonmagnetic layers. For sandwich structures the GMR effectively measures the difference in angle between the two magnetisations in the magnetic layers. Parallel alignment gives a low resistance while antiparallel alignment produces a higher resistance. Figure 1.3.1 shows the measurements of Grunberg *et al.* [1] and Fert *et al.* [2], and the results clearly demonstrate a dramatic change in resistance when a small field is applied for sandwich structures and multilayers, respectively. The change in resistance can be understood in the following simplified picture. Figure 1.3.2 shows both the spin-up and spin-down electron band structure for two FM iron layers separated by a nonmagnetic layer. Fermi's golden rule states that scattering rates are proportional to the density of states at the state being scattered into. As spin-up and spin-down electrons have different densities of states, the spin-up and spin-down electrons experience different scattering (resistance). Simple consideration of electrical resistance for spin-up and spin-down electrons in figure 1.3.3 shows there is a clear difference between the applied field and zero field.

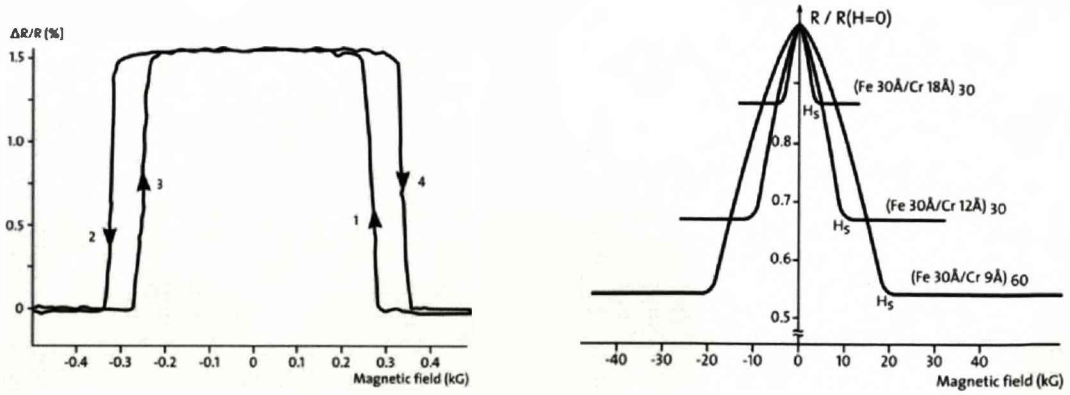

Figure 1.3.1: Magnetoresistance measurements taken from Refs [1,2] showing variation of resistance as a function of applied field.

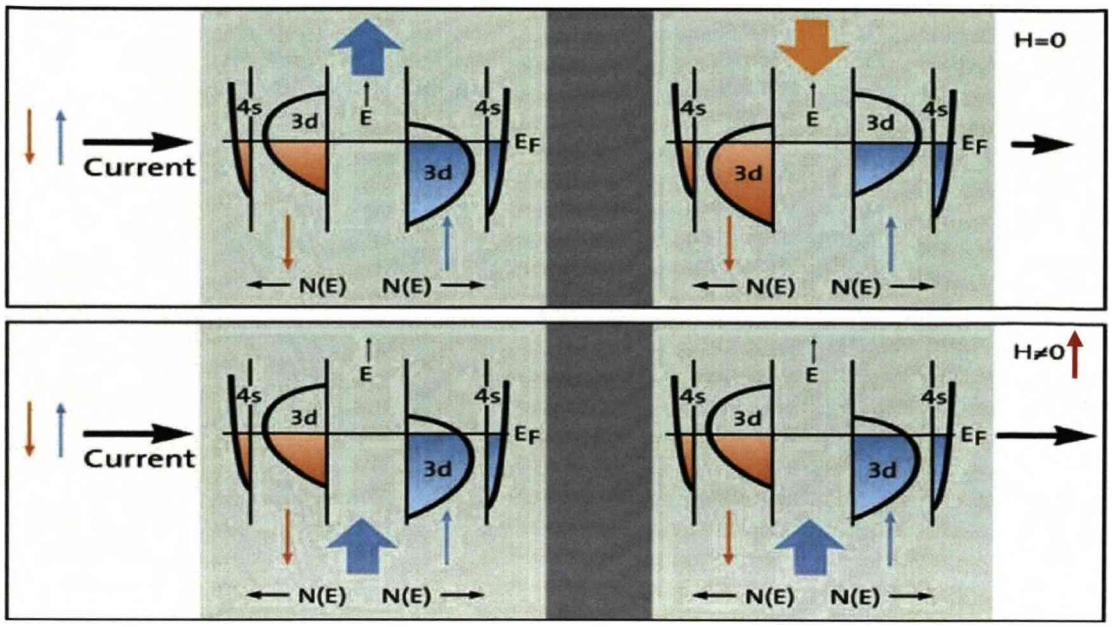

Figure 1.3.2: Schematic illustration of the band structure of a trilayer system with and without any applied field, thin arrows represent spin-up and spin-down current, while large arrows are the magnetization direction of the Fe layer [7].

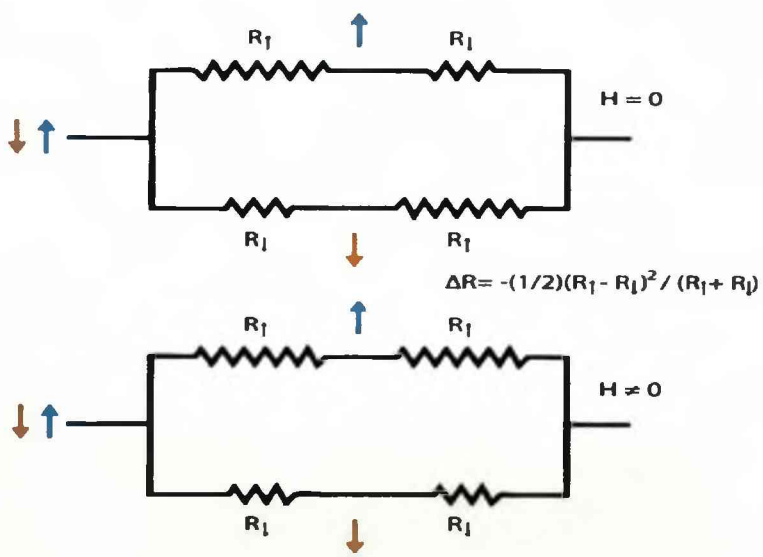

Figure 1.3.3: Same system as figure 1.2.2. $R_{\uparrow}$ and $R_{\downarrow}$ represent the resistance parallel and anti-parallel to the magnetization direction slowing a clear difference between the two [Reference].

Since the discovery of GMR by Baibich *et al.* [2] in 1988, GMR effect quickly found its way into many modern applications, for example, it is now employed in

magnetic read heads and magnetoresistive random access memory (MRAM). Many of these applications require one of the two FM layers to be fixed in one known direction, while the other layer remains free. Often in magnetic devices the pinning is provided via the effect of exchange bias. Exchange bias was first observed by Meiklejohn and Bean [3] in fine cobalt particles with a cobalt oxide shell. Exchange anisotropy occurs between AF and FM interfaces where the AF layer causes a shift in the magnetization curve of the FM layer as shown in figure 1.3.4. Finally, to complete this section, a picture of a spin valve device is shown in Figure 1.3.5, it consists of a top free FM layer, a spacer layer and a pinned FM layer.

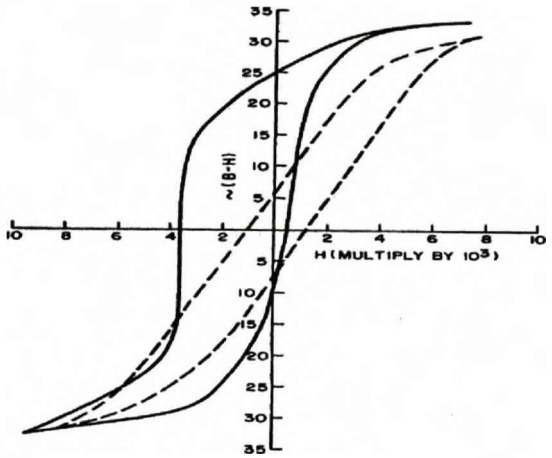

Figure 1.3.4: Hysteresis loops taken from Ref [3], showing a clear shift of the hysteresis loop due to exchange anisotropy.

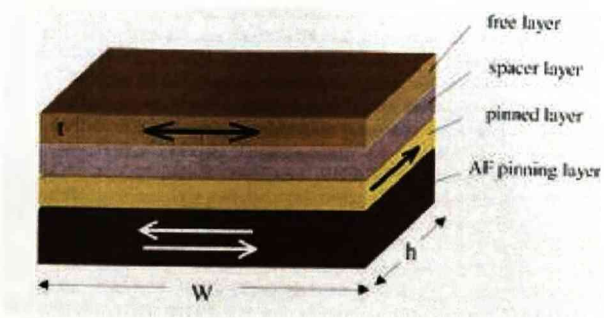

Figure 1.3.5: Schematic diagram of a spin valve device taken from Ref [4].

1.4 Neutron scattering

The neutron interacts with nuclei via the strong force and, since it carries spin, with magnetic moments, including those arising from the electron charge cloud around an atom. Therefore, neutron scattering provides magnetic and structural information simultaneously, and this is very difficult to achieve with other techniques. For example, polarized neutron reflectivity (PNR) can directly measure the magnetization directions of individual FM layers. Figure 1.4.1 is a set of PNR data taken by Lee *et al.* on Fe/Mn multilayers [5]. It shows how the magnetization direction of the Fe layers can be obtained using PNR. A FM coupled structure has a reflectivity profile with the same periodicity as the pure structural case, but an AF coupled structure results in extra reflectivity peaks at the half wave-vector transfer position with respect to the structural peaks.

Neutron scattering is not limited to reflection geometry. In transmission geometry small angle neutron scattering (SANS) can be performed, and SANS is an excellent way of probing magnetic material in the nanoscale range. Figure 1.4.2 shows Co nanoparticles system studied using SANS where well defined Bragg reflections were observed due to the hexagonal ordering of nanoparticles [6]. Furthermore, SANS also gives detailed information on the shape and size of the nanoscale components.

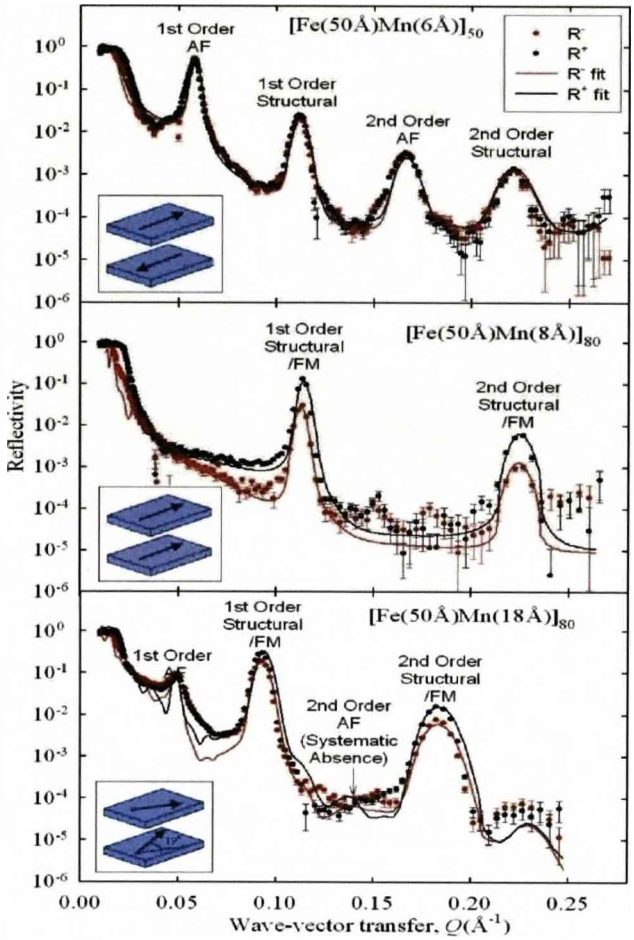

Figure 1.4.1: Reflectivity data from Fe/Mn multilayers studies, showing clear difference for three difference Fe block alignments, from Ref [5].

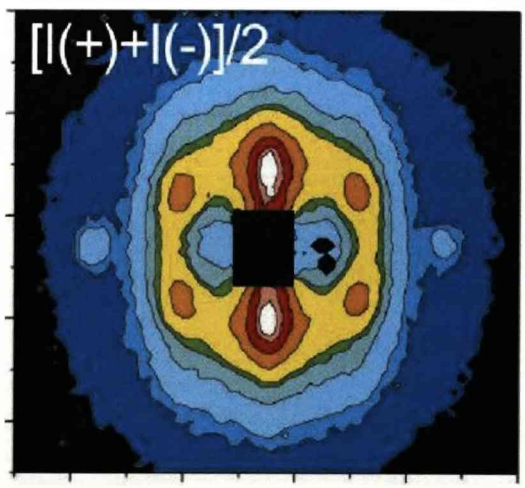

Figure 1.4.2: SANS measurement of field induced ordering of Co nanoparticles, taken from Ref [6].

1.5 Plan of thesis

Chapter 2 will focus on the materials contained within the nanoscale systems studied in this thesis. The magnetic and structural properties of the bulk phase and some of the fundamental magnetism relating to these systems are presented. Chapter 3 is a summary of the experimental techniques used in this thesis, including both theoretical concepts of the techniques used in this work and experimental considerations. Chapter 4 describes detailed PNR and x-ray investigations of MBE grown Fe/MgO multilayers. This is a new type of *tunneling* magnetoresistance (TMR) junction that shows a MR ratio over 200%. Chapters 4 and 5 include studies of Co/Ag and Co-CoO/Ag nanogranular systems, respectively. Both systems are grown using a simple rf sputtering technique, with the latter exposed to a reactive oxidizing atmosphere. Chapter 4 concerns the effect of annealing on GMR ratio, and Chapter 5 concentrates on the formation of an exchange-biasing shell. In these chapters we employed SANS together with SQUID measurements to understand the details of the magnetic structure for the two systems. Chapter 7 includes the studies of self-assembled Co and Fe_2O_3 nanoparticle systems. This section examines the nature of the long-range ordering of these nanoparticles using TEM and SANS, and the magnetic structures are determined using SANSPoL. Finally, Chapter 8 contains a summary of all the findings in this thesis, and considers the future outlook.

Bibliography

[1] G.Binasch, P. Grunberg, F. Saurenbach, and W. Zinn, phys. Rev. B 39, 4828 (1989)

[2] M.N. Baibich, J.M. Broto, A. Fert, F.Nguyen van Dau, F. Petroff, P. Eitenne, G. Creuzet, A. Friederich, and J. Chazelas, Phys. Rev. Lett. 61, 2472 (1988)

[3] W.H. Meiklejohn and C. P. Bean, Phys Rev. 102, 1413 (1956)

[4] http://www.tcd.ie/Physics/Magnetism/Research/halfmetals.php

[5] S.J. Lee, J. P. Goff, G. J. Mcintyre, R. C. C. Ward, S. Langridge, T. Charlton, R. Dalgliesh and D Mannix, Phys. Rev. Lett. 99, 037204 (2007)

[6] A. Wiedenmann, A. Hoell, M. Kammel, and P. Boesecke, Phys. Rev. E 68, 031203 (2003)

[7] http://nobelprize.org/nobel_prizes/physics/laureates/2007/

Chapter 2

Magnetism and magnetic coupling

2.1 Introduction

In this thesis the main focus is on the combination of transition metals and nonmagnetic materials in nanoparticle assemblies and single-crystal multilayers. Both systems have highly promising potential applications and, therefore, the understanding of their magnetic properties becomes extremely important. In order to understand the behaviour of these systems it is necessary to first examine the structural and magnetic properties of the elements in their bulk form. Thus I shall begin this chapter with an overview of magnetism in transition metals. This is followed by a review of the magnetic coupling in multilayers, and a brief discussion of magnetic interactions in nanoparticle arrays.

Electrons are spin ½ fermions and, therefore, they obey the Pauli Exclusion Principle, so that no electron can occupy the same quantum state. Therefore electrons below the highest energy level are paired up in electronic orbitals, with equal and opposite spin moment. Magnetism requires one or more unpaired electrons to give a net moment. For an isolated atom, the magnetic moment is given by:

$$\mu = -g_j \mu_B J \qquad (2.1.1)$$

where J is the total angular momentum, which is a sum of the orbital angular momentum L and spin angular momentum S. In an atom electrons tend to occupy energy levels so that the total energy is at a minimum and Hund's rules can be used to gain a value of J for a free atom. g_j is the Landé factor which can be calculated from

the values of S and L. The typical size of the electronic magnetic moment is given by the Bohr magneton μ_B :

$$\mu_B = \frac{eh}{4\pi m} = 9.27 \times 10^{-24} J/T \quad . \tag{2.1.1}$$

In general Hund's rules can be used to determine the value of J and, hence, the magnetic moment of free atoms. However magnetic atoms hardly ever exist on their own, and the effect of neighbouring atoms can play an important part. For example, in transition metals crystal field effects are much stronger than the spin-orbit interactions leading to Hund's third rule. The first two rules maximise S and L in order to minimise the Coulomb energy, and these are obeyed. However, Hund's third rule relies on the spin-orbit interaction to predict the value of J, and the intervention of the crystalline electric field prevents the identification of the correct ground state for transition metals.

One can distinguish between two different types of magnetism, itinearant and localized. Localized magnetism is well described by Hund's rules together with crystal field correction. However interactions can have profound effect on the magnetic behaviour of a system, one of which is itinearant magnetism. Itinearant magnetism is caused by the exchange interaction between electrons. One useful model for itinerant magnetism is the Stoner model. For a system with a finite magnetization $M \neq 0$ the energy band for spin up and spin down electrons are spitted and the energy of the electrons in this band is given by:

$$E_B = \int_0^{E_\uparrow} E D_s(E) dE + \int_0^{E_\downarrow} E D_s(E) dE - \frac{I}{4}(N_\uparrow - N_\downarrow)^2 \tag{2.1.2}$$

where N is the total number of electrons, $N=N_\uparrow+N_\downarrow$ and I is the Stoner exchange parameter, which describes the exchange interaction between electrons. Taking the definition of spin polarization:

$$R = \frac{N^\uparrow - N^\downarrow}{N}, \tag{2.1.3}$$

in the case where the splitting is small, $D_s(E)$ can be replace by $D_s(E_F)$ one gets:

$$E_B = \frac{N^2}{4D_s(E_F)} R^2 - \frac{I}{4}(N_\uparrow - N_\downarrow)^2 \qquad (2.1.4)$$

Replacing $(N_\uparrow - N_\downarrow)^2$ by $R^2 N^2$:

$$E_B = \frac{N^2}{4}\left[\frac{1}{D_s(E_F)} - I\right]R^2 \qquad (2.1.5)$$

Examination of equation (2.1.5) shows that spontaneous magnetization ($R \neq 0$) result in a reduction in total energy if

$$D_s(E_F)I \geq 1. \qquad (2.1.6)$$

This condition is known as the Stoner criterion for ferromagnetism and it arises due to the strong exchange interaction between electrons [13,14].

2.2 Transition metal magnetism

The term "transition metals" refers to the three rows of elements in the periodic table from the alkali earths to the noble metals. The "3*d* elements" are the first row of transition metals (Sc-Zn). As a consequence of the partial filling of their 3*d* bands leading to unpaired electrons, most of them exhibit magnetism.

The 3*d* elements have an electronic shell of the form $[^{18}\text{Ar}]3d^n4s^2$ where *n* is 1 for Scandium and 10 for Zinc. The conduction band is formed by the 4*s* electrons. Furthermore the 3*d* electrons form the valence electrons for chemical bonding. Therefore oxidation has a dramatic effect on the magnetic properties of the 3*d* elements. The room temperature crystal properties of the bulk elements are summarised in table 2.2.1.

The 3*d* unfilled energy states are responsible for transition metal magnetism, as the *d*-band lies high up in the conduction band and extends through the Fermi energy. This is narrow in comparison to the 4*s* band, which is broad and free electron-

like in behaviour, therefore the *d* band is very different to that from a spherical nearly free electron model.

Neighbouring atoms tend to interact via direct exchange interactions. As shown in table 2.2.1 the transition metals adopt a simple parallel/anti-parallel arrangement of spins, as a consequence of the narrow 3*d* bands.

Element	3d e	Crystal structure	Lattice Parameter a(Å)	Lattice Parameter c(Å)	Magnetic structure
Sc	1	HCP	3.309	5.273	AF
Ti	2	HCP	2.951	4.686	AF
V	3	BCC	3.303	3.303	AF
Cr	5	BCC	2.890	2.890	AF
Mn	5	Cubic	2.890	2.890	AF
Fe	6	BCC	2.865	2.865	FM
Co	7	HCP	2.506	4.066	FM
Ni	8	FCC	3.520	3.520	FM
Cu	10	FCC	3.615	3.615	NM
Zu	10	HCP	2.665	4.947	NM

Table 2.2.1: Room temperature properties of bulk 3d-transition metals. AF, FM and NM denotes anti-ferromagnetic, ferromagnetic and non-magnetic respectively.

2.3 Magnetic interaction

Magnetic dipolar interaction

The simplest interaction between two magnetic moments is the dipolar interaction. Two magnetic dipoles μ_1 and μ_2 separated by r have an energy equal to

$$E = \frac{\mu_0}{4\pi r^3}\left[\mu_1 \cdot \mu_2 - \frac{3}{r^2}(\mu_1 \cdot r)(\mu_2 \cdot r)\right]. \qquad (2.3.1)$$

The dipolar interaction depends strongly on the separation and the relative angle between the two dipole moments. However, the order of magnitude can readily be estimated using the first term. Thus the energy of interaction for an ion of moment 1 μ_B separated from its neighbour by 1Å is of order 1K. Since ordering temperatures of transition metals are of order 1000K other types of exchange interaction are required. In contrast to these exchange interactions the dipolar interactions are long ranged and, therefore, for large regions of ferromagnetic ions the dipolar contribution eventually becomes important.

Direct exchange interaction

Exchange interactions are quantum mechanical effects and they are the consequence of the Pauli Exclusion Principle and the Coulombic energies. If the electrons of neighbouring atoms interact via an exchange interaction via the overlap of their wavefunctions, this is known as direct exchange. The direct exchange interaction Hamiltonian is given as:

$$H_{ex} = -\frac{1}{2}\sum_{ij} I(R_i - R_j) J_i \cdot J_j \qquad (2.3.2)$$

where J_i is the total angular momentum at position i interacted with J_j at position j through an exchange integral $I(R_i\text{-}R_j)$ between the two positions. For positive values of $I(R_i\text{-}R_j)$ the neighbouring atoms are aligned parallel to each other, and anti-parallel if the value of $I(R_i\text{-}R_j)$ is negative. In transition metals, because the $3d$ orbitals extend far from the nucleus, the effect of direct exchange is important for materials like Fe, Co and Ni.

Indirect exchange interaction

In metals the exchange interaction between ions can also propagate through the conduction electrons. A localized magnetic moment spin-polarizes the conduction electrons and the polarization couples to a neighbouring localized magnetic moment at a distance r away. This exchange interaction is indirect as it does not directly interact with the neighbouring atoms. This type of exchange was first proposed by Ruderman and Kittel[1] and later extended by Kasuya [2] and Yosida [3], and the theory is now generally known as the RKKY interaction. The interaction is characterised by a coupling coefficient, j, given by

$$j(R_i - R_l) = 9\pi\left(\frac{j^2}{\varepsilon_F}\right)F(2k_F|R_i - R_l|) \qquad (2.3.3)$$

where k_F is the electron wave vector at the Fermi surface, R_i is the lattice position of the spin moment, ε_F is the Fermi energy and

$$F(x) = \frac{x\cos x - \sin x}{x^4}. \qquad (2.3.4)$$

In the RKKY interaction one moment produces an oscillatory magnetization of the electron gas which can interact with a second moment, the exchange coefficient, j is shown in figure 2.3.1. The interaction is longer range than direct exchange, and can be ferromagnetic or anti-ferromagnetic depending on the distance between the two moments.

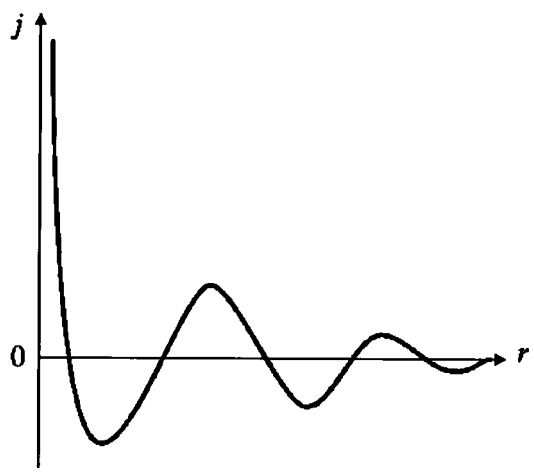

Figure 2.3.1: RKKY exchange coefficient as a function of distance. Picture taken from.

Crystal fields

The Crystal field is an electric field formed by the distribution of charge around the atoms in a crystal. The energy expression of the Crystal field is given as:

$$V_{cf}(r) = \int \frac{e\rho(R)}{|r-R|} dR \qquad (2.3.4)$$

where $\rho(R)$ is the charge density of the surrounding electrons and nuclei, e is electronic charge.

In transition metals, the crystal field effect is much stronger then spin-orbit interaction resulting in orbital quenching and this is the reason for the disagreement between Hund's third rule and experimental result for the magnetic moment of transition metals. Table 2.3.1 compares the measured effective moments with those predicted by Hund's rules. The observations agree better with a moment calculated from *S* rather than *J*. This is because the moments precess in the crystal field leading to L=0.[2]

ion	Shell	S	L	J	P_1	P_{exp}	P2
Ti^{3+},V^{4+}	$3d^1$	1/2	2	3/2	1.55	1.7	1.73
V^{3+}	$3d^2$	1	3	2	1.63	1.61	1.83
Cr^{3+},V^{2+}	$3d^3$	3/2	3	3/2	0.77	3.85	3.87
Mn^{3+},Cr^{2+}	$3d^4$	2	2	0	0	4.82	4.90
Fe^{3+},Mn^{2+}	$3d^5$	5/2	0	5/2	5.92	5.82	5.92
Fe^{2+}	$3d^6$	2	2	4	6.70	5.36	4.90
Co^{2+}	$3d^7$	3/2	3	9/2	6.63	4.90	3.87
Ni^{2+}	$3d^8$	1	3	4	5.59	3.12	2.83
Cu^{2+}	$3d^9$	1/2	2	5/2	3.55	1.83	1.73
Zu^{2+}	$3d^{10}$	0	0	0	0	0	0

Table 2.3.1: Magnetic ground states for 3d ions, P_1 is the value of $p = \mu_{eff}/\mu_B$ predicted by Hund's rules, P_2 is calculated p value assuming orbital quenching and P_{exp} is the experimental values.

2.4 Magnetic domain

Because the dipolar interaction in equation (2.3.1) is long range, within a ferromagnetic body it is often energetically favourable to form domains within the system. Figure 2.4.1a shows a single domain with large dipolar energy. The dipolar energy is reduced in figure 2.4.1b and figure 2.4.1c due to the reduced spatial extension of the field by having domains closure. The dipolar energy is minimised in figure 2.4.1d as the magnetic flux circuit is completed within the ferromagnetic body. However this introduces a number of domains. It costs energy to form domain since domain walls are needed at the domain interfaces. Depending on the magnitude of the exchange interaction and the magnetic anisotropy, in some cases the energy cost to produce domain wall may be higher then the saving of domain formation and in that case domain formation is not favourable [4].

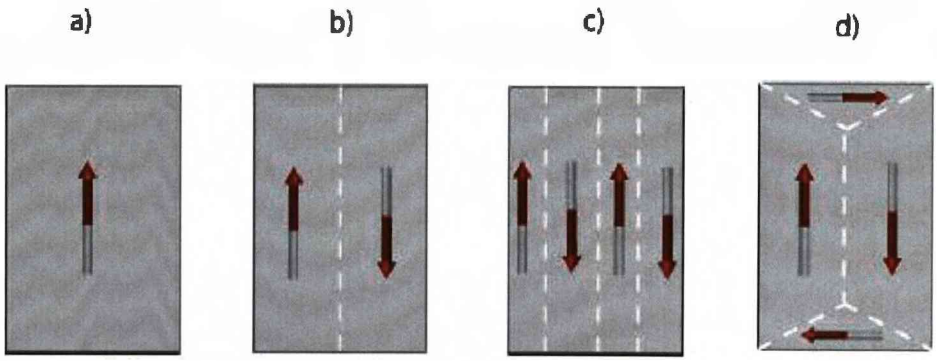

Figure 2.4.1: Different domain configurations: a) single domain, b, c) multi-domain structures. d) Closure domain where the dipolar energy is minimized.

2.5 Magnetic anisotropy

Magnetocrystalline anisotropy

In bulk metals, it is often found that it is easier to magnetize the crystal in one crystallographic direction over the others. The easier direction is known as the "easy

axis", and the term "hard axis" is used for other directions. This anisotropy energy arises from the spin-orbit interaction and the fact that there is only partial quenching of the angular momentum. For cubic crystals due to the high symmetry the anisotropy energy can be expressed in a simple manner as a polynomial series:

$$E = K_1(m_x^2 m_y^2 + m_y^2 m_z^2 + m_z^2 m_x^2) + K_2 m_x^2 m_y^2 m_z^2 + \ldots\ldots \quad (2.5.1)$$

where $m = (m_x, m_y, m_z) = \boldsymbol{M}/|M|$ and $\boldsymbol{M}$ is the magnetisation vector, K_1 and K_2 are anisotropy constants for the given material. When $K_1 \geq 0$ the first term of equation (2.3.1) becomes a minimum for $\langle 100 \rangle$ directions, whilst for $K_1 \leq 0$ it is a minimum for $\langle 111 \rangle$ directions. The anisotropy energy is strongest in lattices with low symmetry and weaker at higher symmetry sites. For example, the cubic systems Fe and Ni have $K_1 = 4.8 \times 10^4$ Jm^{-3} and -5.7×10^3 Jm^{-3}, respectively, whereas for hexagonal Co K_1 is 5×10^5 Jm^{-3}. The low-symmetry permanent magnet $Nd_2Fe_{14}B$ has an even higher value, $K_1 = 5 \times 106$ Jm^{-3}.

Shape anisotropy

The shape anisotropy is mediated by the dipolar interaction and is long range interaction and its contribution is dependent on the shape of the sample. In thin films, the magnetic shape anisotropy energy per unit volume is given by [[4]:

$$E = \frac{1}{2}\mu_0 M_s^2 \cos^2\theta \quad (2.5.2)$$

where θ is the angle between the surface normal and M_s is the saturation magnetisation. The shape anisotropy energy is at a minimum when the angle θ is 90° i.e. moments lying in the plane of the layer.

2.6 Magnetic coupling in multilayers

Magnetic coupling between FM blocks is observed across nonmagnetic spacer layers up to 100Å thick. Since the magnetic blocks are not in contact with each other, this is clearly another type of indirect exchange interaction. If the intermediate layer is metallic the exchange relies on the polarization of the conduction electrons in the spacer layer, and the coupling mechanism resembles the RKKY interaction. If the spacer layer is an insulator quantum mechanical tunnelling of the wavefunction is required. In this section we will focus on FM blocks with an insulating spacer which relates to Fe/MgO superlattices presented in chapter 4. The interaction through the insulating block determines the magnetic coupling between the FM materials and gives rise to FM or AF coupling. In this section we will examine two useful models to describe the coupling.

Néel coupling

The presence of correlated interfacial roughness leads to a significant dipolar energy. "Néel coupling" or, as it is better known, "orange peel" coupling, is a model developed by Néel [6] to describe the magnetic interaction between two ferromagnetic layers of infinite thickness, separated by a nonmagnetic spacer with a wave like correlated interface (figure 2.6.1). Provided h is the wave amplitude with wavelength λ, the interlayer coupling energy J is given by

$$J = \frac{\pi^2 h^2 \mu_0 M_F M_p}{\sqrt{2\lambda}\exp(-2\pi\sqrt{2t/\lambda})} \cdot \qquad (2.6.1)$$

Néel coupling is caused by the correlated roughness at the interface and it gives rise to ferromagnetic coupling between the two ferromagnetic blocks. For systems like the Fe/MgO multilayers, which have insulating spacer layers, FM coupling between the FM blocks for very thick spacer layers is believed to be mainly due to Néel coupling.

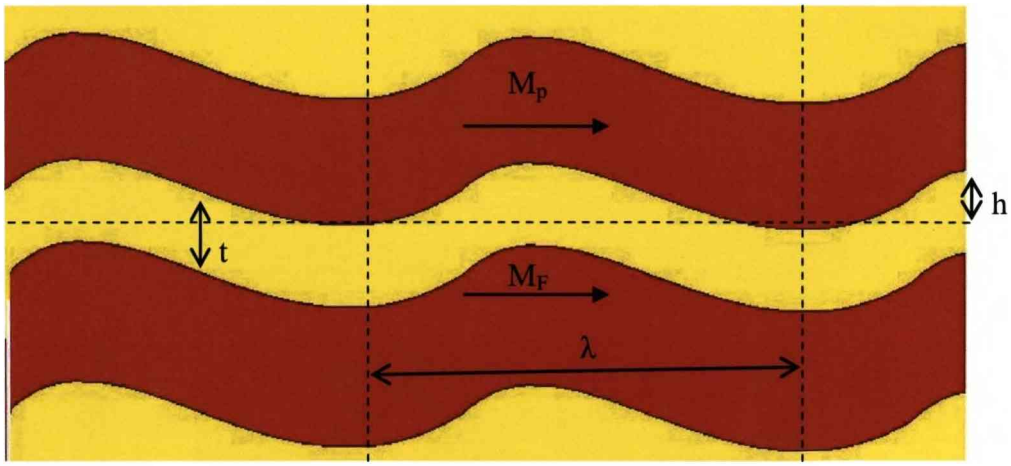

Figure 2.6.1: Magnetic film with Néel coupling.

Interlayer exchange coupling

Interlayer exchange coupling describes the magnetic coupling between the magnetic blocks in multilayers where the magnetic blocks are separated by a nonmagnetic spacer layer. The basic principles underlying the interlayer coupling can be understood from quantum interference effects using Bruno's free electrons model, see Fig. 2.6.2 [7,8]. A unified treatment of metallic and insulating spacer layers can be obtained using the concept of the complex Fermi surface [7]. Real wave vectors give propagating waves, whereas imaginary wave vectors correspond to evanescent waves.

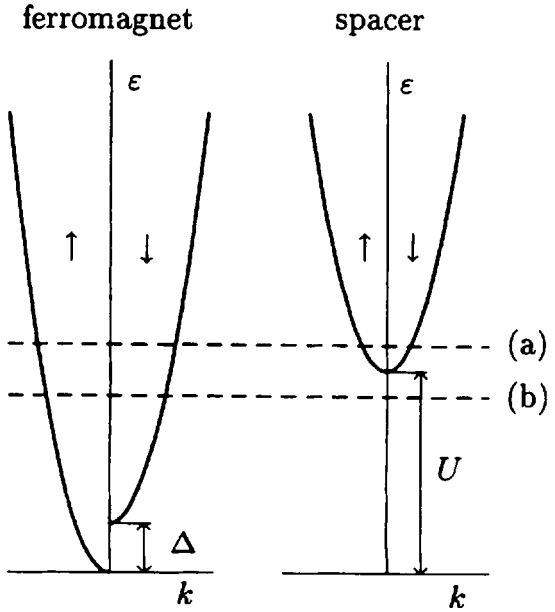

Figure 2.6.2: Sketch of the free electron model; the dashed line indicates the position of the Fermi level, (a) for a metallic spacer layer, (b) for an insulating spacer layer. Zero of potential is taken as the bottom of the majority band of the FM layers; the potential of the minority band is given by the exchange splitting Δ; the potential of the spacer is U.

Inside a ferromagnet the majority electrons are polarized parallel, and the minority electrons anti-parallel, to the magnetisation direction. As the polarized electron wave travels through the spacer layer it encounters two interfaces and the electron waves can either be transmitted or reflected at these interfaces. Multiple reflections within the spacing layer can result in the quantum interference effect. It is the dependence of the propagation and reflection of these polarised electrons on the relative orientation of the magnetisations in the FM blocks that gives rise to interlayer exchange coupling in magnetic multilayers.

Consider a spacer layer of thickness D, sandwiched between two semi-infinite FM layers, whose magnetisations are at an angle θ with respect to each other. The interlayer exchange coupling per unit area is given by [7]

$$E(\theta) = J_0 + J_1 \cos(\theta) + J_2 \cos^2(\theta) + \ldots \qquad (2.6.2)$$

where J_0 is not magnetic, J_1 corresponds to Heisenberg coupling, J_2 to biquadratic coupling etc. We are interested in the Heisenberg term

$$J_1 = -\frac{1}{4\pi^3}\,\mathrm{Im}\int d^2k_{xy}\int_{-\infty}^{+\infty} f(\varepsilon)d\varepsilon$$

$$\times\frac{2\Delta r^2 e^{iq_z D}}{1-2\bar{r}^{-2}e^{iq_z D}+\left(\bar{r}^{-2}-\Delta r^2\right)^2 e^{2iq_z D}} \tag{2.6.3}$$

where $f(\varepsilon)$ is the Fermi-Dirac function, k_{xy} is the in-plane component of the wave vector, q_z is the difference between reflected and incident out-of-plane components of the wave vectors, and the spin-average of the reflected amplitudes is

$$\bar{r} = \frac{r^{\uparrow}+r^{\downarrow}}{2} \tag{2.6.4}$$

and the spin-asymmetry of the reflected amplitudes is

$$\Delta r = \frac{r^{\uparrow}-r^{\downarrow}}{2} \tag{2.6.5}$$

In the limit of large spacer thickness, one obtains for a metal spacer

$$J_1 = \frac{1}{4\pi^2}\frac{\hbar^2\kappa_F^{\ 2}}{mD^2}\,\mathrm{Im}(\Delta r^2 e^{2i\kappa_F D})$$

$$\times\frac{2\pi k_B TDm/\hbar^2\kappa_F}{\sinh(2\pi k_B TDm/\hbar^2\kappa_F)}. \tag{2.6.6}$$

where the Fermi wave vector of the spacer layer is given by

$$k_F = \left[\frac{2m(\varepsilon_F - U)}{\hbar^2}\right]^{\frac{1}{2}} \tag{2.6.7}$$

In the case of insulating spacer layers one obtains in the limit of large spacer thickness

$$J_1 = -\frac{1}{4\pi^2}\frac{\hbar^2\kappa_F^{*\,2}}{mD^2}\,\mathrm{Im}(\Delta r^2 e^{-2\kappa_F^* D})$$

$$\times\frac{2\pi k_B TDm/\hbar^2\kappa_F^*}{\sin(2\pi k_B TDm/\hbar^2\kappa_F^*)}. \tag{2.6.8}$$

where the Fermi wave vector of the spacer layer is given by

$$k_F^* = \left[k_{ll}^2 + \frac{2m(U - \varepsilon_F)}{\hbar^2} \right]^{\frac{1}{2}} \tag{2.6.9}$$

This reduces to Slonczewski's result for the interlayer coupling across a tunnelling barrier [9]. The sign of the coupling is determined by the argument of Δr^2. If

$$k_F^{*2} < k_F^{\uparrow} k_F^{\downarrow} \tag{2.6.10}$$

then the coupling is antiferromagnetic, whereas if

$$k_F^{*2} > k_F^{\uparrow} k_F^{\downarrow} \tag{2.6.11}$$

then the coupling is ferromagnetic. Here $k_F^{\uparrow}$ and $k_F^{\downarrow}$ are the Fermi wave vector of the majority and minority spin electrons in the FM, respectively.

The only difference between equation (2.6.6) for the metal spacer and (2.6.8) for the insulator is the replacement of k_F by ik_F^*. This changes the oscillatory thickness dependence of the metallic spacer to an exponential decrease with spacer thickness for the insulator. This transformation also changes the last factor in equations (2.6.6) and (2.6.8) from a hyperbolic sine in the denominator to a sine. Thus, in contrast to the metallic case where the exchange decreases with temperature, the exchange coupling actually increases with temperature for an insulating spacer.

The interlayer exchange coupling calculated using equation (2.6.3) is shown in Fig. 2.6.3 for a metal and Fig. 2.6.4 for an insulating spacer [8]. The behaviour of the metal corresponds to that of the RKKY interaction for the spacer layer, and the coupling changes from AF to FM depending on the spacer thickness. In contrast, the coupling is always AF for these model parameters for the insulator, except for very small spacer thicknesses, where states well below the Fermi level may contribute. For very large spacer thicknesses the interlayer exchange is small and the Néel coupling may take over.

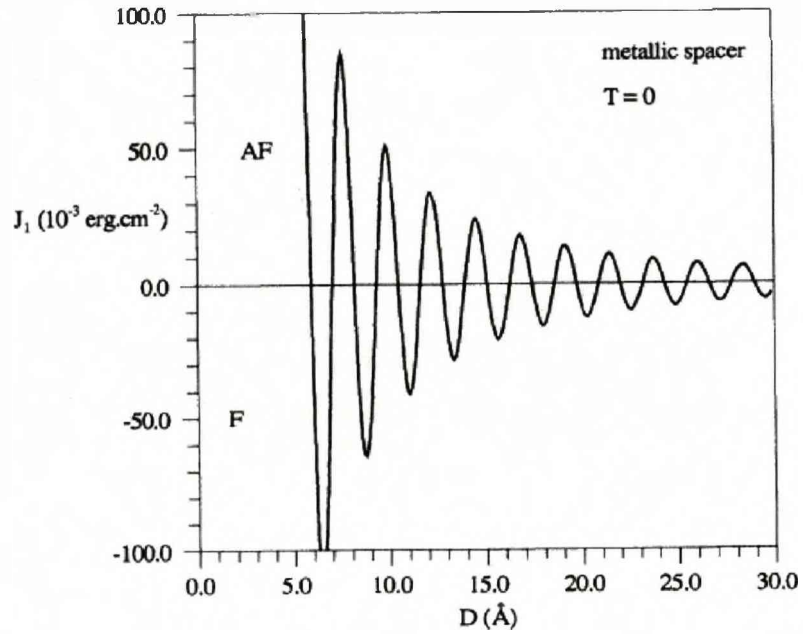

Figure 2.6.3: Interlayer exchange coupling for metallic spacer, at $T = 0$, for the free-electron model with $\varepsilon_F = 7.0$ eV, $\Delta = 1.5$ eV and $U = 0$ [8].

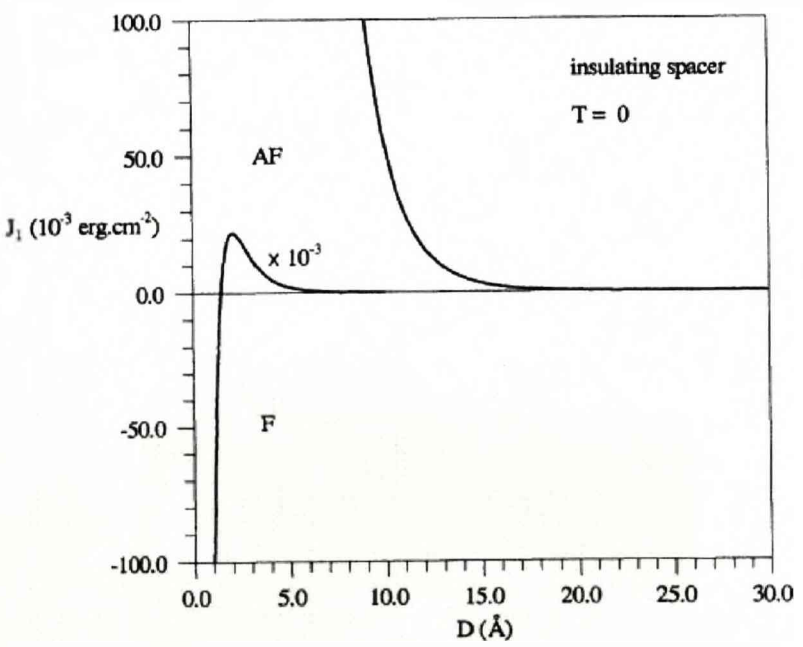

Figure 2.6.4: Interlayer exchange coupling for insulating spacer, at $T = 0$, for the free-electron model with $\varepsilon_F = 7.0$ eV, $\Delta = 1.5$ eV and $U - \varepsilon_F = 0.1$ eV [8].

Magnetic spacer layers

When the spacer layer is magnetic the direct exchange interaction at the interface may be dominant. For the case of ferromagnetic (FM) layers next to anti-ferromagnetic (AF) layers, this gives rise to exchange bias phenomenon in multilayers, see Fig. 2.6.5. Such a FM-AF system is cooled in a magnetic field from above the AF Néel temperature. Provided the Curie temperature of the FM is greater than the AF Néel temperature, the measured magnetic hysteresis loop observed at a temperature less than the AF Néel temperature will appear to be shifted as if another magnetic field was present in addition to the applied magnetic field. It appears to be energetically favourable for the FM to be magnetized in one direction rather than the other.

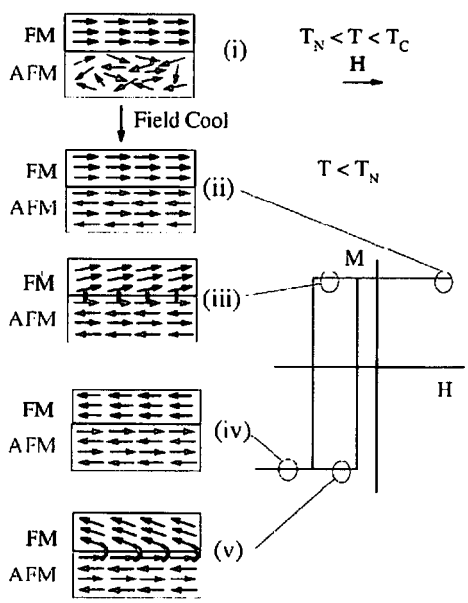

Figure 2.6.5: Schematic diagram of the spin configuration of an exchange bias system.

2.6 Magnetic coupling in nanoparticles

In this thesis I shall consider FM nanoparticles. In many FM samples the lowest energy state is often the domain closure state, so that the dipolar energy is minimised and the overall magnetic moment is zero. However if the particle size is reduced, surface energies (domain wall formation) become progressively more costly in comparison with the saving of volume energies (dipolar energy). This is because surface energies scale as the sample size squared whereas volume energies scale as the sample size cubed. Therefore below a critical dimension it is energetically favourable to have no domain wall so that the sample consists of only one magnetic domain and behave like a small permanent magnet. In our studies of nanoparticles the particles size is always in the nanometre range and it is more favourable for the nanoparticles to have no domain structure.

Shape anisotropy can also have a key role for nanoparticles. For example, if the particles are elongated along one direction the moment is likely point along that direction, whereas spherical particles clearly have no anisotropy at all.

The interactions between arrays of nanoparticles that are isolated from each other are necessarily dipolar in nature. The self-assembled Co and Fe_2O_3 arrays in chapter 7 fall into this category. However, if the particles are separated by metallic media, indirect interactions are possible. Skomsky [10] and Altbir *et al.* [11] have compared interparticle RKKY and dipolar interactions using an integral calculation in the limit of large distances, and the summation over many pairs, respectively. Both approaches yield the result that dipolar interactions dominate for particle sizes greater than 1nm. However, if the matrix contains magnetic impurities, like the Co/Ag system in chapter 5, the RKKY-like interactions can potentially be enhanced [12].

If the FM nanoparticles are surrounded by an AF shell, like the oxidised Co nanoparticles in chapter 6, then exchange bias similar to that described above for multilayers, may also occur for magnetic nanoparticles.

Bibliography

[1] M.A. Ruderman and C. Kittel. *Phys. Rev.*, **96**:99-102, 1954.

[2] T.Kasua Progr. Theoret.Phys. Rev., 96(99),1954

[3] K. Yosida. Phys. Rev. 106(893),1957

[4] "Magnetism in Condensed Matter" by S.J. Blundell. OUP (2001).

[5] A.E. Berkowitz and K. Takano J. Magn. Magn. Mater. **200**, 552 (1999).

[6] L.Néel, Comptes. Rendus 255, 1676 (1962)

[7] P. Bruno Phys Rev B 49 13 231 (1994)

[8] P. Bruno Phys Rev B 52 411 (1994)

[9] J.C. Slonczewski Phys Rev B 39 6995 (1989)

[10] R. Skomsky Europhys Lett 48 455 (1999)

[11] D. Altbir, J. d'Albuquerqe e Castro and P. Vargas Phys Rev B 54 R6823 (1996)

[12] A. Lopez, F.J. Lázaro, M. Artegas and A. Larrea Phys Rev B 66 174413 (2002)

[13] R. Skomski, JMD. Coey, Permanent Magnetism, IoPP Studies in Condensed Matter Phys, 1999

[14] H. Ibach, H. Luth, Solid-State Physics, Springer

Chapter 3

Experimental Techniques

3.1 General scattering theory

3.1.1 Scattering Cross-Sections

The most import quantity in scattering theory is the scattering cross section, which governs all the scattering processes and it is defined as:

$$\sigma_{tot} = \frac{\text{total number of scattered particles per second}}{\psi}, \quad (3.1.1.1)$$

where ψ is the total incident flux. The number of particles scattered into some solid angle $d\Omega$ is given by

$$\frac{\partial\sigma}{\partial\Omega} = \frac{\text{number of particles scattered s}^{-1} \text{ into d}\Omega}{\psi \cdot d\Omega}. \quad (3.1.1.2)$$

This is known as the differential cross section and has units of area. The differential cross section is the quantity that is measured during any scattering experiment, and it will be derived for different scattering techniques throughout this chapter. Following the definition of $\delta\sigma/\delta\Omega$ above, this cross section can be rewritten in the form:

$$\left(\frac{d\sigma}{d\Omega}\right)_{\lambda\to\lambda'} = \frac{1}{\psi}\frac{1}{d\Omega}\sum_{k'} W_{k,\lambda\to k',\lambda'}, \quad (3.1.1.3)$$

where $W_{k,\lambda\to k'\lambda'}$ is the number of transitions per second from the state k, λ to the state k', λ'. k and k' are the initial and final wavevector of the incident and scattered

particle respectively, whilst λ and λ' relate to the initial and final state of the scattering system.

In order to calculate $W_{k,\lambda\to k'\lambda'}$ we first assume that the scattering is a single-event process, i.e. there are no multiple scattering events within the sample, and particles in the incident beam do not interact with each other. In the case of x-ray and neutron scattering, due to the relatively small scattering cross sections, this assumption is usually satisfied. With this assumption in mind we can express the summation in equation (3.1.1.3) in terms of the interaction potential, V, between the incident particles and the scattering system. The application of first order time-independent perturbation theory yields Fermi's Golden rule:

$$\sum_{k'} W_{k,\lambda\to k',\lambda'} = \frac{2\pi}{\hbar}\rho_{k'}\left|\left\langle k'\lambda'\middle|V\middle|k\lambda\right\rangle\right|^2, \qquad (3.1.1.4)$$

where $\rho_{k'}$ is the number of momentum states per unit of solid angle, per unit energy range for state with wavevector k'.

To complete our discussion on scattering cross sections we substitute equation (3.1.1.4) back into equation (3.1.1.3) which yields an expression for the differential scattering cross section:

$$\left(\frac{d\sigma}{d\Omega}\right)_{\lambda\to\lambda'} = \frac{1}{\psi}\frac{1}{d\Omega}\frac{2\pi}{\hbar}\rho_{k'}\left|\left\langle k'\lambda'\middle|V\middle|k\lambda\right\rangle\right|^2. \qquad (3.1.1.5)$$

Equation (3.1.1.5) is the fundamental equation used to derive the cross section for individual scattering experiments. Only the expression for the interaction potential V is required in each case [1].

3.1.2 X-ray scattering

The interaction between the x-ray electric field and the charge density within an atom can result in scattering, and the cross section for this scattering can be expressed using equation 3.1.1.5. Charge scattering can be understood in term of the electromagnetic wavefunction,

$$E(r, t) = \hat{E}_i E_0 e^{i(k.r-\omega t)} \qquad (3.1.2.1)$$

where $\hat{E}_i$ is the incident polarization of the field, k is the wave vector and ω determines the oscillation frequency of the field. On collision with matter the electromagnetic wave is absorbed and reemitted as a electromagnetic photon, with energy equal to the incident photon energy, which travels outward in a spherical wave form with wave vector k' and polarisation state $\hat{E}_f$. As there is no change in the x-ray energy this process is elastic.

The differential cross section for x-ray scattering from an atom is given as:

$$\frac{d\sigma}{d\Omega} = (r_o)^2 \left[\hat{E}_i \cdot \hat{E}_f\right]^2 \sum_{\mu \to \mu'} \left| \left\langle \mu' \left| \sum_j \rho(r) e^{iQ \cdot R_j} \right| \mu \right\rangle \right|^2 . \qquad (3.1.2.2)$$

The pre-factor, $r_o=(e^2/4\pi\varepsilon_0 m_e c^2)=2.82\text{x}10^{-5}$Å is the classical electron radius, j is the index for the summation over all the electrons in the atom, $\rho(r)$ is the charge density and $Q=k_i-k_f$ is the wave vector transfer.

The expression can be simplified if we assume monatomic crystals and, therefore, we can factorise the crystal into systematic arrays of unit cells each comprising the same arrangement of atoms with the same electron density. Then the electron position can be written as $R_j=R_l+r_d+r_e+u_{ld}$ where R_l is the Bravais lattice vector, r_d is the time-averaged positions of the atoms within a unit cell, r_e is position of the electron sites within the atom and u_{ld} corresponds to the instantaneous fluctuations of the atomic positions about their equilibrium values. Together with equation (3.1.2.2) the differential cross section becomes,

$$\frac{d\sigma}{d\Omega} = (r_o)^2 \left[\hat{E}_i \cdot \hat{E}_f\right]^2 f_D N^2 v_c^* \left| \sum_{d=1}^{unit\ cell\ atoms} f(Q) e^{iQ \cdot r_d} \right|^2 \partial(Q - \tau) \qquad (3.1.2.3)$$

where the form factor for a given atom, $f(Q)$, is the Fourier Transform of the electron density

$$f(Q) = \int \rho(r) e^{iQ \cdot r_e} . \qquad (3.1.2.4)$$

The term f_D is the Debye-Waller factor, it takes into account the effect of vibrations of atoms in a crystal. It is of the form:

$$f_D(Q) = e^{-\frac{1}{3}\langle u^2 \rangle Q^2} , \qquad (3.1.2.4)$$

and has the effect of reducing the scattering intensity as Q increases. $\langle u \rangle$ is the mean-square displacement which is temperature dependent. As the temperature increases the mean-square displacement increases and this causes the scattering intensity to decrease. The summation in equation (3.1.2.3) is only over the atoms within the unit cell, since the remaining atoms within the crystal are simply a repeat of this unit cell and only scale the overall intensity by N^2, where N is the number of unit cells in the sample. v_c^* is the volume of the unit cell in reciprocal space. The delta function ensures that the scattering condition is satisfied, i.e. the wave-vector transfer is a point on the reciprocal lattice. Thus, the delta function indicates that scattering only occurs at Bragg positions and is zero elsewhere. However this is only true for an ideal system, in reality there is line broadening of the peaks due to the presence of crystalline imperfections, the finite size of crystal, and the resolution of the diffractometer.

So far we have considered the classical case where the electrons are evenly distributed around a positive nucleus. However, atomic electrons are governed by quantum mechanics, and consist of discrete energy levels. The most tightly bound electrons have energies comparable to those of an x-ray photon, so if the energy of the photon is much less then the binding energy of the electron, then the response of the electron due to photon alternating field will be greatly reduced, consequently the scattering cross section will also be reduced. In addition the responses of the bound electrons will have a phase lag with respect to the driving field. Taking these two quantum effects into account in our scattering cross section, the form factor f(Q) becomes:

$$f(Q,\hbar w) = f^{0}(Q) + f^{'}(\hbar w) + if^{''}(\hbar w) + f_{spin}(Q). \quad (3.1.2.5)$$

f^0(Q) and f_{spin}(Q) are the charge scattering form factor and the non-resonant magnetic scattering form factor respectively, and they are independent of energy. One must note that in general the charge scattering term is several orders of magnitude larger than the magnetic interaction term. Therefore in general the magnetic scattering is usually regarded as a negligible contribution. Finally f' and f'' are known as the anomalous dispersion corrections, which are energy dependent and they are due to the quantum mechanical effects we have mentioned above[2].

X-ray scattering from a multilayer

The intensity of the elastically scattered x-rays from a crystal is given by equation (3.1.2.3). Consider the scattering from a multilayer system comprising N bilayers with Q in the growth direction. Each bilayer has n_a atoms of type a and n_b atoms of type b. This equation becomes

$$I(Q) \propto \left| \left(\sum_{S=1}^{N} e^{iQLS} \right) \left(\sum_{l=0}^{n_a+n_b-1} f_l(Q) e^{iQR_l} \right) \right|^2 \quad (3.1.2.6)$$

where L is the mean bilayer thickness and R_l is the component of the position vector in the growth direction for the l^{th} atom. The first term generates a series of peaks at positions given by $Q=(2\pi m/L)$, where m is an integer [3]. The widths of the peaks are determined by the numbers of bilayers that are being summed over. A large value of N will give rise to a narrow peak, and as $N \rightarrow \infty$ the first term becomes a delta function. The amplitude of the peaks are determined by the second term, which is a broadly oscillating "envelope" function. This term is known as the one-bilayer structure factor. All of the information on the nature of the atoms within the bilayer is contained within this term. To calculate this one-bilayer structure factor, one must determine the variation of $f_l(Q)$ and R_l as a function of l. In a real multilayer system, there may be surface roughness and inter-diffusion between the two materials at their interfaces. Even the best crystals will have some kind of inter-diffusion and, therefore,

a sharp interface is almost never observed. In this work we used a tanh function to model the changes at the interface. This function gives the required shape, with an almost liner variation at the middle of the interface and rounded at the edges. The expression for the concentration of atom a in the l_{th} layer is

$$c_a(l) = \frac{1}{2}\left[1 + \tanh\{(l+0.5)/\lambda_1\} - \tanh\{(l+0.5-n_a)/\lambda_3\} + \tanh\left[(l+0.5-n_a-n_b)/\lambda_1\right]\right], \quad (3.1.2.7)$$

where λ_1 and λ_3 are the widths between the *a/b* and *b/a* interfaces, respectively. The scattering amplitude of the l^{th} layer is then given by:

$$f_1(Q) = c_a(l) f_a(Q) + \left[1 - c_a(l)\right] f_b(Q). \quad (3.1.2.8)$$

The expression for the d spacing is similar to equation (3.1.2.7), apart from the arguments of the function are adjusted to ensure that they are centred at the atomic positions rather than atomic sites.

$$g_a(l) = \frac{1}{2}\left[1 + \tanh\{l/\lambda_2\} - \tanh\{(l-n_a)/\lambda_4\} + \tanh\left[(l-n_a-n_b)/\lambda_2\right]\right] \quad (3.1.2.9)$$

and d spacing is given by:

$$d_m = g_a(l) d_a + \left[1 - g_a(l)\right] d_b. \quad (3.1.2.10)$$

Then the position of the l^{th} atom is simply:

$$R_l = \sum_{m=0}^{l} d_m \quad (3.1.2.11)$$

The parameters λ_2 and λ_4 represent the inter-diffusion at the interface *a/b* and *b/a*, respectively. However λ_2 and λ_4 also give information on the strain at the interfaces. Therefore, even for a perfectly sharp interface the value of λ_2 and λ_4 are non zero because there are strains for the atoms near the boundary since the two materials must be lattice matched in the plane at the interface.

Experimental considerations and data corrections

Even when the scattering response function from the system is known, there are other factors that need to be taken into account to reproduce the observed scattering intensity due to the specific experimental configuration. Here we discuss some of those factors.

Resolution effects

In an ideal experiment the width of an observed diffraction peak would solely depend on the coherence between the scattering centres in the crystal lattice. However, in reality the instrumental resolution plays an important part in the width of an observable peak. The peak observed is, in fact, a convolution of the intensity from the crystal and the instrumental resolution function.

The computation of resolution functions for triple-axis neutron spectrometers has been performed by Cooper and Nathans [4]. The form of the resolution function is complex, and varies over Q_h, Q_k, Q_l, and energy, and the essential results in Q-space apply equally to x-ray diffractometers. However, if a scan is performed in only one wavevector component direction, a Gaussian form of instrumental resolution can usually be assumed. Coherence lengths are obtained from the full-width-half-maximum (FWHM) of a scans performed in a particular reciprocal space direction. The coherence length is given by,

$$\xi = \frac{2\pi}{\Delta Q} \qquad (3.1.2.12)$$

where ΔQ is the FWHM of a scan along a reciprocal space direction. The instrumental resolution becomes important when one tries to correlate the peak width with any model. The observable line shapes are usually altered by instrumental resolution effects. The FWHM of the observed scattering, Γ^{obs}, can be linked to the instrumental FWHM, Γ^{inst}, by

$$\Gamma^{obs} = \sqrt{(\Gamma^{s})^2 + (\Gamma^{inst})^2}\,, \qquad (3.1.2.13)$$

where Γ^{s} is the true FWHM of the sample that would be measured if there were no instrumental broadening of the line shapes.

The instrumental resolution function can be measured directly using a high quality crystal with very narrow true FWHM. The MgO substrates used in this thesis have very narrow mosaic spreads and, therefore, give very narrow Bragg diffraction peaks that are ideal for the determination of the instrumental resolution.

Lorentz Corrections

The observed intensity of a Bragg peak does not solely depend on the intensity of the crystal's structure factor. It also depends on how the scan was performed. The Lorentz factor relates the measured area of a peak to the intrinsic peak intensity. The Laue condition states that a Bragg reflection will only occur if the wavevector transfer $Q = k_i - k_f$ is equal to a reciprocal lattice vector τ. For elastic experiments it requires that $|k_i| = |k_f|$ so the locus of the possible vectors Q forms a sphere of radius $|k_i|$ in reciprocal space. This sphere is known as the Ewald sphere. The Lorentz factor is a geometrical term which corrects for the different rates at which the reciprocal lattice points scan through the Ewald sphere. As the wave-vector transfer moves through reciprocal space, the Ewald sphere passes over the Bragg point τ. The number of scattered neutrons or x-rays is proportional to the time that τ is coincident with the Ewald sphere. If ω is the angular velocity of the crystal and v_n is the component of the velocity of the reciprocal lattice point along the radius of the moving sphere, the Lorentz correction is defined as the ratio of the two velocities $L = \omega/v_n$. The Lorentz

correction can be simplified if the scans are specular. In this case the integrated intensity, I is given by

$$I = \frac{I'}{2\sqrt{B_{11}}\sin\theta}, \qquad (3.1.2.14)$$

where I' is the measured integrated intensity, ϑ is the Bragg angle and B_{11} is an instrument dependent constant.

Absorption Corrections

X-rays are absorbed as well as scattered in their passage through matter. If a narrow beam of monochromatic radiation passes through a thickness I in the crystal, the emergent intensity I is related to incident intensity I_0 by:

$$I = I_0 \exp(-\mu l) \qquad (3.1.2.15)$$

where μ is the linear absorption coefficient. For a crystal with a flat surface, geometric considerations of the beam path through a crystal for a given orientation lead to the relation

$$I = \frac{I_0 \sin\varepsilon}{\sin\varepsilon + \sin\phi} \qquad (3.1.2.16)$$

where $\varepsilon = \theta - \alpha$, $\phi = \theta + \alpha$, θ is the Bragg angle and α is the angle between the scattering planes and the surface of the crystal, Figure(3.1.2.1). For scans along the surface normal direction, α is zero and the measured intensity is simply half the incident intensity.

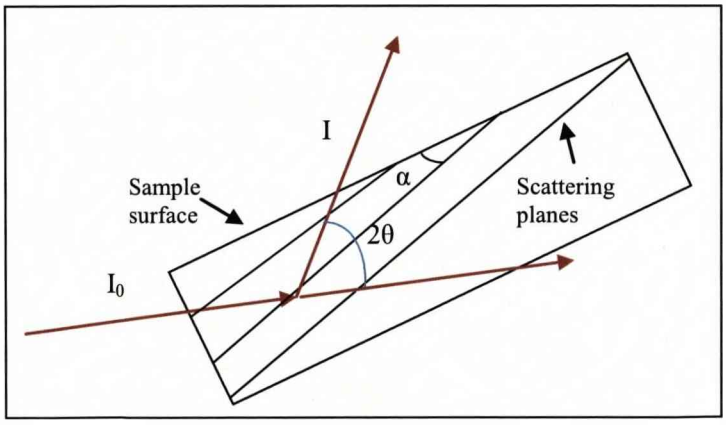

Figure(3.1.1): Diagram showing the scattering geometry.

Instrumentation

Fixed tube diffractometer

X-ray measurements were performed using a Philips X'Pert Pro x-ray diffractometer, in the Department of Physics at the University of Liverpool. This diffractometer produces x-ray by accelerating electrons to a water-cooled copper anode. The greatest intensity occurs for the characteristic K_α line at a wavelength of 1.54Å. The x-ray beam passes through a divergence slit followed by a multilayer x-ray mirror. The mirror focuses a large solid angle of x-rays into a parallel beam. The parallel beam then passes through a Ge(2 2 0) four-bounce monochromator before it reaches the sample. The scattered beam from the sample can be measured either directly in two-axis mode or after reflection off an analyser crystal, in triple-axis mode. Triple-axis mode gives a much better resolution and a substantial amount of background reduction. However it reduces the effective incident x-ray intensity by six fold.

Synchrotron Radiation

Synchrotron radiation is typically about 10^{12} times more intense than fixed tube sources. X-rays are emitted when high energy electrons are deflected by strong magnetic fields. A synchrotron consists of bunches of electrons circulating in a

storage ring at a speed very close to the speed of light, the electrons are accelerated by bending magnets, and as a result x-rays are emitted tangential to the electron flight path. The intensity of x-rays emitted by the electrons can be further increased using an insertion device. An insertion device is a line of magnets that force the electrons to oscillate, and for each oscillation x-rays are emitted, and if these x-rays add coherently, an extremely intense beam can be obtained.

Experiments were performed on the materials and magnetism beam line I16 at Diamond, Didcot. I16 uses an insertion device to produce intense x-rays. The energy range of I16 is between 3.5kev to 25kev. The calculated monochromatic flux at sample is about 10^{14} photon per second. Finally, a scintillator was used to measure the scattered x-rays.

3.1.3 Thermal neutron scattering

Neutrons are excellent probes of crystalline matter because they are uncharged particles and possess magnetic moments. Uncharged particles do not experience any Coulomb force and, therefore, neutrons can penetrate a substantial amount of material, and are only scattered by the nuclei and the magnetic moments of the material. Most importantly the de Broglie wavelength of thermal neutron is comparable to the inter-atomic distances in solids, so that interference effects can yield information on the structure of the scattering system.

Elastic neutron nuclear scattering

The differential cross section for coherent elastic neutron nuclear scattering is very similar to x-ray scattering. One can applies Fermi's golden rule to determine the transition (scattering) rate if one assumes the scattering centre (the nucleus) is a point-like nuclear potential

$$V_N = \frac{2\pi\hbar^2}{m}\sum_l b_l \partial(\bar{r} - \bar{R}_l) \qquad (3.1.3.1)$$

where b_l is the nuclear scattering length and m is the neutron mass. One major difference between neutrons and x-rays is that x-rays are scattered by the distribution of electrons rather than the nucleus. Hence the scattering depends on the atomic number, and is dominated by elements with high atomic numbers. In contrast, neutron scattering is due to the strong nuclear force and this varies erratically with atomic number. As a consequence, neutrons see light atoms such as hydrogen or oxygen much better than x-rays. The interaction with the nucleus also depends on the spin state of the nucleus. The nuclear spins are usually not ordered and can be treated as ideal paramagnets.

Taking the nuclear potential above together with equation (3.1.1.3), the resulting equation for the differential cross section can be broken down into two parts: coherent scattering and incoherent scattering terms. The incoherent component depends on the correlation between the positions of the same nucleus at different times and does not give rise to interference. In fact, it arises from the random distribution of isotopes and nuclear spin states. However, the coherent term depends on the correlation between the position of the same nucleus at different times, and the correlation between the positions of different nuclei at different times. It therefore gives interference effects and the elastic coherent scattering cross section per unit volume is given by

$$\frac{d\sigma}{d\Omega} = V^{-1}\left\langle \left| \sum_{l=1}^{N} b_l e^{iQ\cdot r_l} \right|^2 \right\rangle \qquad (3.1.3.2)$$

where V is the volume, N is the number of nuclei in the sample, b_l is the bound coherent scattering length of the l^{th} nucleus. The position of l^{th} nucleus is denoted by r_l and Q is the scattering wave vector.

Elastic magnetic neutron scattering

It is possible to incorporate a simplistic model of magnetic neutron scattering. The effect of magnetic moment can be made to modify the effective scattering length

such that moment directions associated with a lattice site are represented. The effective scattering length is given by:

$$b_{eff} = \bar{b} + \bar{b}_{mag}\hat{\mu} \times \hat{Q} \tag{3.1.3.3}$$

in which $\bar{b}_{mag}$ is the magnetic scattering length, $\hat{\mu}$ and $\hat{Q}$ are two unit vectors that take into account the fact that the magnetic scattering cross section depends on the direction of the magnetic moment at the scattering centre with respect to scattering wave vector.

3.1.4 Small Angle Neutron Scattering (SANS)

Small angle neutron scattering has been demonstrated over the years to be a useful tool for characterizing the structure of precipitates and voids in solids, and colloidal solids and liquids. In this section we will try to derive an expression for the SANS cross section, using the scattering theory developed over the last few sections.

We begin by making use of equation (3.1.3.2) and assume the sample contains N_p particles immersed in a homogeneous matrix. If we break down the sample volume into N_p cells each containing only one particle and label each nucleus with two subscripts *i* and j (Figure 3.1.4.1), then equation (3.1.3.2) become:

$$\frac{d\sigma}{d\Omega} = V^{-1}\left\langle \left| \sum_{i=1}^{N_p}\sum_{j=1}^{N_i} b_{ij} \exp(i\bar{Q}\cdot\bar{r}_{ij}) \right|^2 \right\rangle, \tag{3.1.4.1}$$

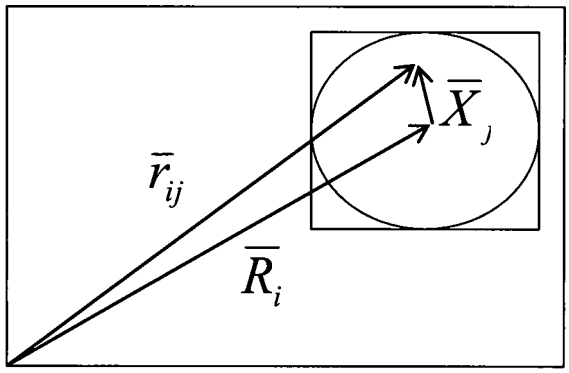

Figure 3.1.4.1: Geometrical notation used to construct equation (3.1.4.1) and equation (3.1.4.2).

where b_{ij} and $\bar{r}_{ij}$ are the scattering length and position of the j^{th} nucleus contained in the i^{th} cell. N_i is the number of nuclei within the i^{th} cell. If the centre of mass the i^{th} particle position is given by $\bar{R}_i$ and the position of nucleus $\bar{r}_{ij}$ can be rewritten in terms of $\bar{r}_{ij} = \bar{R}_i + \bar{X}_j$ m where $\bar{X}_j$ is the position of the nucleus relative to the centre of mass of the particle. So equation (3.1.4.1) becomes:

$$\frac{d\sigma}{d\Omega} = V^{-1}\left\langle \left| \sum_{i=1}^{N_p} \exp(i\bar{Q}\cdot\bar{R}_i)F_i(Q) \right|^2 \right\rangle \qquad (3.1.4.2)$$

where

$$F_i(Q) = \sum_{j=1}^{N_i} b_{ij}\exp(i\bar{Q}\cdot\bar{X}_j), \qquad (3.1.4.3)$$

is the form factor of the i^{th} particle. If we expand equation (3.1.4.2) then we get:

$$\frac{d\sigma}{d\Omega} = V^{-1}\left\langle \sum_{i=1}^{N_p}\sum_{i'=1}^{N_p} F_i(Q)F_{i'}^{*}(Q)\exp(i\bar{Q}\cdot(\bar{R}_i - \bar{R}_{i'}) \right\rangle, \qquad (3.1.4.4)$$

where the inner brackets represent the weighted average particle size distribution, and by decomposing this average the cross section reduces to

$$\frac{d\sigma}{d\Omega}(\bar{Q}) = n_p\left[<\left|F(\bar{Q})\right|^2> - \left|<F(\bar{Q})>\right|^2\right] + n_p\left|<F(\bar{Q})>\right|^2 S(\bar{Q}), \quad (3.1.4.5)$$

where $n_p=N_p/V$ is the average number density of particles in the sample and $S(\bar{Q})$ is the interparticle structure factor defined as

$$S(Q) = N_p^{-1}\left\langle \sum_{i=1}^{N_p}\sum_{i'=1}^{N_p} \exp[i\bar{Q}\cdot(\bar{R}_i - \bar{R}_{i'})]\right\rangle. \quad (3.1.4.6)$$

Going from equation 3.1.4.4 to 3.1.4.5 we assumed that the particle size and orientation are uncorrelated with the positions of the particles. The brackets <> represent an average weighted by the distribution of particle sizes and orientations. For a monodisperse system the cross-section will take a much simpler form

$$\frac{d\sigma}{d\Omega}(\bar{Q}) = n_p\left|<F(\bar{Q})>\right|^2 S(\bar{Q}) \quad (3.1.4.7)$$

where $<F(\bar{Q})>=\frac{1}{n_p}\sum F_i(q)$ and in the limit of very low particle density, the solution becomes ideal as $S(\bar{Q})=1$ [5-7].

Scattering form factor

In this section we will look at the small angle scattering form factor for different shaped particles. We will only cover those that were used in this thesis. A detailed listing of all commonly used form factors can be found in Ref. [7].

Sphere

The scattering form factor for a spherical particle with uniform scattering length density was calculated in 1911 by Lord Rayleigh [8] and it takes the form of:

$$F_{sphere}(Q) = \frac{3[\sin(QR) - QR\cos(QR)]}{(QR)^3}, \qquad (3.1.4.8)$$

where Q is wave vector transfer and R is the radius of the particle.

Core-shell

The structure of a core-shell particle is shown in figure 3.1.4.1. It consists of a spherical core particle surrounded by a spherical shell inside a matrix. Figure 3.1.4.1 also shows the change in scattering length density of the particle as a function of core radius for some arbitrarily chosen core-shell parameters. The form factor for a core-shell particle is then given by

$$F_{core\_shell}(Q) = \left|(p_c - p_s)F_{sphere}(QR_c) + (p_s - p_m)F_{shpere}(QR_s)\right|, \qquad (3.1.4.9)$$

where R_c and R_s are the radius of the core and shell. p_c, p_s and p_m are the scattering length density of the core, shell and matrix respectively [9].

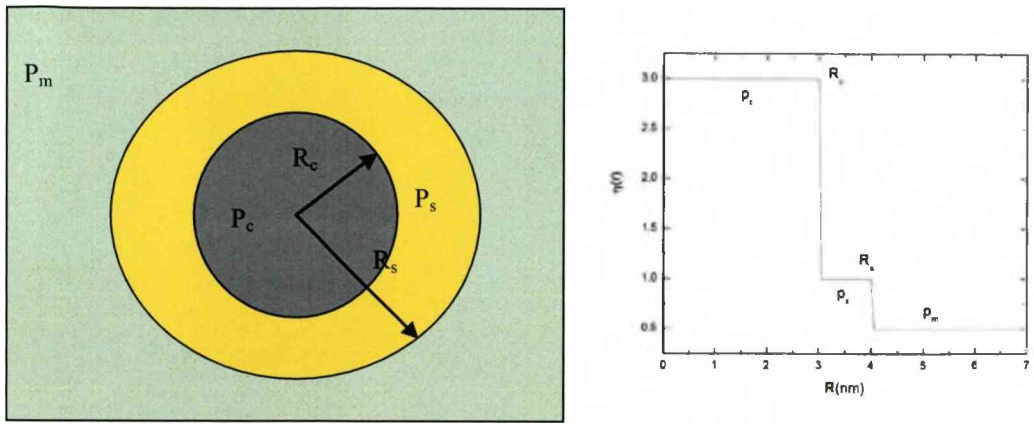

Figure 3.1.4.1: (Left) Core-shell particle structure and (right) the change in scattering length density as a function of radius.

Spherical particles with diffusion zone

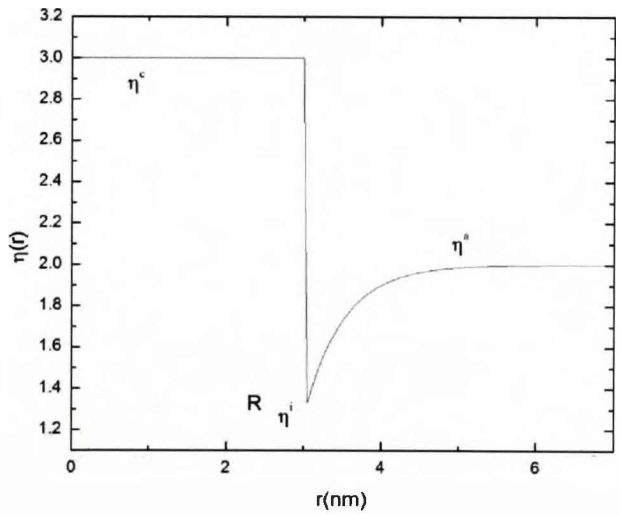

Figure 4.1.4.2: Scattering length density of a spherical particles with diffusion zone.

So far, for the last two scattering form factors, we have assumed that the interfaces are sharp. However, it is more realistic to model the interfaces as a diffusion zone [10]. The change in scattering length density for such particle can be described by

$$\eta(r) = \eta^c \Xi(R-r) + \left(\eta^a - (\eta^a - \eta^i)\exp[(R-r)/l]\right)\Xi(R-r), \quad (3.1.4.10)$$

with

$$\Xi(R-r) = \begin{cases} 0 & for \quad x < 0 \\ 1 & for \quad x \geq 0 \end{cases}$$

where R is the radius of the particle core. η^c, η^a and η^i are the scattering length density of the core, matrix and diffusion zone respectively, l is the width of the diffusion zone. Figure 3.1.4.2 shows the variation in the scattering length density of a typical particle with a diffusion zone. The form factor for a spherical diffusion zone particle is then given by

$$F(q,[R,l]) = F_{core}(q,[R]) + F_{shell}(q,[R,l]), \quad (3.1.4.10)$$

with

$$F_{core}(q,[R]) = (\eta^c - \eta^a)V_p f_{core}(q), \quad (3.1.4.11)$$

where $f_{core}(q)$ is the scattering form factor of a spherical particle. The more complex scattering amplitude of the diffusion zone can be written as

$$F_{shell}(q,[R,l]) = (\eta^i - \eta^a)V_p f_{shell}(q), \quad (3.1.4.12)$$

with

$$f_{shell}(q,[R,l]) = 3l\frac{(p_{\cos}\cos qR + p_{\sin}\sin qR)}{q(1+l^2q^2)^2R^3}, \quad (3.1.4.13)$$

where

$$p_{\cos} = l - l^3 q^2 + R + l^2 q^2 R \qquad (3.1.4.14)$$

and

$$p_{\sin} = lq\left[R + l(2 + lq^2 R)\right] \qquad (3.1.4.15)$$

This model is very similar to the core-shell model but, instead of having a sharp, well-defined shell, a diffusion zone is used. The diffusion zone model is often used in magnetic alloy systems where the interface is usually not well defined.

Structure factor

The scattering structure factor was defined in equation (3.1.4.6), and it accounts for the scattering due to particle-particle correlations. As mentioned above, the structure factor is negligible for low particle density. However as the particle density increases the structure factor becomes more and more important.

There are only very few cases for which the structure factor can be calculated analytically. The majority of which are results obtained from liquid state theory for particles with spherical symmetry interacting with a spherically symmetric potential. Due to the immense complexity of the calculations required to derive these structure factors, only the end results are quoted in this section.

Hard-sphere potential

In the hard-sphere potential the only assumption is that particles with radius R and volume fraction η will not overlap e.g. the particles are hard-sphere. The expressions for S(Q) have been calculated using Percus-Yevick approximation [11]

$$S_1(Q) = \frac{1}{1 + 24\eta G(RQ)/(RQ)} \qquad (3.1.4.16)$$

In this equation:

$$\begin{aligned} G(A) = {} & \alpha(\sin A - A\cos A)/A^2 \\ & + \beta(2A\sin A + (2 - A^2)\cos A - 2/A^3) \\ & + \gamma[-A^4\cos A + 4\left((3A^2 - 6)\cos A + (A3 - 6A)\sin A + 6\right)]/A^5 \end{aligned}$$

where

$$\alpha = (1 + 2\eta)^2/(1 - \eta)^4$$

$$\beta = -6\eta(1 + \eta/2)^2/(1 - \eta)^2$$

$$\gamma = \eta\alpha/2$$

A modified version of this hard-sphere structure factor with gamma distribution was used to model data with high particle density through out this work and a full description can be found in Refs. [12-13].

Experimental considerations

For small angle neutron scattering experiments, data are taken using an area detector. For analysis purposes it is convenient to reduce the data to one dimension with the scattering intensity as a function of the magnitude of the wave vector transfer q. During this reduction process we can also separate the magnetic scattering from the nuclear scattering, hence we can analyse nuclear and magnetic scattering independently. In this section we will describe the data reduction procedures for polarized and unpolarized small angle neutron scattering.

Page missing in original

One can recover the unpolarized neutron result in equation (3.1.4.17) by taking the sum of I^+ and I^-.

$$\left[I^+(Q,\alpha)+I^-(Q,\alpha)\right]/2 = I(Q,\alpha)_{non-polarized} \qquad (3.1.4.20)$$
$$= A(Q)+B(Q)\sin^2\alpha$$

Similarly to SANS above we can fit the data to equation (3.1.4.20) as a function of α to separate the magnetic scattering from the nuclear scattering.

Finally, the difference between the intensities of the two polarization states represents a magnetic-nuclear cross term,

$$\left[I^-(Q,\alpha)-I^+(Q,\alpha)\right]/2 = 2F_N F_M \sin^2\alpha \qquad (3.1.4.21)$$

Fitting equation (3.1.4.21) to the difference data can, in principle, give a different angular dependence to equations (3.1.4.17) and (3.1.4.20) if the structural and magnetic form factors have different spatial dependencies. However, if the structural and magnetic form factors are 100% correlated, one obtains the same result in each case.

Instrumentation

D11

Much of the SANS measurements were performed on the beam line D11 at ILL France. D11 provides a monochromatic neutron beam with incident wavelengths between 4.5Å and 40Å. The neutrons scattered from the sample are collected by a 64x64cm He^3 multi-detector, which is placed inside a 40m long evacuated tube. The large area detector allows each measurement to cover a large area in Q. Furthermore the detector is motorized and can be placed at any distance between 1.1m to 36.7m

from the sample position coving a Q range of 5×10^{-4} to 0.44 $Å^{-1}$. When the detector distance is small, high values of Q are accessed with good counting statistics whereas, when the detector distance is large, it is possible to focus on the low-Q region at the expense of scattering intensity. Figure 4.1.4.3 shows the layout of the D11 beam line.

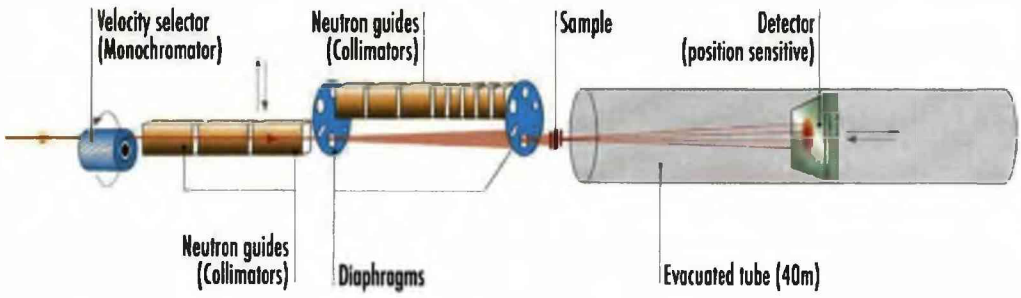

Figure 4.1.4.3 Schematic diagram of the D11 diffractometer, taken from [14].

V4

Similarly to D11, V4 is a neutron beam line optimized for SANS at HMI, Germany. V4 provides a monochromatic neutron beam with incident wavelengths between 3.8Å and 30Å. Again the neutron scattering from the sample is detected on a 64x64cm ^{3}He multi-detector, which in this case is placed inside a 16m long evacuated tube. Furthermore the detector is motorized and can be placed at any distance between 1m to 16m away from the sample position, covering a Q range of 1×10^{-3} to 0.85 $Å^{-1}$. However, the main difference between V4 and D11 is that V4 provides polarized incident neutrons using a polarizer and spin flipper. Thus, although the incident flux of neutrons is lower than the ILL at HMI, the sensitivity to magnetic scattering is enhanced by the use of polarised neutrons. Figure 4.1.4.4 demonstrates the layout of the V4 instrument.

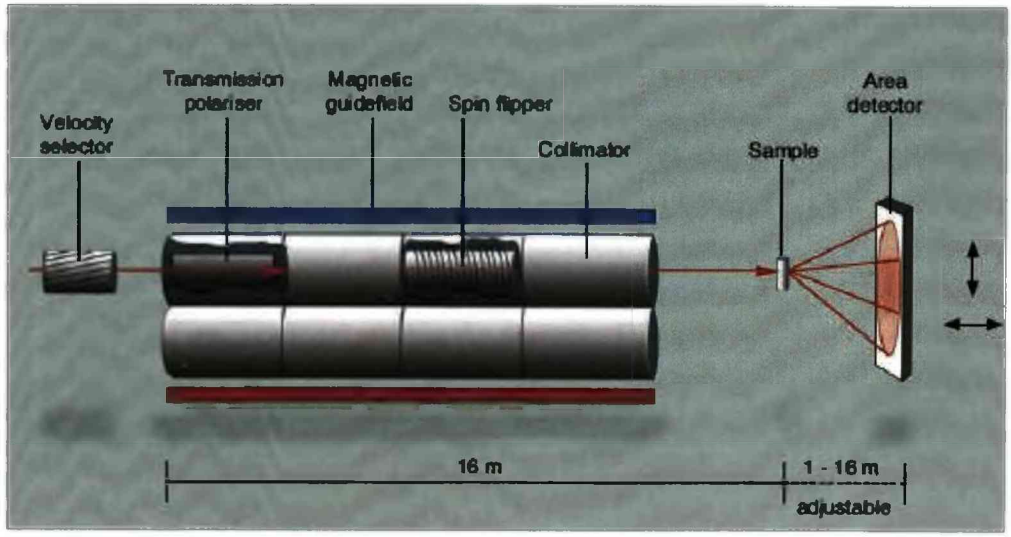

Figure 4.1.4.4 Schematic diagram of the V4 diffractometer [15].

3.1.5 X-ray reflectivity

Using grazing-incidence techniques, such as reflectivity, it is possible to focus on the near-surface region of samples. Beyond the region of total external reflection the reflectivity falls off rapidly with Q. The very high intensities available with x-rays mean that structural reflectivity measurements can be performed over a wide range of Q. Thus, x-ray reflectivity is ideal for studying the structure of multilayers and, in particular, the structures of the interfacial regions.

In this section I shall derive expressions for the x-ray reflexivity cross section. The optical nature of this technique means that one need only consider the refractive indices of the layers. This in turn depends upon the scattering length density rather than the actual arrangement of ions. Thus, the reflectivity does not depend on the crystallinity of samples. I shall begin with the derivation with Snell's law.

Theory

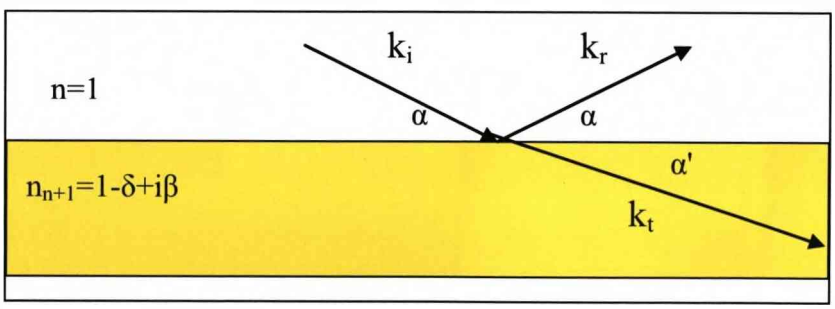

Figure 3.1.5.1: Snell's law and the Fresnel equation can be derived by considering the two components of wave-vector transfer, along and perpendicular to the surface.

Snell's law and the Fresnel equations are essential for calculating x-ray reflectivity. They can easily be derived by considering x-rays with wave vector k_i and incident angle α, see figure 3.1.5.1. Similarly, we have for the reflected wave k_r, α and k_t, α' for the transmitted wave. Each wave that arrives at the interface can be broken down into two components, one perpendicular to the surface and the other parallel to the surface. By imposing the boundary conditions that the wave and its derivative at

the interface must be continuous for both components, we obtain Snell's law and the Fresnel equation.

Snell's law [16] gives the relationship between the incident ray and the reflected ray in two adjacent media n and n+1. For the setting in figure 3.1.5.1 Snell's Law is:

$$n_n \cos\vartheta_n = n_{n+1} \cos\vartheta_{n+1} \qquad (3.1.5.1)$$

where n_n and n_{n+1} are the refractive indices in media n and media n+1 respectively. In air (~vacuum) the reflective index is unity. The refractive index for denser materials is given by:

$$n = 1 - \delta + i\beta \qquad (3.1.5.2)$$

For x-rays the values of α and β can be expressed in terms of the density of the atomic form factors:

$$\delta = \frac{2\pi\rho_a r_o}{k^2}(f^o + f') \qquad (3.1.5.3)$$

and

$$\beta = \frac{2\pi\rho_a r_o}{k^2} f'', \qquad (3.1.5.4)$$

where r_o is the classical electron radius, ρ_a is the atomic number density, f_o is the atomic form factor, f', and f'' are the dispersive corrections and k is $\frac{2\pi}{\lambda}$, where λ is the x-ray wavelength.

The Fresnel equations give the amplitude of reflectivity (r) and transmittivity (t), for the interface between the m^{th} and n^{th} layers:

$$r_{m,n} = \frac{Q_m - Q_n}{Q_m + Q_n} \qquad t_{m,n} = \frac{2Q_m}{Q_m + Q_n} \qquad (3.1.5.5)$$

where $Q_m = 2k\sin\alpha_m$. The intensity is the modulus of the square of the amplitude.

Kinematical approximation

It is possible to use an approximation to derive an analytical form of reflectivity from a multilayer. One approach is the Kinematical approximation. This approximation assumes that multiple reflections and refraction at interfaces are weak and can be ignored. Due to the lack of multiple reflections, the reflectivity from the multilayer structure can simply be calculated by summing the scattering amplitude from all N bilayers, and make suitable changes in their phase difference for the scattered wave from each bilayer. This method gives a good estimation at high wave-vector transfer. However, this approximation breaks down when the incident angle is close to the critical angle for total external reflection $\vartheta = \sqrt{2\delta}$.

Parratt's exact recursive method

Parratt's exact recursive method [17] uses dynamical theory and is a way of exactly calculating reflectivity from a multilayer of N layers on top of an infinitely thick substrate. The reflectivity from a multilayer system can be expressed in terms of the Fresnel coefficients, see figure 3.1.5.2. We first consider just two layers with an infinite bottom layer so that there are no multiple reflections from the this layer. Then the total reflectivity for the system is given by:

$$r_{slab} = r_{01} + t_{01}t_{10}r_{12}p^2 + t_{01}t_{10}r_{10}r_{12}^2p^4 \ldots\ldots\ldots\ldots \qquad (3.1.5.6)$$

p^2 is a phase factor which changes the phase of wave travelling in opposite directions and is generalised as $p^2 = \exp(id_nQ_n)$, with d being the thickness of the nth layer. By taking the geometric sum of the expression to infinity, and using two substitutions: $r_{01}^2 + t_{01}t_{10}^2 = 1$ and $r_{01} = -r_{10}$ this gives an expression for the (n-1,n) interface:

$$r_{n-1,n} = \frac{r'_{n-1,n} + r_{n,n+1}p_n^2}{1 + r'_{n-1,n}r_{n,n+1}p_n^2} \qquad (3.1.5.7)$$

where r' denotes reflectivity without multiple reflections. The Parrat procedure then consists of summation of $r_{n-1,n}$ terms starting from the bottom infinite substrate layer:

$$r'_{N,\infty} = \frac{Q_N - Q_\infty}{Q_N + Q_\infty} \qquad (3.1.5.8)$$

and it follows that the reflectivity from the next interface up in the stack is:

$$r_{n,n+1} = \frac{Q_n - Q_{n+1}}{Q_n + Q_{n+1}}. \qquad (3.1.5.9)$$

By continuing this process recursively until the reflectivity amplitude, $r_{0,1}$, where interface between the vacuum and the first layer is reached. This expression will give the amplitude of the reflectivity for a given Q. Then the measured intensity in an x-ray reflectivity experiment is the modulus of the square of this amplitude.

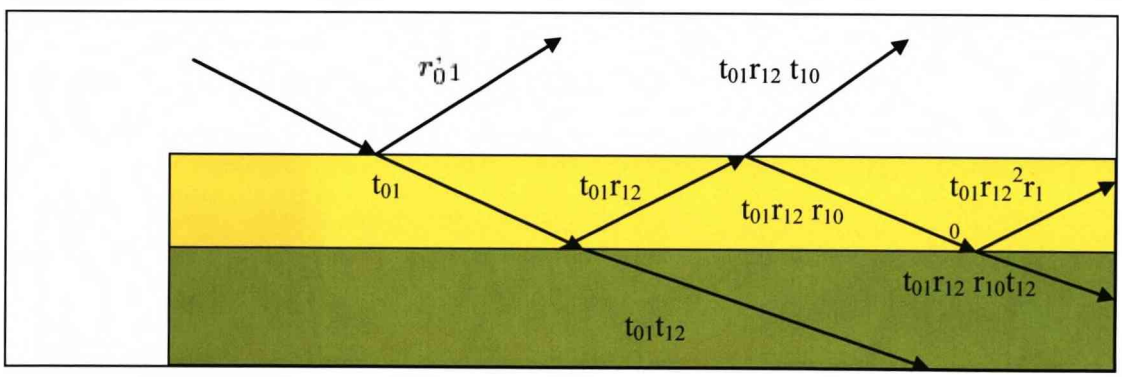

Figure 3.1.5.2: Reflection and transmission from a semi-infinite slab.

Rough Interfaces

The effect of roughness on the on-specular reflectivity is one which has undergone intense discussion [18-19], and different models have been tested. Here we will only discuss the model used by x-ray reflectivity program SPEEDO, which was used to fit all x-ray reflectivity spectra in this thesis. The program employs the

procedure of Nevot and Croce [19]. A pre-factor is introduced in the reflection coefficients so that:

$$r_{n,n+1} \rightarrow r_{n,n+1} \exp(-2\sigma_n k_n k_{n+1}) \qquad (3.1.5.10)$$

which assumes a Gaussian distribution of vertical roughnesses.

3.1.6 Polarised Neutron Reflectivity (PNR)

X-ray reflectivity and polarised neutron reflectivity can both be used to gain information from multilayer samples, regarding composition and interfacial roughness. However one major difference between the two techniques is the neutron's sensitivity to the sample magnetization. In this section, we will consider on-specular polarised neutron reflectivity on multilayer system and assume that the interfacial regions are perfectly flat, and that there is translational invariance in the *x-y* plane.

Theory

The Schrodinger equation for the wavefunction of a neutron in a solid $\psi(r)$ can be written in general:

$$\left[-\frac{\hbar^2}{2m_n} + V(r)\right]\psi(r) = E\psi(r), \qquad (3.1.6.1)$$

where m_n is the neutron mass, $V(r)$ is the potential energy and E is the total energy. Due to the translational invariance in the *x-y* plane, we only need to consider wavevector q_n that is perpendicular to the interface for region n. Then the solution to the Schrodinger equation is then:

$$\left[\frac{d^2}{dz^2} + q_n^2\right]\psi(z) \qquad q_n = \sqrt{\frac{2m_n}{\hbar^2}\left(\frac{(\hbar^2)k_\perp^2}{2m_n} - V_n\right)} \qquad (3.1.6.2)$$

where Vn is the interaction potential in layer n, and $k_\perp$ is the incident neutron wave vector perpendicular to the surface. The interaction potential now consists of a nuclear scattering term and a magnetic interaction term:

$$V_n = \frac{\hbar^2}{2\pi m_n}\rho_n b_n - \mu_n \cdot B_n, \qquad (3.1.6.3)$$

where μ_n ,b_n, B_n and ρ are the neutron moment, coherent nuclear scattering length, magnetic field, and atomic density, respectively.

In PNR measurements, the incident neutrons are polarised either parallel (+) or anti-parallel (-) to a small guide field. Polarisation analysis after reflection yields four cross-sections (++), (--), (+-), (-+) referring to the incident and scattered spin state, respectively. The total reflectivity from the region N can then be written as a 2x2 matrix:

$$r_{1..N} = \begin{pmatrix} r_{1..N}^{++} & r_{1..N}^{+-} \\ r_{1..N}^{-+} & r_{1..N}^{--} \end{pmatrix}. \qquad (3.1.6.4)$$

The total reflectivity from a multilayer can be calculated using the transfer matrix method. However, this method is too complex to cover in detail here. For a complete derivation see Blundell and Bland, Ref. [20]. The method makes use of the transfer matrix to calculate the transmission and reflection coefficients, hence the total reflectivity. An alternative method is an optical method [21] in which the total reflectivity is calculated recursively, similarly to Parratt's exact recursive method used earlier for x-ray reflectivity. For each bilayer the reflectivity is:

$$r_{j,N} = r_{j,j+1} + t_{j,j+1}P_{j+1}r_{j+1..N}P_{j+1} \times (I - (r_{j+1,j}P_{j+1}r_{j+1..N}))^{-1} t_{j+1,j} \qquad (3.1.6.5)$$

for j=n-2, n-1....,1 in that order, substituting the result of each calculation into the following one. I is a unit matrix and P is the propagation matrix given by,

$$P_j = \begin{pmatrix} \exp i(q_k^+ d_j) & 0 \\ 0 & \exp i(q_k^- d_j) \end{pmatrix}. \qquad (3.1.6.6)$$

The reflection and transmission matrix coefficients are

$$r_{1..N} = \begin{pmatrix} r_{j,j+1}^{++} & r_{j,j+1}^{+-} \\ r_{j,j+1}^{-+} & r_{j,j+1}^{--} \end{pmatrix} \qquad (3.1.6.7)$$

$$t_{1..N} = \begin{pmatrix} t_{j,j+1}^{++} & t_{j,j+1}^{+-} \\ t_{j,j+1}^{-+} & t_{j,j+1}^{--} \end{pmatrix} \qquad (3.1.6.8)$$

One advantage of this scheme over an equivalent treatment using transfer matrices is that the interface reflectivites can be directly modified by a Debye-Waller factor to model the spin dependent specular roughness. Thus for interface *j*:

$$r_{j,j+1}^{\sigma_1\sigma_2} \rightarrow r_{j,j+1}^{\sigma_1\sigma_2} \exp\left(-\frac{1}{2} q_j^{\sigma_1} q_{j+1}^{\sigma_2} (\Delta z_j)^2 \right), \qquad (3.1.6.9)$$

where σ denotes the spin state for incident and reflected neutrons, ΔZ_j is the root-mean-square roughness at interface *j*.

Instrumentation

D17

D17 is able to operate in three modes, time-of-fight (TOF), monochromatic and polarizing, see figure 3.1.6.1. For our work on D17 we were interested primarily in the spin flip reflectivity, therefore polarised mode was used throughout the whole D17 experiment.

In polarised neutron reflectivity mode the incident neutron beam must be spin polarised and in addition the scattered beam must be analysed to determine the polarisation state. The polarisation of the incident beam is achieved by the polarising

monochromator and the incident polarization state is selected using a spin flipper. In addition, a spin flipper and a ^{3}He analyser were positioned in the scattered beam path before the 2D detector to measure all four polarisation channels. The advantage of ^{3}He over analyzer mirrors is that polarization analysis can also be applied to the off-specular scattering. The ^{3}He analyser needed to be replaced every 24 hours and correction had to be made for the decay in the polarization of the ^{3}He.

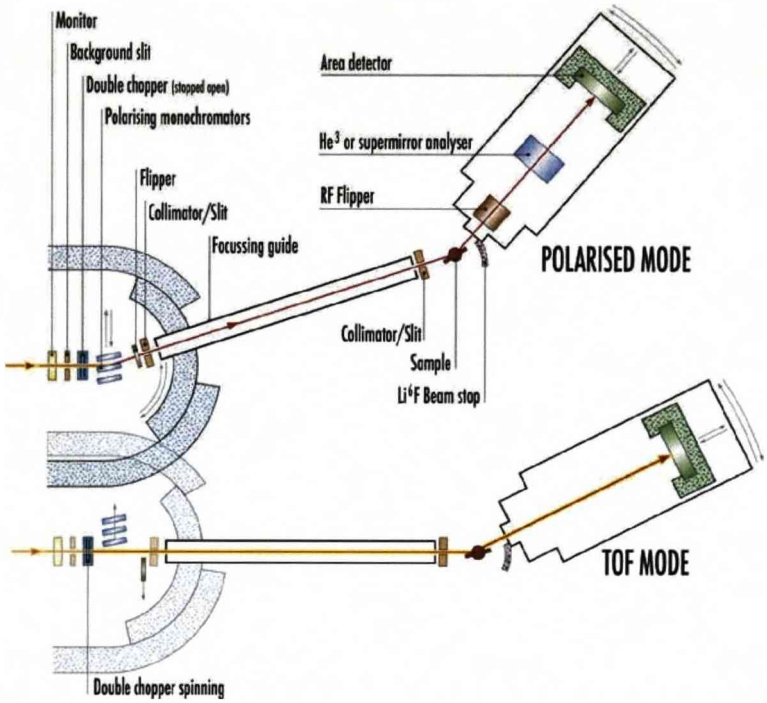

Figure 4.1.6.1 Schematic diagram of the D17 diffractometer [22].

3.2 SQUID Magnetometry

3.2.1 Theory

A Superconducting Quantum Interference Device (SQUID) is a device that measures the total magnetization of a sample with the highest precision available. This is important when dealing with the tiny amounts of material typically present in magnetic nanostructures. In order to gain an understanding of this device, we must first consider the behavior of a current within a superconducting ring. This is followed

by consideration of the effect of an external field on this superconducting ring, and then finally a ring with two Josephson junctions.

Let us first consider a superconducting ring without a magnetic field or Josephson junctions. In such a ring the electrons within the system pair up via the phonon interaction, to form Cooper pairs. These Cooper pairs can be represented by a wavefunction of the form:

$$\psi_p = \psi_0 \exp\left(\frac{i(P \cdot r)}{\hbar}\right) \tag{3.2.1.1}$$

where P is the net momentum of the pair and the centre of mass is at r. The Cooper pair experiences no scattering from the lattice sites, resulting in a large mean free path, and zero resistance. The Cooper pairs inside a superconducting ring can be considered to be phase coherent. Due to this phase coherence, London and London concluded that the flux is quantised and this quantised flux is known as fluxons [23]. A fluxon, Φ_0 is defined as:

$$\Phi_0 = \frac{h}{2e} = 2.07 \times 10^{-15} \mathrm{Tm}^{-2} \tag{3.2.1.2}$$

Consider a superconductor with two Josephson junctions, see figure 3.2.1.1. The result of having the Josephson junctions is that the two superconducting regions are isolated from each other. The phases of the Cooper pairs within each segment of the superconductor are now unrelated. Josephson junctions are thin, non-superconducting "weak links", where the Cooper pairs can quantum mechanically tunnel through the gap without the breakage of the pairs. The current i_s flowing in a Josephson junction is given by

$$i_s = i_c \sin(\Delta\phi), \tag{3.2.1.3}$$

where i_c is the critical current of the junction and $\Delta\phi$ is the phase difference across the junction. For the case where the circulating current is small so no fluxon are

produced by this circulating current, then the flux inside the ring can be approximated by the applied flux only. The phase change $\Delta\phi$ is defined as $\delta_a - \delta_b$, where δ_a and δ_b are the phase differences at the two Josephson junctions. Furthermore the quantum condition requires that the phase change around the closed ring must be $n2\pi$, where n is an integer. Thus we can write:

$$\delta_a - \delta_b = 2\pi \frac{\Phi_a}{\Phi_0} \tag{3.2.1.4}$$

where Φ_a is the flux in the loop due to the applied field. The total current flow I through the junctions is given by [24]

$$I = i_{ca} \sin\delta_a + i_{cb} \sin\delta_b , \tag{3.2.1.5}$$

where i_{ca} and i_{cb} are the critical currents in the two junctions. Given that the two junctions are identical e.g. $i_c = i_{ca} = i_{cb}$. Equation 3.2.1.5 becomes

$$I = 2i_c \cos\left(\frac{\delta_a - \delta_b}{2}\right)\sin\left(\frac{\delta_a + \delta_b}{2}\right) \tag{3.2.1.6}$$

Substituting equation (3.2.1.4) into equation (3.2.1.6) and noting that the sine function cannot be greater than unity, an equation relating the measured (maximum) supercurrent $I_{\max}$ to the applied flux is given by:

$$I_{\max} = 2i_c \left|\cos\left(\frac{\Phi_a}{\Phi_0}\right)\pi\right| . \tag{3.2.1.7}$$

The Josephson junctions gives a way of measuring a sample magnetisation placed inside the ring if i_c is known.

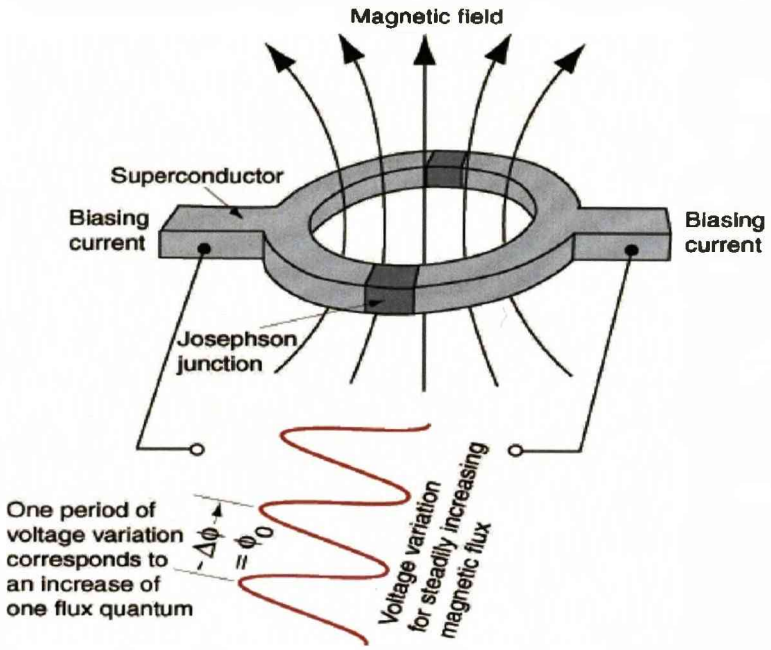

Figure 3.2.1.1: A schematic diagram of a ring with 2 Josephson junction[25].

3.2.2 Instrumentation

The SQUID data presented in this work were obtained using an RF Quantum Design Magnetic Property Measurement System (MPMS) XL SQUID magnetometer. This design contains a superconducting loop with two Josephson Junctions. The SQUID provides a temperature control environment with temperature range of 1.8K to 400K with an accuracy of 0.01K, and a superconducting electromagnet able to produce a magnetic field up to 7T with an accuracy of 1×10^{-5} T.

The SQUID consists of an inner liquid reservoir surrounded by a liquid nitrogen region to reduce excessive liquid helium boil off. The liquid helium is used to maintain the electromagnet in a superconducting state and for cooling the sample space.

Samples are mounted in a plastic straw-like sample holder that is connected to the end of a sample rod which is inserted into the SQUID. The other end of the sample rod is attached to a stepper motor which is used to position the sample and provide the oscillation needed for measurements.

The pickup coils are configured as highly balanced second-derivative coils that reject applied field from the superconducting magnet to a resolution of 0.1%.

Bibliography

[1] G.L Squires, Thermal neutron scattering, Cambridge University press.

[2] Jens Als-Nielsen, Des McMorrow, Elements of Modern X-Ray Physics, John Wiley & Sons, Ltd.

[3] D.A. Jehan, D.F. McMorrow, R. A. Cowley, R.C.C. Ward, M. R. Well, and N. Hagmann, K. N. Clausen Phys. Rev B, 48 8.

[4] M.J. Cooper and R. Nathans. Acta Crystallogr., 23:357,1967

[5] Guinier, Fournet, Walker, Yudowitch, Small-angel scattering of x-rays. Wiley & Sons, Ltd

[6] Michael Kotlarchyk and Sow-Hsin Chen, J.Chem. Phys. 79(5). (1983)

[7] Jan Skov Pedersen, Advances in Colloid and Interface science 70 171-210 (1997)

[8] Lord Rayleigh, Proc. Roy. Soc. London, Ser. A, 84 (1911) 25-38.

[9] A. Wiedenmann, Physica B 297 226-233 (2001)

[10] A. Heinemann, J.Appl. Cryst. 33,1386 (2000)

[11] D.J. Kinning and E.L. Thomas, Macromolecules, 17 1712-1718 (1984)

[12] W.L. Griffith, R. Triolo, and A.L. Compere, Phys. Rev A 33 3 (1986)

[13] W.L. Griffith, R. Triolo, and A.L. Compere, Phys. Rev A 35 5 (1987)

[14] http://www.ill.eu/d11/home-d11/

[15] http://www.hmi.de/bensc/instrumentation/instrumente/v4/v4_en.htm

[16] E. Hecht. Optics. Optics Addison-Wesley, 1998.

[17] L.G. Parrat. Phys. Rev.,95:359, 1954.

[18] P. Croce and Nevot. Rev. Phys. Appl., 11:113,1976.

[19] Nevot and P.Croce. Rev. Phys.Appl.,15:761,1980.

[20] S.J. Blundell and J.A.C. Bland. Phys. Rev. B, 46:3391,1992.

[21] S.J. Blundell and J.A.C. Bland. J. Magn. Magn. Mater., 121:185,1993.

[22] http://www.ill.eu/d17/home-d17/

[23] F. London. Proc. Roy. Soc (London), 152(24), 1935.

[24] B.D. Josephson. Physics Letters, 1:251,1962.

[25] http://hyperphysics.phy-astr.gsu.edu/hbase/solids/squid.html

Chapter 4

Fe/MgO Multilayers

4.1 Motivation

Tunnel magnetoresistance (TMR) in magnetic tunnel junctions [1,2] is the key to developing magnetoresistive random-access memory (MRAM), magnetic sensors and novel programmable logic devices [3-5]. A Giant room-temperature magnetoresistance ratio up to 1000% was predicted, however only a fraction of this value is observed [6,7]. Many believed this discrepancy is due to an imperfect interface, however, the junctions prepared by Yuasa *et al.* are believed to have ideal Fe/MgO without mixing [6]. In contrast, Meyerheim *et al.* found an interfacial FeO layer [8]. *Ab initio* calculations by Heiliger *et al.* using these and other interface structures show that even the sign of the TMR ratio depends on the interface structure [9].

Interlayer magnetic coupling has been observed for Fe/MgO/Fe using bulk magnetometry [10-13]. For thin barrier thicknesses AF coupling is observed, and the results agree with theoretical models using spin-polarised quantum tunnelling of electrons between ferromagnetic layers [14,15]. For larger spacer layer thicknesses FM coupling is observed, and this is attributed to the "Orange Peel" interaction associated with correlated roughness of the FM/insulator interfaces [16].

The motivation for studies of Fe/MgO multilayers is to study the nature of magnetic coupling between the iron layers. The extra artificial periodicity introduced in multilayers can potentially gives detailed information on the interfacial structure and structural coherence by using synchrotron X-rays and the magnetic ordering can be studied using PNR.

4.2 Introduction

In this chapter I shall present detailed structural and magnetic studies of Fe/MgO multilayers, after describing the sample growth and experimental techniques. Then I shall describe a high-angle x-ray diffraction study, which yields information on the structural coherence of the system and the level of interdiffusion between the two constituents. This is followed by x-ray reflectivity and high resolution tunnelling electron microscopy, techniques that give an insight into the details of the interfacial roughness and bilayers thickness. After establishing the structural model of the system, I shall present SQUID and PNR results to determine the magnetic structure of this system, and its affect on the physical properties.

4.3 Sample Growth

All samples studied in this chapter were grown at the Clarendon Laboratory, Oxford. Single-crystal FCC MgO substrates were used, with MgO (001) in the epitaxial plane. The substrates had a dimension of 1.2cm by 1.0cm and a thickness of 0.1cm. Prior to growth the MgO(001) substrates were degreased by boiling in trichloroethylene, isopropyl alcohol, and methanol. In both cases 50Å of MgO seed layer was grown at 500°C. Thereafter multilayers of nominal composition $[Fe(50Å)/MgO(6Å)]_{20}$ and $[Fe(50Å)/MgO(20Å)]_{20}$ were grown at ambient temperature with growth rates of 0.3Å/s and 0.1Å/s for the Fe and MgO, respectively. The Fe cubic unit cell shares the same growth (c-axis) as the MgO cubic cell, but the Fe a-b axes are rotated relative to MgO about the c-axis by 45°, so that the Fe(001)[100] is parallel to the MgO (001)[110]. The growth directions are summarised in Figure 4.3.1. Finally, the samples were capped with 100 Å of copper to prevent oxidation [17]. A schematic diagram of the multilayer composition is shown in Figure 4.3.2.

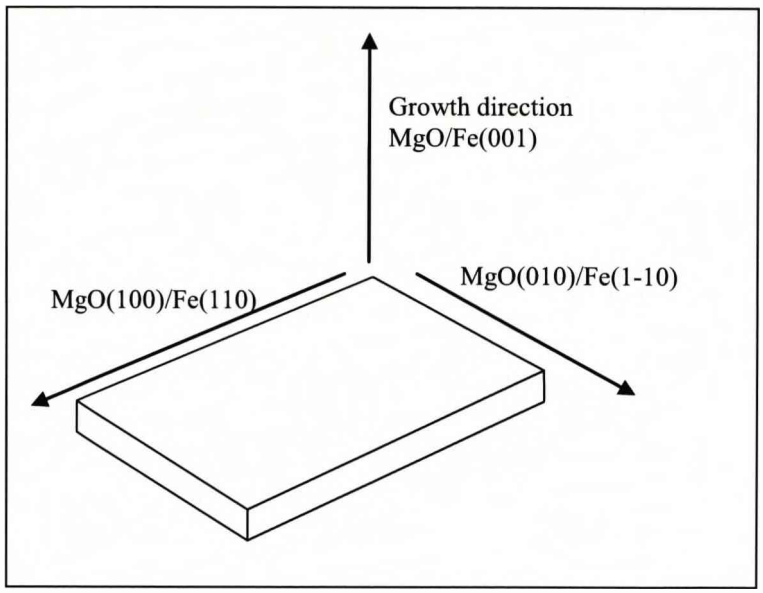

Figure 4.3.1: Epitaxial relationship between the Fe and the MgO substrate. The Fe a-b axes are rotated by 45° about the c-axis.

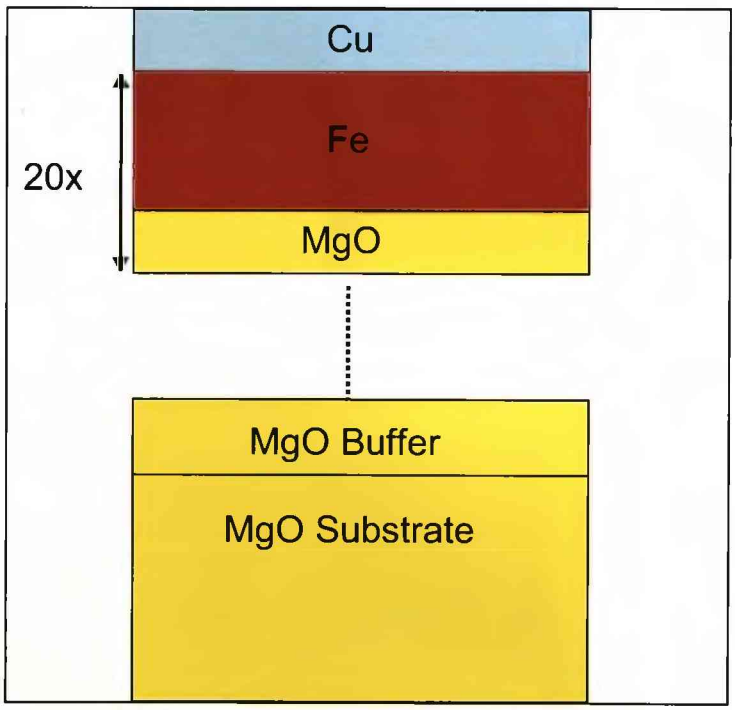

Figure 4.3.2: A schematic diagram of an Fe/MgO superlattice.

4.4 Experimental procedure

High-angle x-ray diffraction and low-angle x-ray reflectivity measurements for structural analysis were performed using I16 beamline at Diamond, with incident x-ray energy of 10kev. Further studies were performed using the in-house Philips X-Pert diffractometer with Cu Kα radiation at incident energy of 8.048kev. Both sets of measurements were taken at room temperature.

SQUID measurements were performed using a Quantum Design MPMS magnetometer. All measurements were taken at room temperature with the Fe [110] in-plane direction parallel to the applied field.

Transmission electron microscopy (TEM) was performed by Chao Wang of the Department of Materials in Oxford University to examine the samples in a cross-sectional view. The contrast modes were high-resolution (HREM) in a JEOL 4000EX microscope and high angle annular dark field (HAADF) in a JEOL 3000F field-emission microscope operated in a scanning mode.

Polarised neutron reflectivity, PNR, was performed on both multilayers, using the D17 diffractometer at the ILL. The samples were mounted with the Fe [110] in-plane direction parallel to the direction of the magnetic guide field, following the orientation used for the SQUID measurements. This guide field was kept constant throughout the experiment and always had a value of 0.001T. On- and off-specular reflectivity data were taken at the same time using a 2D detector, and a ^{3}He analyzer was used with incident neutron wavelength of 5.387Å. Both non-spin-flip and spin-flip reflectivities were measured in each given scan. In order to cover a broad enough range of wave-vector transfer, Q, these scans were performed in three parts. Each part had some overlap in Q with the next so that scans could be combined after the time-dependent ^{3}He analyzer efficiency correction.

4.5 Structural characterization of Fe/MgO superlattices

4.5.1 High-angle X-ray diffraction

Figure 4.5.1.1 shows an x-ray diffraction scan taken using the Philips X-pert diffractometer along the [00L] direction for Fe(50Å)/MgO(20Å)]$_{20}$, showing the Fe (002) peak. The structural coherence length was estimated to be about 53Å, using $\xi=2\pi/\Delta Q$ where ΔQ is the FWHM of the Bragg reflection. This result suggests that the superlattices are only structurally coherent within one layer of Fe. However Figure 4.5.1.2 taken using I16 shows the high-angle x-ray scan through the same Fe (002) Bragg peak for the same sample. It is clear that the synchrotron measurements are much more sensitive, and by comparing the two data sets we see extra reflections around the main Bragg peak for the I16 data. It might be reasonable to assume that the oscillations either side of the most intense Bragg peak are multilayer reflections due to extra periodicity from the bilayer repeat, since these are frequently observed with multilayers systems. However this is not the case here. Figure 4.5.1.2 shows a simulation for the [Fe(50Å)/MgO(20Å)]$_{20}$ superlattice with structural coherence of 20 bilayers. This simulation shows sharp superlattice Bragg peaks either side of the most intense Bragg peak, which are ΔQ apart, where $\Delta Q=2\pi/$(bilayer thickness). Further inspection of the data and the simulation shows that the observed oscillations are not multilayer reflections. It is clear that this sample does not possess sufficiently long-range structural coherence for the observation of multilayer reflections.

The diffraction data for both Fe(50Å)/MgO(6Å)]$_{20}$ and Fe(50Å)/MgO(20Å)]$_{20}$ are shown in figure 4.5.1.3. Simulations were performed assuming a structural coherence of just two bilayers, and they are shown as solid lines in figure 4.5.1.3. This simple model captures the main features in the scattering data, the oscillation period and the peak intensity. Furthermore, the simulation model also provides useful information on the interfacial diffusion between the Fe and MgO blocks, the number of planes of each constituent and the individual lattice parameters. The lattice

constants obtained by the simulation are close to the bulk values for Fe and MgO. These fitted parameters are given in Table 4.5.1.1. It is important to note that the interfacial diffusion values indicate that the interfaces of these samples are well defined on the atomic scale, i.e. there is very little intermixing between the Fe and MgO atoms. Finally, the mosaic spreads of each sample are also included in Table 4.5.1.1. Mosaic spreads are obtained by rotating the sample about an axis perpendicular to the scattering plane, and these scans explore in-plane coherence and crystal mosaicity in the sample. Studies of other transition metal and rare-earth superlattices suggest that the sharpest interfaces have broad mosaic, as observed here. Figure 4.5.1.4 shows the scattering for [Fe(50Å)/MgO(20Å)]$_{20}$ over a wider range of Q. Further oscillations near to the bulk MgO (0 0 2) reflection are visible, but the results are obscured by the scatting from the substrate.

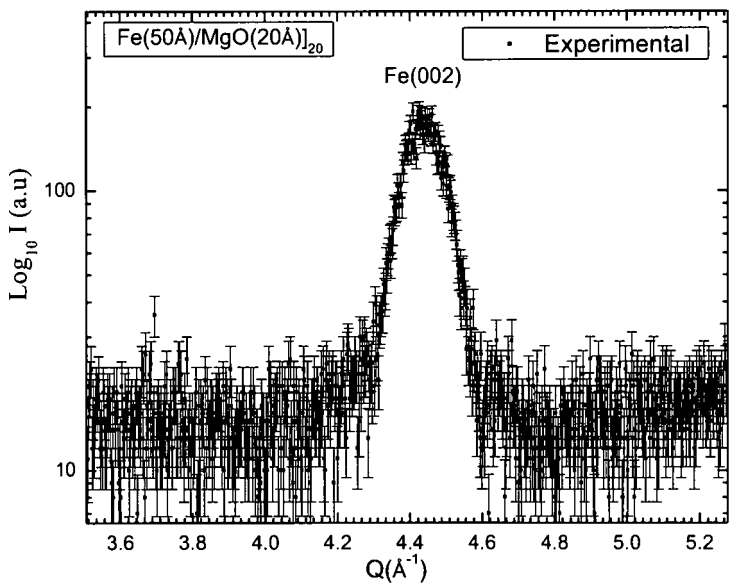

Figure 4.5.1.1: Structural X-ray diffraction through the Fe (0 0 2) Bragg reflection for [Fe(50Å)/MgO(20Å)]$_{20}$ using the Philips X-pert diffractometer, showing no indication of any peaks around the Fe(002).

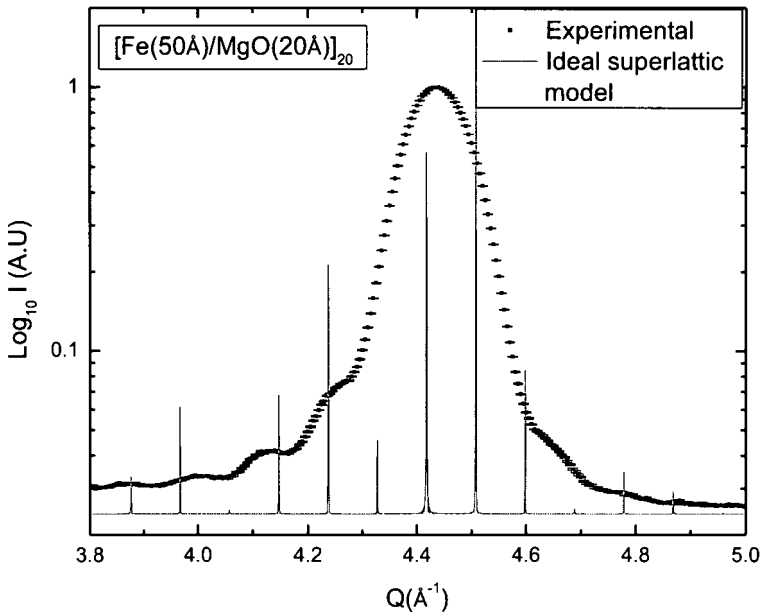

Figure 4.5.1.2: Structural x-ray diffraction through Fe (0 0 2) Bragg reflection for Fe(50Å)/MgO(20Å)]$_{20}$. The green line shows the calculated ideal X-ray scattering from a fully coherent superlattice structure.

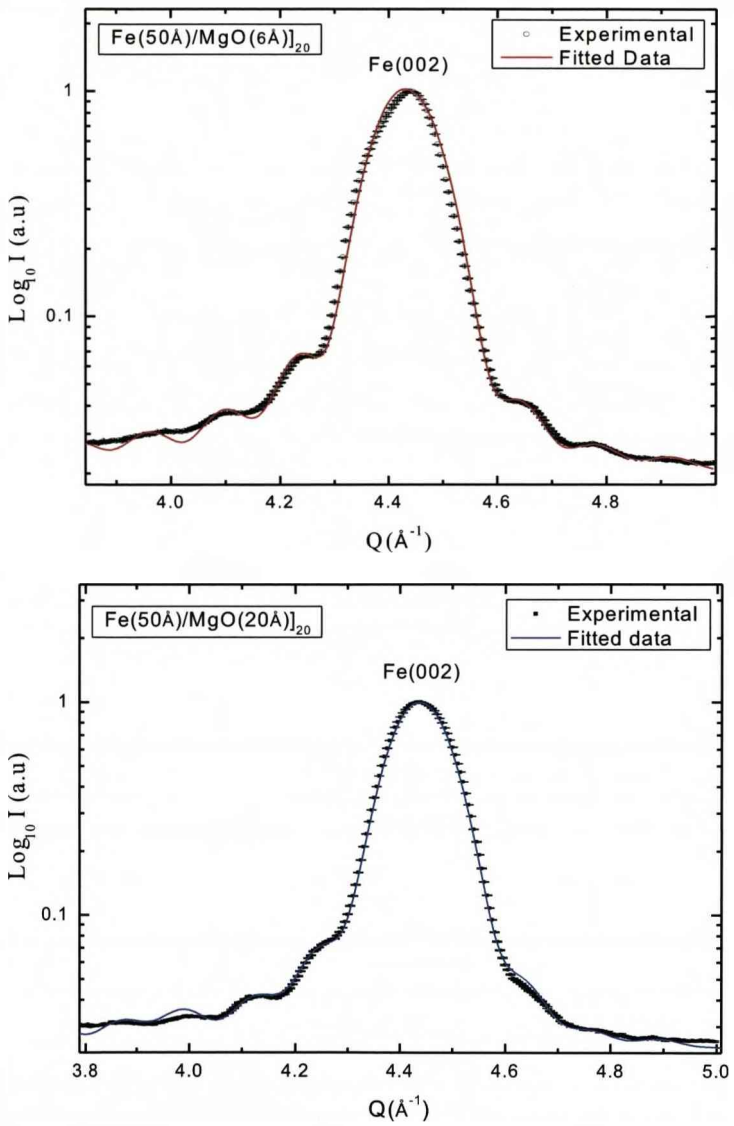

Figure 4.5.1.3: Structural x-ray diffraction through the Fe (0 0 2) Bragg reflection for $[Fe(50\text{Å})/MgO(6\text{Å})]_{20}$ *and* $[Fe(50\text{Å})/MgO(20\text{Å})]_{20}$ *synchrotron x-rays on I16. The solid lines show fits to the data for a structural model with coherence over just two bilayers.*

Nominal composition	cFe ±0.005Å	cMgO ±0.005Å	Bilayer thickness ±1.0Å	Structural coherence ±1.0Å	Mosaic spread ±0.02°	Interfacial diffusion ±0.5 plane
$[Fe(50Å)/MgO(6Å)]_{20}$	2.833	4.212	53	106	2.18	0.8
$[Fe(50Å)/MgO(20Å)]_{20}$	2.835	4.214	72	96	2.02	0.8

Table 4.5.1.1: Structural parameters obtained from x-ray diffraction for $[Fe(50Å)/MgO(6Å)]_{20}$ and $[Fe(50Å)/MgO(20Å)]_{20}$ superlattices.

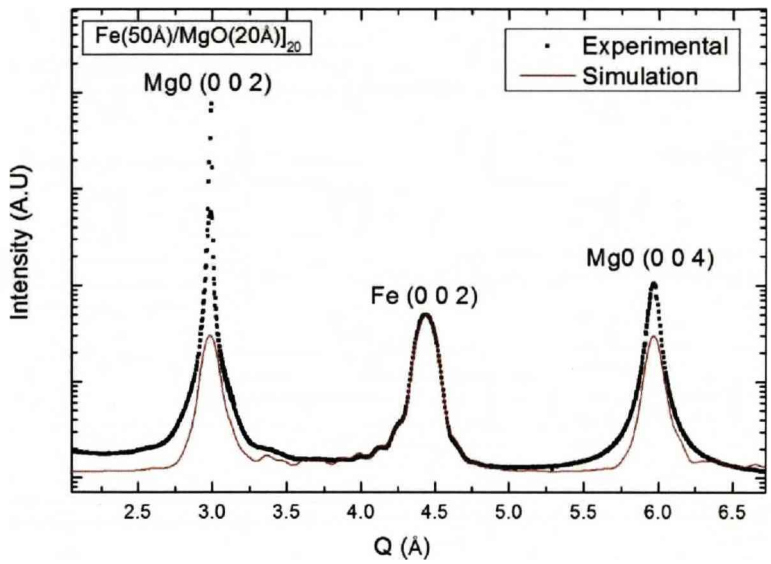

Figure 4.5.1.4 Structural x-ray diffraction along the [00L] direction. The red line through the data points is a simulation showing the presence of extra peaks close to the positions of the bulk Fe and MgO Bragg reflections. However, the scattering in the vicinity of the MgO reflections is obscured by the stronger scatting from the substrate.

4.5.2 X-ray reflectivity

Figure 4.5.2.1 shows the specular x-ray reflectivities for $[Fe(50\text{Å})/MgO(6\text{Å})]_{20}$ and $[Fe(50\text{Å})/MgO(20\text{Å})]_{20}$ at room temperature. At low angles one is not sensitive to the crystallinity. The SPEEDO programme by Knewtson and Suter [18] was used to model the electron density profile over the whole stack. The model shows exceptionally good agreement with the data, capturing all observed Bragg reflections up to 4^{th} and 5^{th} order for $[Fe(50\text{Å})/MgO(6\text{Å})]_{20}$ and $Fe(50\text{Å})/MgO(20\text{Å})]_{20}$, respectively. The fitted parameters are summarized in table 4.5.2.1. One may notice that the roughness parameters given by reflectivity are much larger than those obtained using x-ray diffraction. This is presumably because the reflectivity averages over a much larger area of the sample and over many domains, whereas the diffraction sees a small coherent region over one domain.

On the question of the presence of an FeO layer at the interface, it is not possible to distinguish with these specular x-ray results. Figure 4.5.2.2 shows the reflectivity profile for an intermediate oxide layer, but no roughness. It is clear that roughness would need to be introduced in order to suppress the intensities of the higher order reflections. However, the electron density of the FeO is between that of the Fe and the MgO, and it is then impossible to separate the effect of the intermediate oxide layer from the roughness.

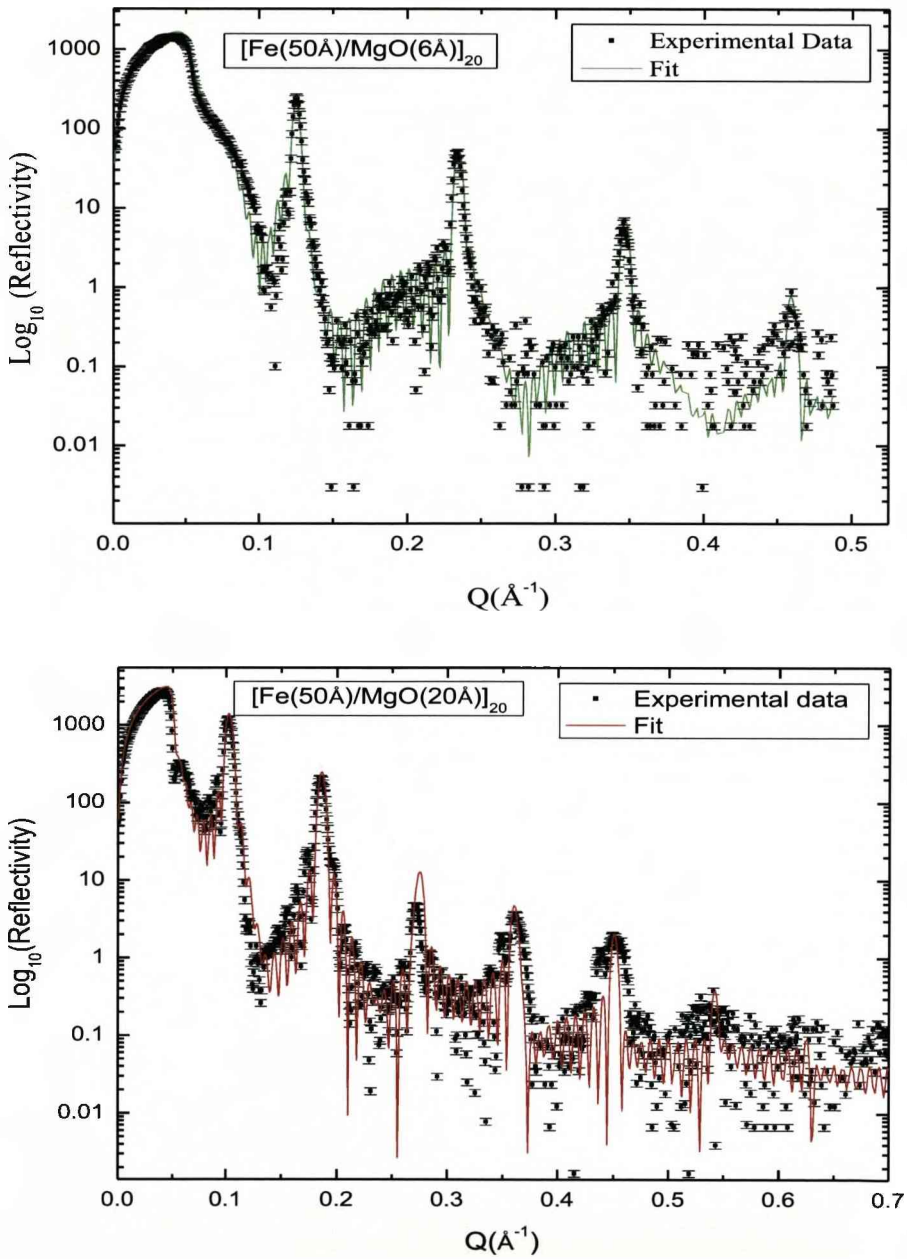

Figure 4.5.2.1: X-ray reflectivity for [Fe(50Å)/MgO(20Å)]$_{20}$ and [Fe(50Å)/MgO (20Å)]$_{20}$. The solid lines show the fitted reflectivities.

Nominal composition	Fe block thickness ±0.2Å	MgO block thickness ±0.2Å	Bilayer thickness ±0.3Å	Roughness MgO/Fe ±0.2Å	Roughness Fe/MgO ±0.2Å
$[Fe(50Å)/MgO(6Å)]_{20}$	47.6	7.5	58.1	7.1	3.8
$[Fe(50Å)/MgO(20Å)]_{20}$	49.7	20.4	70.1	6.5	3.4

Table 4.5.2.1: Structural parameters obtained from x-ray reflectivity for $[Fe(50Å)/MgO(6Å)]_{20}$ and $Fe(50Å)/MgO(20Å)]_{20}$ superlattices.

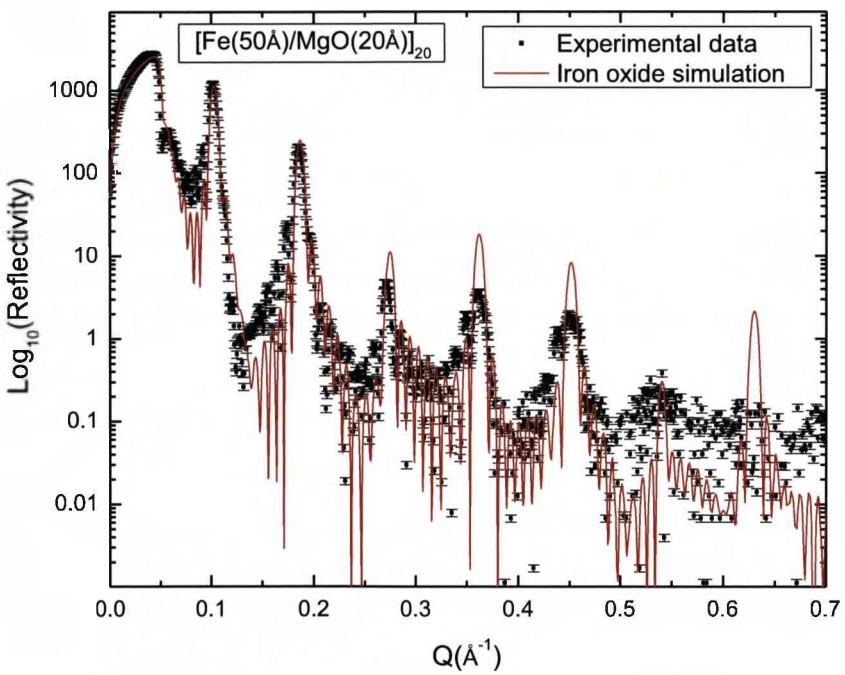

Figure 4.5.2.2: X-ray reflectivity from $[Fe(50Å)/MgO(20Å)]_{20}$ compared with the calculated reflectivity from an ideal iron oxide layer in between the Fe and MgO blocks.

4.5.3 Transmission electron microscopy (TEM)

Figure 4.5.3.1 is an HAADF image, which presents an overview of the [Fe(50Å)/ MgO(6Å)]$_{20}$ multilayer structure. The image shows a clear contrast between the Fe and MgO layers suggesting no significant interdiffusion between Fe and MgO. The uncorrelated roughness across the multilayers was studied using a series of line profiles along the growth direction with a width of approximately 2.8 nm. These line profiles were examined every 10 nm across the field of view in order to determine variations in the thickness of an Fe/MgO repeat unit. For the [Fe(50Å)/MgO(6Å)]$_{20}$ sample, no significant variations were found between the repeat layers and across the field of view resulting in an average thickness of 53Å. Therefore, within the limited field of view of this image, no significant in-plane roughness was detected. The standard deviation of all the measurements, which is indicative of the out-of-plane roughness of these layers, is 2.9Å. The reason for the lower roughness than x-ray reflectivity is partly due to the limited resolution due to pixel size, and partly because the average is performed over a much smaller region of the sample. However, the TEM images give a good qualitative picture of what the interfacial roughness looks like. Figure 4.5.3.2 and Figure 4.5.3.3 are HREM images of [Fe(50Å)/MgO(6Å)]$_{20}$. The presence of pinholes can be observed for thin MgO thicknesses, while for the thicker MgO layers pinholes were not observed. Close inspection of several images reveals the presence of correlated, wavy roughness, see Figure 4.5.3.3

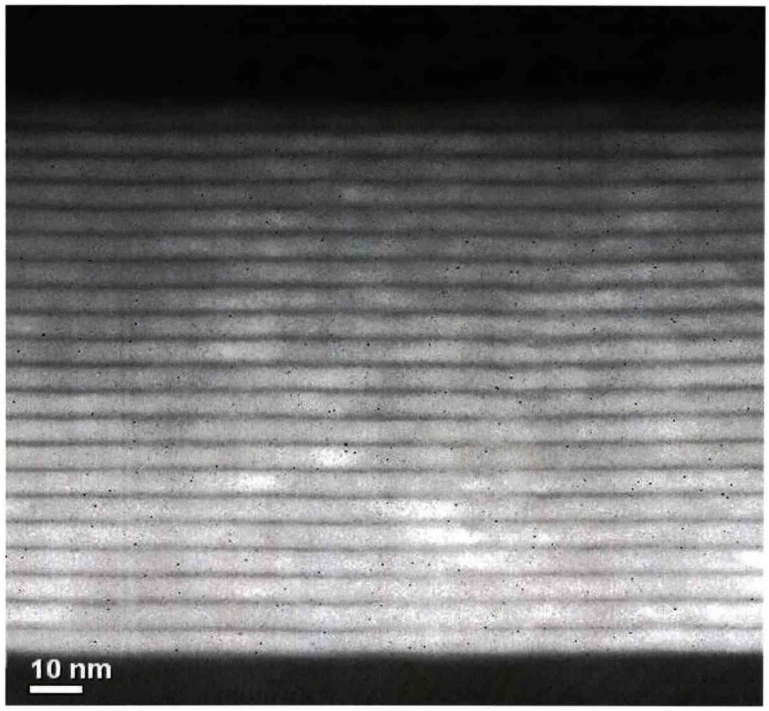

Figure 4.5.3.1 HAADF image of the [Fe(50Å)/MgO(6Å)]$_{20}$ multilayer in cross-sectional view with zone axis Fe[100] | MgO[110].

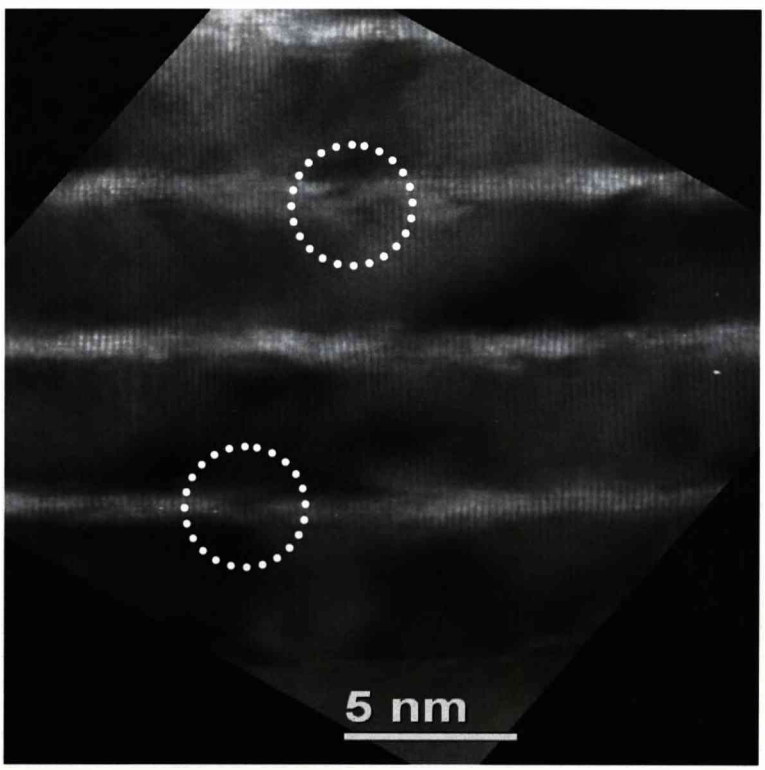

Figure 4.5.3.2: HREM image of the [Fe(50Å)/MgO(6Å)]$_{20}$ multilayer in cross-sectional view. Circles highlight pin holes in MgO layer.

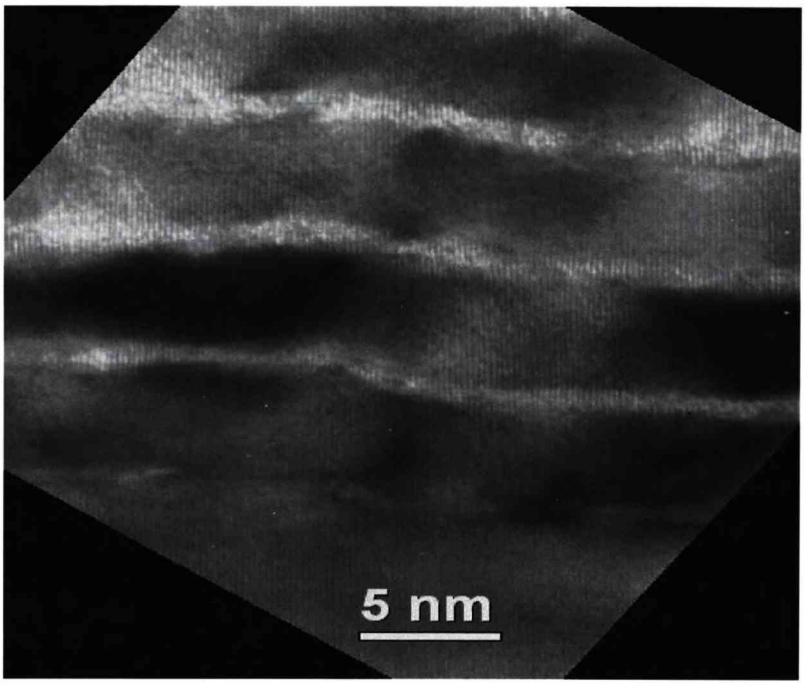

Figure 4.5.3.3: HREM image of the [Fe(50Å)/MgO(6Å)]$_{20}$ multilayer in cross-sectional view, showing wave like correlated roughness..

4.5.4 Summary of all structural results

MBE grown Fe/MgO multilayers with different barrier layer thicknesses have been studied using high-angle x-ray diffraction, x-ray reflectivity and high resolution tunnelling electron spectroscopy. These samples have shown very well defined multilayer structures with very little interdiffusion, typically below one atomic layer. However, their crystalline coherence lengths are confined to just two bilayers. Reflectivity measurements revealed that the roughness between the interfaces is rather high with typical values of 6.5-7.1 for MgO on Fe and 3.4-3.8 for Fe on MgO. These roughnesses could be consistent with those estimated over much smaller regions within the sample using x-ray diffraction and HAADF. Interestingly, HREM also shows that these roughnesses are sometimes correlated. Finally, the presence of pinholing for samples with MgO thicknesses below 6Å was observed, but once the MgO thickness reached 10Å no pinholing was detected.

4.6 Magnetometry Measurements

4.6.1 Introduction

In much of the literature written on Fe/MgO junction systems, the nature of the coupling between the ferromagnetic Fe blocks is believed to vary as a function of MgO thickness, with MgO thickness below 12Å anti-ferromagnetically (AF) coupled and ferromagnetically (FM) coupling for MgO thickness greater than this value [10]. In this section I shall investigate the magnetic coupling of the Fe/MgO multilayers with different thicknesses of MgO using SQUID magnetometry. This will form the link to the magnetic coupling as a function of MgO thickness in junctions. Then the magnetic ordering will be investigated in much greater detail using PNR.

4.6.2 Result

$Fe(50Å)/MgO(6Å)]_{20}$

The hysteresis loop for the $[Fe(50Å)/MgO(6Å)]_{20}$ multilayer is shown in Figure 4.6.2.1. For low fields, some of the magnet moment aligns almost immediately with the field. This observation could be caused either by a small amount of FM coupled Fe layers or uncoupled Fe layers, since in both cases the application of a small field would cause the FM Fe blocks to align with the applied field. However as the applied field increases, AF coupling between the Fe blocks was observed. The observation of AF coupling is in agreement with the results for tunnel junctions with barrier layers thickness below 12Å [10].

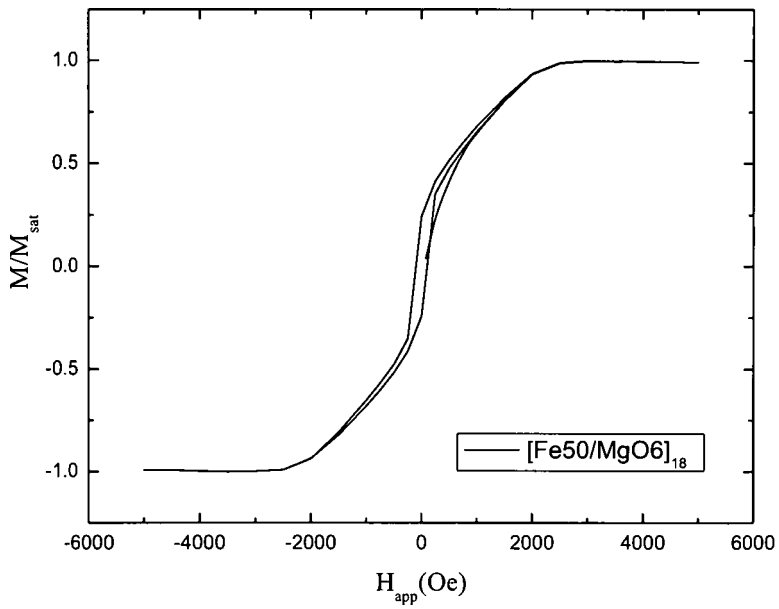

Figure 4.6.2.1: Hysteresis curve for [Fe(50Å)/MgO(6Å)]$_{20}$ at room temperature.

Fe(50Å)/MgO(20Å)]$_{20}$

Figure 4.6.2.2 shows the hysteresis loop for the [Fe(50Å)/MgO(20Å)]$_{20}$ multilayer. The first thing to notice is the magnetic moments follow the applied field very readily, suggesting there is either no coupling between the Fe layers or the Fe blocks are FM coupled. Due to the weak in-plane magnetic anisotropy for magnetic multilayer systems, the FM Fe blocks follow the applied field with very little energy cost. Hence only a small field was needed to saturate the sample.

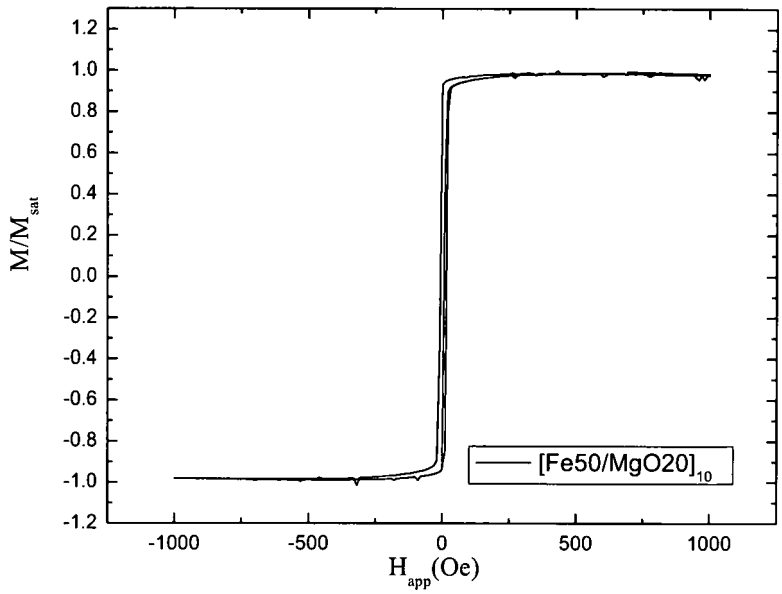

Figure 4.6.2.2: Hysteresis curve for [Fe(50Å)/MgO(20Å)]$_{20}$ at room temperature.

4.7 Polarized neutron reflectivity

4.7.1 Introduction

PNR was performed on these Fe/MgO multilayers. These measurements were designed to enhance the measurements made using the SQUID, since they give microscopic information on the orientation of magnetisation directions of Fe layers. Results from PNR will a provide useful additional information since they determine the precise magnetic structure, rather than only the overall magnetisation information given by SQUID measurements. In particular this technique allows for details of layer-to-layer magnetic correlations to be studied. For instance, using PNR the question of whether the[Fe(50Å)/MgO(20Å)]$_{20}$ sample is FM coupled or uncoupled can be answered. This technique, however, does not probe the specific inter-atomic correlations and is not affected by factors such as mosaic spread. All PNR measurements were performed on the D17 neutron reflectometer with a ^{3}He analyzer.

$Fe(50Å)/MgO(6Å)]_{20}$

Figure 4.7.1.1 shows the polarized neutron reflectivity measurement for sample $[Fe(50Å)/MgO(6Å)]_{20}$ with only a guide field applied along Fe [110]. There are a numbers of interesting features. Firstly, there are no indications of an AF peak at the half wave-vector transfer of the structural peak. Secondly, there is no sign of FM correlations since there is no splitting of the non spin-flip reflectivities R^{++} and R^{--}. Thirdly, there is no correlated component perpendicular to the guide field, because the spin-flip reflectivities R^{+-} and R^{-+} are at background level (Figure 4.7.1.2). It is worth noting that the coherent neutron footprint of the D17 beam along the sample surface is ~100 microns. Now take a ferromagnetic sample and break it up into domains such that the net magnetization is zero. If the domains are much larger than 100 microns, the scattering from them will add incoherently and any neutron polarization information would be lost (no spin-flip scattering). However if the domains are much smaller than the coherent footprint, the neutrons will scatter coherently and spin-flop scattering can be observed. As the domains within this sample are much smaller than 100 microns, therefore one can safely reject the idea that the scattering is due to random ferromagnetic coupled domains. Finally, fits to the data using a single domain model reveal that the reflectivities are purely structural as the random orientated domains resulted in a complete cancelation of the magnetic contribution, and the structural parameters are in good agreement with those determined independently by x-ray techniques. The parameters determined by PNR are listed in Table 4.7.1.1.

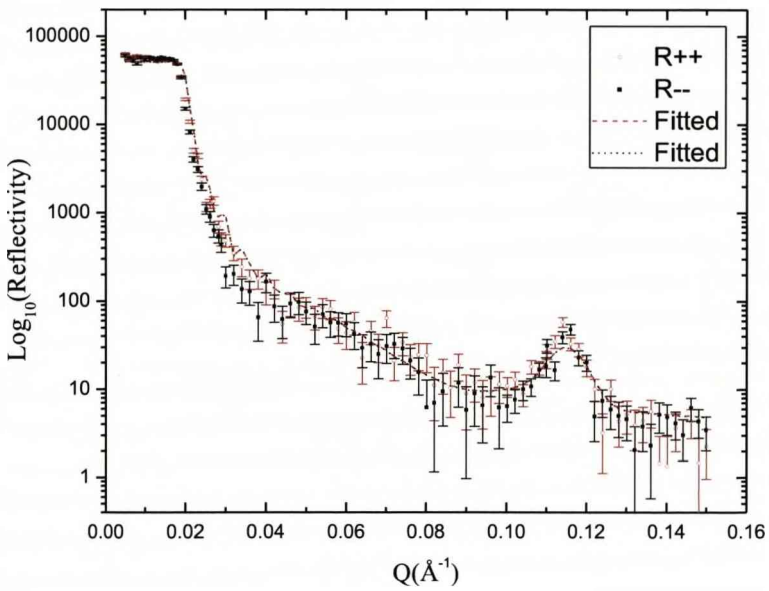

Figure 4.7.1.1: On-specular non-spin flip PNR for $[Fe(50Å)/MgO(6Å)]_{20}$ *at 300K showing no sign of AF or FM coupling.*

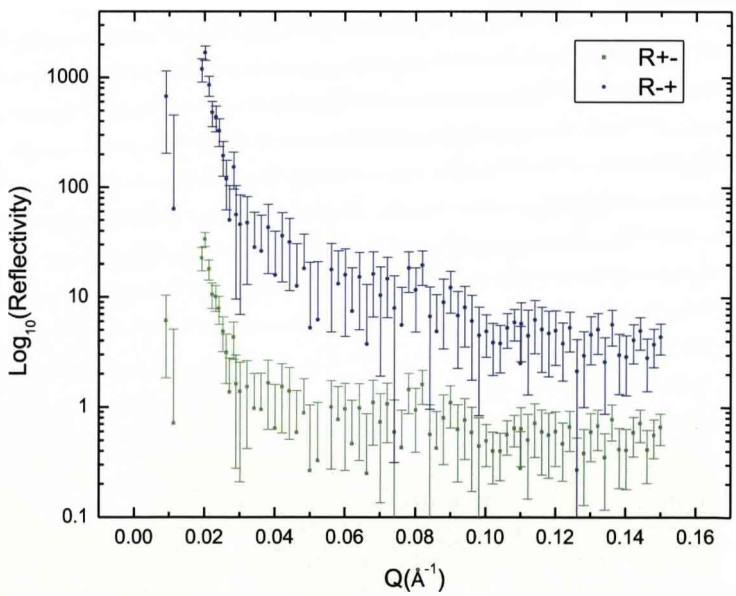

Figure 4.7.1.2: On-specular spin flip PNR for $[Fe(50Å)/MgO(6Å)]_{20}$ *at 300K in guide field, showing no correlations of components perpendicular to the guide field.*

Nominal composition	Fe block thickness ±0.4Å	MgO block thickness ±0.4Å	Magnetic moment $\pm 0.1 \mu_B$	Roughness MgO/Fe ±0.4Å	Roughness Fe/MgO ±0.4Å
$[Fe(50Å)/MgO(6Å)]_{20}$	47.4	7.5	0	7.0	3.8

Table 4.7.1.1: Structural parameters obtained using PNR for the $[Fe(50Å)/MgO(6Å)]_{20}$ superlattice.

A saturation field of 0.32T was applied and the non-spin-flip reflectivities are shown in Figure 4.7.1.2. Once again neither spin-flip reflectivities nor the AF peak at the half wave-vector transfer of the structural peak was observed. However, a clear splitting between R^{++} and R^{--} reflectivities was observed, suggesting that the magnetic moment of Fe blocks are FM aligned along the applied field direction, as expected under a saturation field. The fits to data using the same structural parameters obtained at zero applied field revealed the in-plane ordered Fe moment value to be $1.9 \pm 0.1 \mu_B$ per atom.

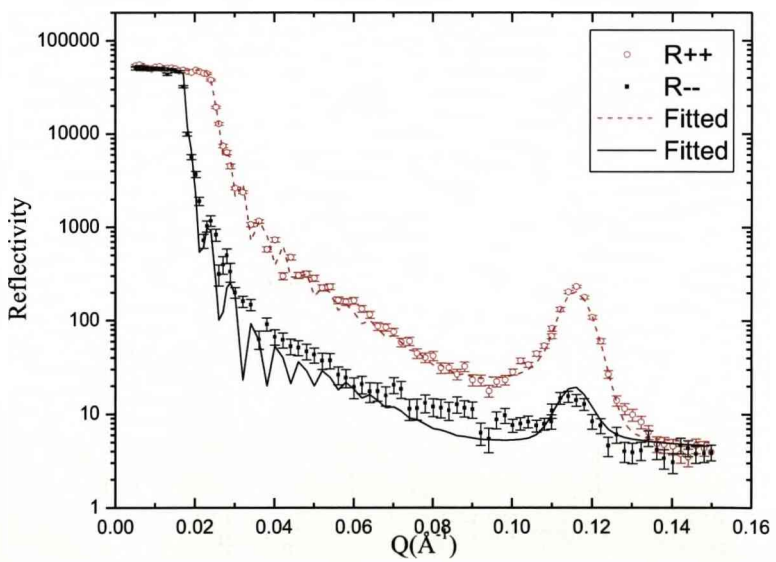

Figure 4.7.1.2: On-specular PNR for $[Fe(50Å)/MgO(6Å)]_{20}$ at 300K in saturation field H=0.32T.

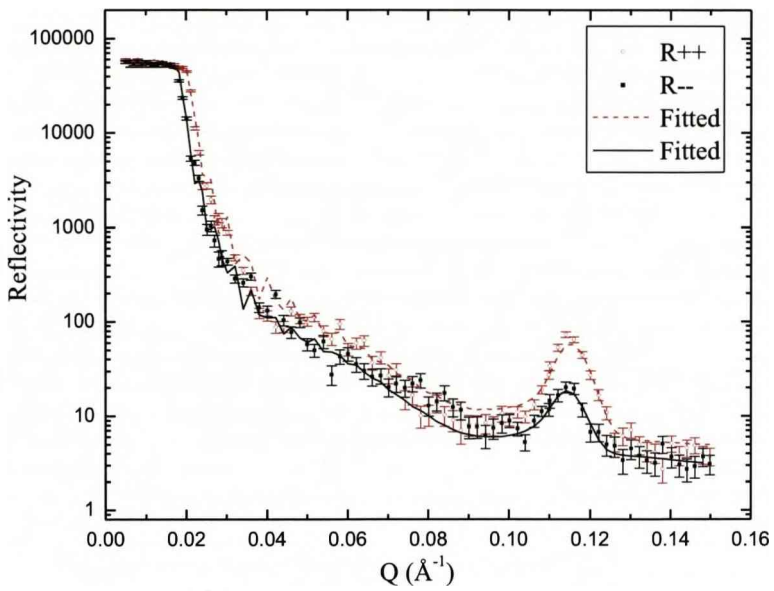

Figure 4.7.1.3: On-specular PNR for [Fe(50Å)/MgO(6Å)]$_{20}$ at 300k with coercive field H=0.0009T.

One cannot easily measure the reflectivity with a field in the opposite direction to the guide field, since depolarization may occur at the point where the field changes sign. Therefore after saturation the sample was then saturated in the opposite direction and thereafter brought back to its magnetic coercive state at 0.009T with the field in the same direction as the guide field. The reflectivities of the coercive state are shown in Figure 4.7.1.3. Surprisingly, splitting between the R^{++} and R^{--} was observed, which indicates that some FM coupling remains. Furthermore no spin-flip reflectivities were observed in this coercive state, again indicating the absence of a correlated component perpendicular to the guide field. Detailed fitting to the data show the Fe moment value is 0.4±0.1 μ_B per atom, which is about 20% of the saturated value. The question arises as to whether the sample contains correlated FM coupled moments, or the sample is FM coupled because the applied field is not at the coercive point due to an offset of the applied field. However if we study the SQUID magnetization data closely, it is easy to see that a field of order 0.025T must be applied to the sample in order to achieve 20% saturation and during the experiment a Hall probe was employed to determine the applied field direction and strength to the nearest 0.0001T and, therefore, an offset of 0.016T is highly unlikely. Hence we conclude that the splitting between the R^{++} and R^{--} is due to the presence of correlated FM moments within the

system and not induced moments due to an offset in the applied field. Comparison of the peak width of the FM Bragg reflection with that obtained in a saturated field indicates that the FM correlation extend through the entire stack in the coercive state.

Fe(50Å)/MgO(20Å)]$_{20}$

We now study the contrasting behaviour of [Fe(50Å)/MgO(20Å)]$_{20}$ Figure 4.7.1.4. shows reflectivities of the sample in its virgin state with 0.001T of guide field applied along Fe [1 1 0] direction. A clear splitting between R++ and R-- was observed indicating FM coupled moments along the guide field direction. Furthermore, spin-flip reflectivities were also detected suggesting the presence of FM coupled moments perpendicular to the guide field. Detailed fitting was performed for all 3 reflectivity channels, and the results show that the Fe moment value is 2.2±0.1 μ_B per atom. The moment components perpendicular to the guide field are comparable to those parallel to the field, and this gives rise to the observation of signal in the R^{+-} and R^{-+} channels. In all cases the coherence of the FM structure is across the whole multilayer stack. Finally the structural fitting parameters are again in good agreement with those obtained independently using the x-ray technique and they are summarized in Table 4.7.1.2.

Nominal composition	Fe block thickness ±0.4Å	MgO block thickness ±0.4Å	Magnetic moment ±0.1μ_b	Roughness MgO/Fe ±0.2Å	Roughness Fe/MgO ±0.2Å
[Fe(50Å)/MgO(6Å)]$_{20}$	49.2	20.7	2.2	6.5	3.4

Table 4.7.1.2: Structural parameters for [Fe(50Å)/MgO(20Å)]$_{20}$ superlattice.

For completeness Figure 4.7.1.5 is included, it shows reflectivity measurements for [Fe(50Å) /MgO(20Å)]$_{20}$ in a saturated field of 0.32T. As expected clear splitting between R++ and R-- providing evidence of FM moment aligned along the guide field direction and spin-flip channel are at background level. As expected under a saturation field Fe moments are aligned along the field direction with Fe moment value of 2.2±0.1 μ_B per atom.

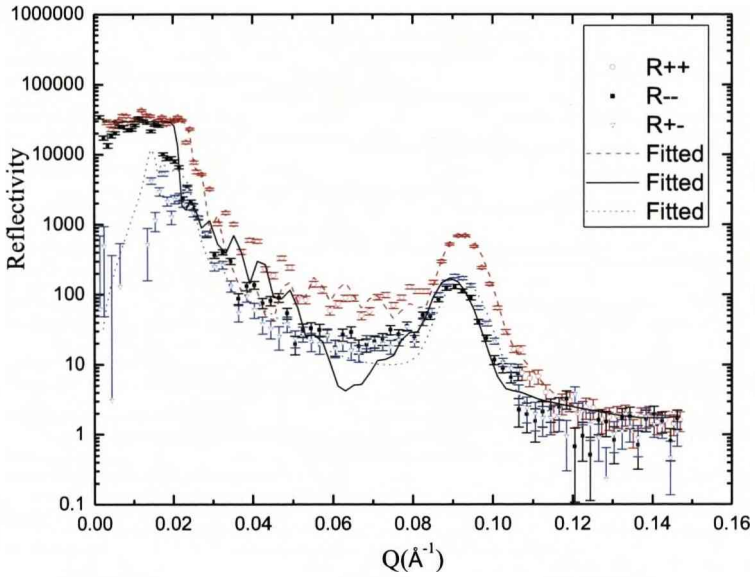

Figure 4.7.1.4: On-specular PNR for [Fe(50Å)/MgO(6Å)]$_{20}$ at 300K in guide field H=0.02T.

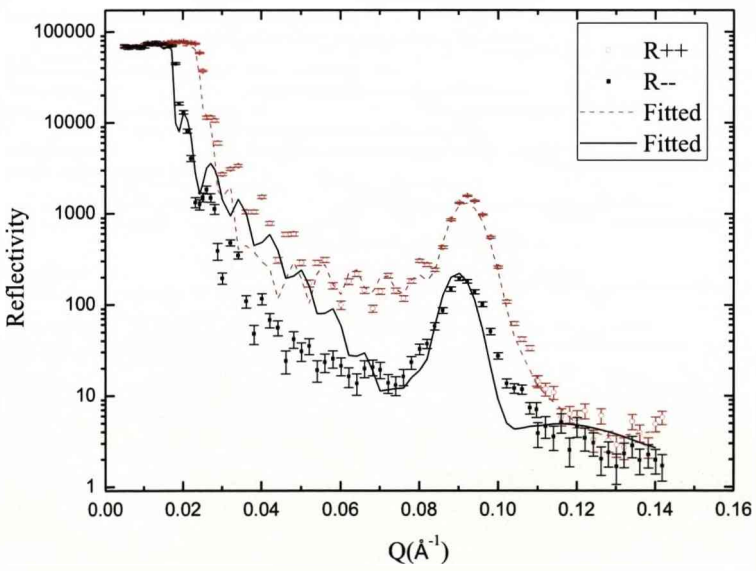

Figure 4.7.1.5: On-specular PNR for [Fe(50Å)/MgO(6Å)]$_{20}$ at 300K in saturated field H=0.32T.

4.8 Discussion

High angle x-ray scattering revealed that the structural coherence of the multilayer is confined within two bilayers. This loss of coherence of the crystal structure can be attributed to the variation in barrier thickness and the large different in lattice parameter between Fe and MgO.

Now I shall discuss the consistency of results between PNR and SQUID measurements for different thicknesses of MgO layer. Then I shall try to understand the magnetic structure of both multilayers. It is important to note that SQUID magnetometry is a technique that can only probe net bulk magnetisations, and only by using PNR, has it been possible to investigate the vector magnetisations of Fe blocks in the Fe/MgO multilayers.

I shall start with the more straight forward case, the multilayer with composition [Fe(50Å)/MgO(20Å)]$_{20}$. SQUID data, suggested that for this thickness of MgO, the Fe blocks are either FM coupled or uncoupled. However, PNR shows that the Fe blocks are FM coupled. Furthermore PNR also demonstrated that this FM structure is coherent throughout the whole structure of the multilayer. Interestingly this FM coupling for MgO thickness greater then 15Å was not expected according to a quantum interference calculation [15]. Therefore, the observed FM coupling is unlikely to be due to quantum interferences within the MgO layers. However, FM coupling could be explained by Néel coupling (orange peel effect). As we saw earlier this chapter, the presence of a wavy correlated roughness can be seen with HREM, and this correlated roughness could lead to orange peal coupling, which in turn gives rise to the FM coupling we observed. For a small field, the Fe moments within a layer do not form a single domain. This idea is supported by the observation of spin-flip reflectivities from the virgin state. This demonstrates that there are some FM coupled layers aligned away from the guide field direction. Figure 4.8.1 summarizes the magnetic structure of [Fe(50Å)/ MgO(20Å)]$_{20}$ at zero applied field, where within each Fe blocks there is the formation of domains, which are FM coupled with successive Fe blocks, but these domain are randomly oriented in zero applied field. When a sufficient high field is applied to this system, these domains will align with the applied field and the system becomes the one-domain structure shown Figure 4.8.2

Now let us consider sample $[Fe(50\text{Å})/MgO(6\text{Å})]_{20}$. From SQUID measurements an AF coupling response was observed between the Fe blocks. However, it was not clear from the SQUID measurements whether there is any kind of FM coupling present within the system. Using PNR in its zero-field state no AF correlations were detected. Furthermore, in its coercive state there are some FM correlations. One possible explanation could be that a randomly varying thickness of the barrier layer arising from the interfacial roughness could lead to successive blocks being AF and FM coupled. Barriers of 6 Å thickness should make successive Fe blocks AF coupled. However, pinholing for thinner barriers or thicker blocks may lead to FM coupling. This would lead to the static magnetic disorder illustrated in Figures 4.8.3 and 4.8.4.

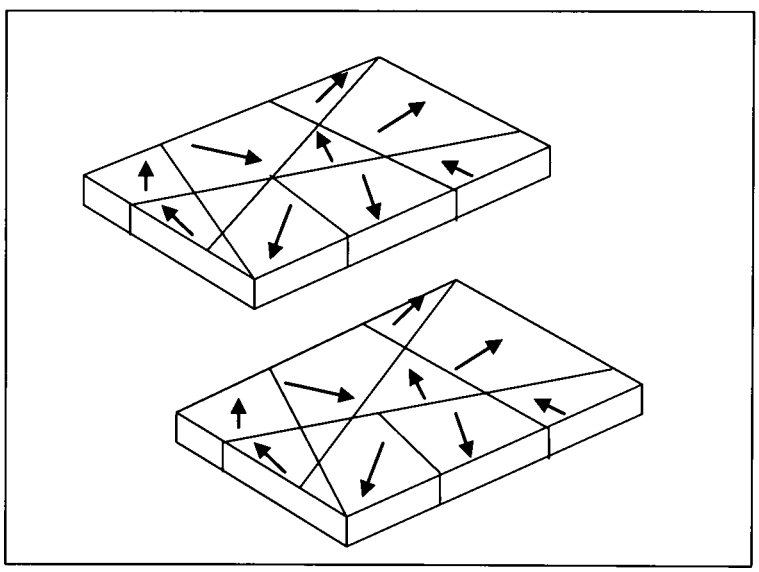

Figure: 4.8.1 Schematic diagram of FM coupled superlattices showing FM coupled domains formations under zero applied field.

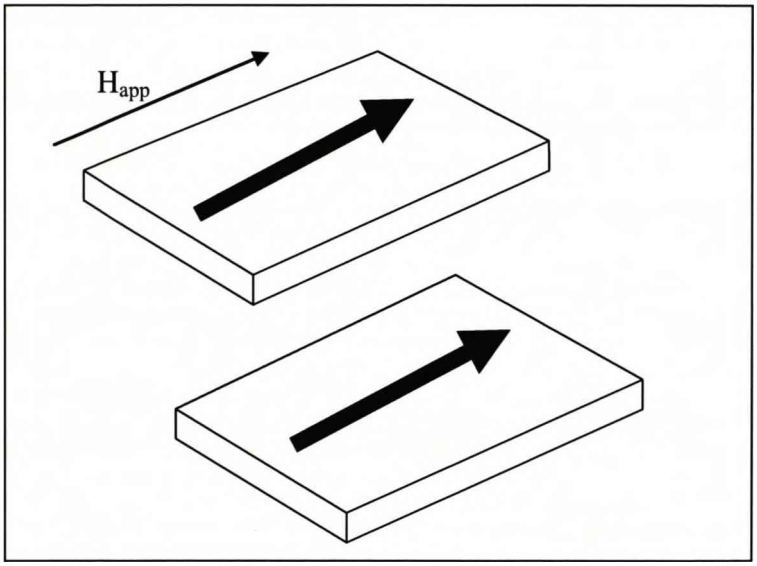

Figure: 4.8.2 Schematic diagram of a FM coupled superlattice under a saturation field.

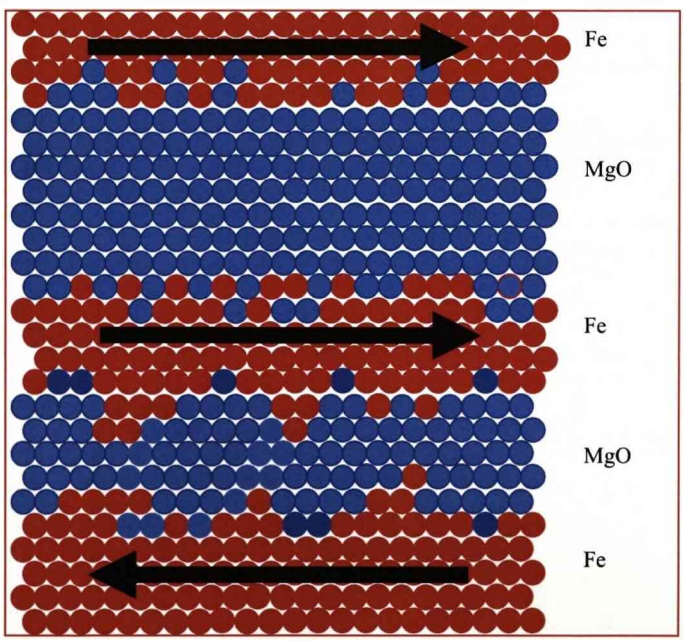

Figure 4.8.3: Illustration of how variation of MgO thickness can result in the coexistence of both FM and AF coupling.

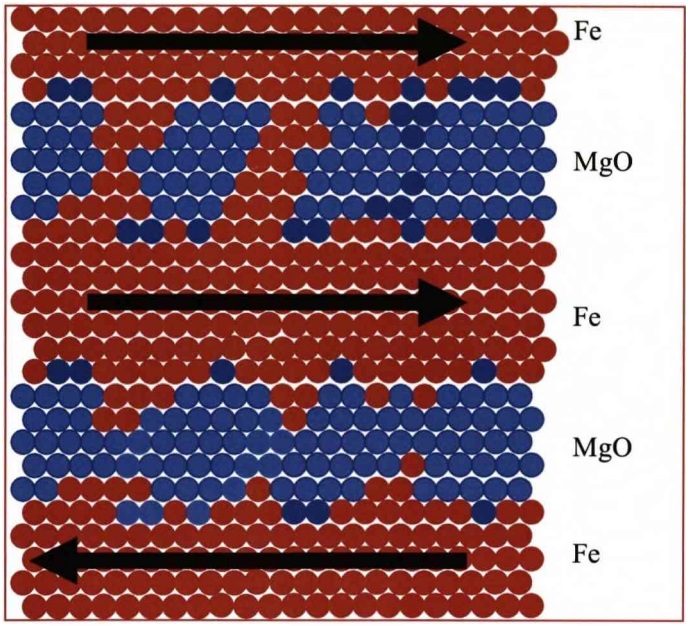

Figure 4.8.4: Illustration how of Fe pinholing can result in the coexistence of both FM and AF coupling.

4.9 Conclusions

By using SQUID, high angle X-ray diffraction, X-ray reflectivity and PNR, we have studied extensively both the crystal structure and magnetic structure of Fe/MgO multilayers. X-ray diffraction and HREM show that the Fe/MgO multilayers have sharp interfaces separating the two components, but the crystalline coherence is confined within 2 bilayers. Furthermore, the presence of wavy roughness leads to substantial variation in the thickness of the barrier layers. We found that for thick MgO layers the system forms a FM coupled structure. In contrast, thin layers of MgO give no magnetic correlation in the virgin state, but do show frozen in FM moments when returned to the coercive state.

These results have implications for the properties of the technologically important Fe/MgO/Fe tunnel junctions. The rather large interfacial roughness will certainly limit the maximum TMR ratio. However, the fact that the Fe and MgO components are sharply separated means that the dramatic affects on TMR arising from oxidation at the interfaces [9] are unlikely to be important for tunnel junctions prepared under these conditions. The presence of FM interactions in both the virgin

and coercive states for thin barrier layers will also limit the practically attainable TMR ratios compared to those possible for junctions with pure AF interactions.

Bibliography

[1] J. S. Moodera, L. R. Kinder, T. M. Wong, and R. Meservey. *Phys. Rev. Lett.* 74, 3273 (1995).

[2] T. Miyazaki and N. Tezuka, *J. Magn. Magn. Mater.* 139, L231 (1995).

[3] S. A. Wolf, D. D. Awschalom, R. A. Buhrman, J. M. Daughton, S. von Molnar, M. L. Roukes, A. Y. Chtchelkanova, and D. M. Treger, *Science* 294, 1488 (2001).

[4] A. Ney, C. Pampuch, R. Koch, and K.H. Ploog, *Nature* 425, 485 (2003).

[5] J. S. Moodera and P. A. LeClaire, *Nature Mater.* 2, 707 (2003).

[6] Yuasa, T. Nagahama, A. Fukushima, Y. Suzuki, and K. Ando, *Nature Mater.* 3, 868 (2004).

[7] S.SP Darkin, *Nature Mater.* 3, 868 (2004).

[8] H. L. Meyerheim, R. Popescu, J. Kirschner, N. Jedrecy, M. Sauvage-Simkin, B. Heinrich, and R. Pinchaux*Phys. Rev. Lett.* 87, 076102 (2001).

[9] C. Heiliger, P. Zahn, B.Y. Yavorsky and I. Mertig, *Phys. Rev. B* 72, 180406(R) (2005).

[10] Hehn, F. Montaigne, and A. Schuhl,, *Phys. Rev. Lett.* 89, 107206 (2002).

[11] E.Popova, C. Tiusan, A. Schuhl, F. Gendron, N. A. Lesnik, *Phys. Rev Lett 74 224415(2006)*

[12] C.Martinez, M. R. Ibarra, A. Cebollada, and F. Briones *J. App. Phys 94 4006 (2003)*

[14] J. C. Slonczewski, *Phys. Rev. B* 39, 6995 (1989).

[15] P. Bruno, *Phys. Rev. B* 52, 411 (1995).

[16] L. Néel, *C. R. Acad. Sci.* 255, 1676 (1962).

[17] SGWang, G.Han, GHYu, Y.Jiang, C.Wang, A.Kohn, and RCCWard, et al, J. Magn. Magn Mater. 310 1935 (2007)

[18] ftp://x2d.phys.cmu.edu/

Chapter 5

Co/Ag nanogranular systems

5.1 Motivation

There is currently intense interest in the behaviour of magnetic nanoparticles due to the huge potential for commercial exploitation in diverse areas, such as data storage, sensors and drug delivery systems. Many of these applications rely on the phenomenon of giant magnetoresistance (GMR). The GMR effect arises from spin-dependent electron scattering [1,2], which gives a reduction in the resistivity when the magnetic nanoparticles are aligned. GMR was discovered in nanogranular alloys independently in 1992 by Berkowitz *et al.* [3] and Xiao *et al.* [4]. Later a similar GMR effect was reported for various granular systems and the strongest effect was observed for the Co/Ag system [5-12]. Recently, a record 40% room temperature GMR was observed in a nanogranular Co/Ag alloy by optimizing the concentration, sputtering conditions and heat treatment [13].

The motivation behind the studies of the Co/Ag nanogranular system is to obtain information about the magnetic structure of the embedded particles and use that to gain an understanding of the complex changes in GMR ratio as a function of annealing temperature.

5.2 Introduction

The GMR measurements that have inspired the work in this chapter were performed by Jose De Toro at the Universidad Castilla-La Mancha. A VSM magnetometer was used to provide the required field (15kOe) for magneto resistance

measurements, and a standard four-probe method was then employed to measure the change in resistance with and without applied field for samples after different heat treatments.

Figure 5.2.1 shows the observed magnetoresistance as a function of annealing temperature. Before any heat treatment the GMR ratio is 27%, and it remains at this level for annealing temperatures up to 200°C. As the annealing temperature increases further towards 230°C a small reduction in GMR ratio was observed. Continued annealing of the sample up to 300°C resulted in the observation of the record high 38% GMR. Annealing to still higher temperatures caused a reduction of the GMR, and annealing at 420 °C brought the GMR ratio back to 25%.

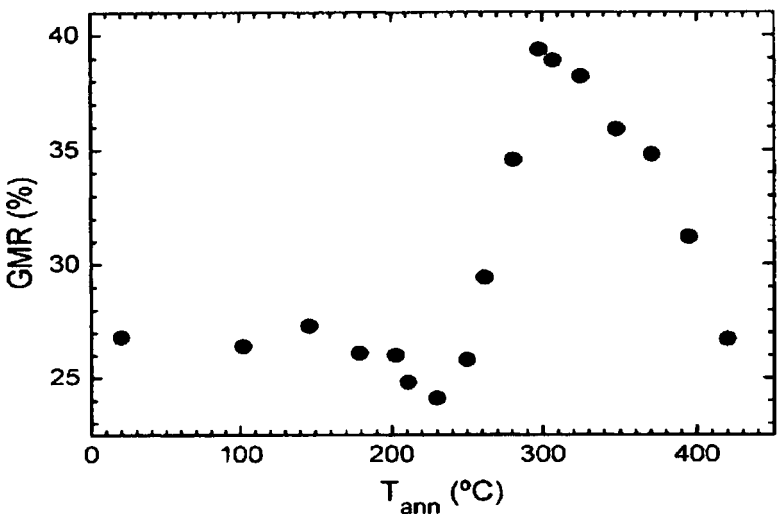

Figure 5.2.1 GMR ratio as a function of annealing temperature for the $Co_{29}Ag_{71}$ nanogranular sample [13].

In this chapter, after describing the sample growth conditions and experimental techniques, I shall present detailed studies of the structural and magnetic ordering of the Co/Ag nanogranular system. First, I shall describe high-angle x-ray diffraction studies, which yield information on the crystal structure and lattice parameters for both Co and Ag. Then I shall present SANS data to determine how the magnetic structure evolves during the heat treatment. Finally, I shall show how the model used to describe the x-ray diffraction and SANS data provides a comprehensive understanding of the complex dependence of GMR ratio on annealing temperature shown in Figure 5.2.1.

5.3 Sample growth

Nanogranular alloys of composition $Co_{29}Ag_{71}$ were prepared by Jose De Toro using rf magnetron sputtering at the Universidad Castilla-La Mancha. A composite cathode consisting of high purity (≈99.9%) small pieces of Co symmetrically arranged on an Ag target. Films of thickness of 8 μm were grown on glass substrates at room temperature with a deposition rate of 1.1nm/s. The residual pressure was $4x10^{-7}$ mbar and the Ar pressure during deposition was $3x10^{-3}$ mbar. A 30 watt power was employed during growth to optimize GMR effect.

5.4 Experimental procedure

High angle x-ray diffraction experiments were performed using the XMaS beamline at the ESRF, with an incident x-ray energy of 6.6keV. Further studies were performed using the in-house Philips X-Pert diffractometer with Cu Kα radiation at incident energy of 8.048keV. Further bulk magnetic properties were measured using a SQUID magnetometer at the University of Liverpool and the microscopic magnetic structure was studied by SANS using D11 at the ILL and LOQ at ISIS, see chapter 3 for further details on these techniques. The small volume of magnetic material meant that it was necessary to form a coupon of samples to increase the signal. Furthermore, the films were peeled away from the glass substrates to reduce background. The stack of Co/Ag film was fixed together by using two pieces of silicone with an open area of $18x4mm^2$. The thermal treatment of the sample was performed using a tube oven at the ILL during the SANS experiment.

5.5 High-angle x-ray diffraction

The inset in Figure 5.5.1 shows the high-angle x-ray diffraction from the Co/Ag nanogranular system. Both the Co and Ag adopt the FCC structure with the FCC [111] direction preferentially perpendicular to the surface. The mosic spreads for Co and Ag before annealing are 23° and 18°, respectively. After annealing the mosaic spreads reduce to 7.2° for Ag and 7.7° for Co. This suggests that the annealing process helps both Co and Ag crystal grains to align with their (111) planes parallel to the surface.

Figure 5.5.1 also shows the change of the Co and Ag lattice parameters as a function of annealing temperature. The two lattice constants are calculated using the scattering angles, 2θ, of the Co and Ag x-ray diffraction peaks. It was observed that as the annealing temperature increases the Ag peaks move to a lower 2θ values suggesting there is an increase of the Ag lattice parameter. In contrast the Co diffraction peaks shifted to higher 2θ values and, therefore, the Co lattice parameter increases as a function of annealing temperature. As the annealing temperature increases the Ag and Co lattice parameters approach their bulk values, confirming the assignment of these peaks. It is clear from the data that the Co- and Ag-rich regions undergo phase separation when the annealing temperature goes above 200°C, where the lattice parameters are first observed to change. As the annealing temperature increases above 400°C the lattice parameters for both Co and Ag are very close to their bulk values.

Finally it is worth examining the structural coherence in the growth direction, which can be estimated using equation (3.1.2.12). Before any annealing the coherence length is 22nm for Ag and 3.9nm for Co. These values give an estimate of grain sizes in the matrix and the size of the nanoparticles, respectively. After annealing at 420°C these coherence lengths increases to 27nm and 7.6nm for Ag and Co, respectively. The increase in grain size in the matrix would be expected after annealing, but the large increase in nanoparticle size is more unusual. In fact, the results strongly suggest that the nanoparticles are agglomerating to form much larger particles.

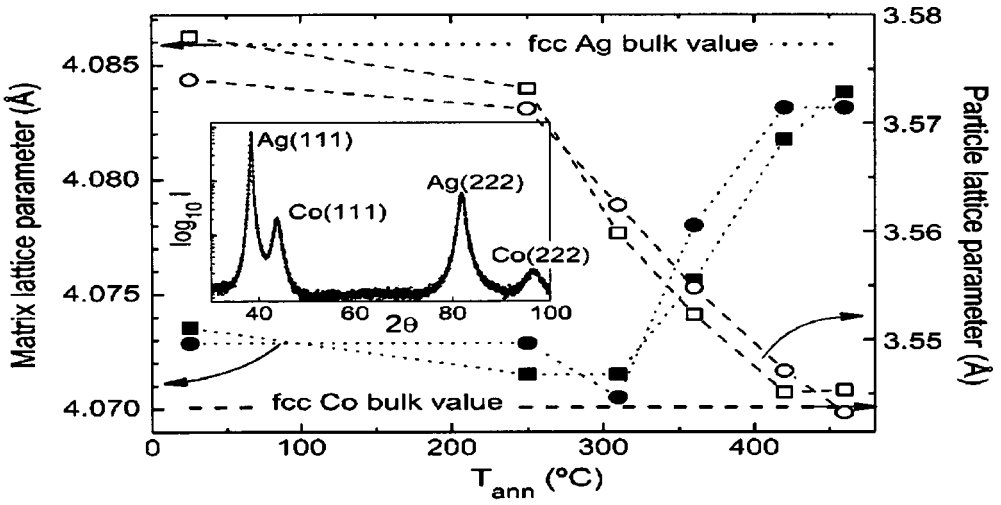

Figure 5.5.1: Changes in Co and Ag lattice parameters as a function of annealing temperature, the inset is a typical plot showing the high-angle x-ray diffraction.

5.6 Small angle neutron scattering (SANS)

SANS measurements were performed on Co/Ag nanogranular samples for different annealing temperatures. In this section I shall begin with an overview of the two dimensional data. This will be followed by analysis of the reduced one dimensional data set, using the methods discussed in chapter 3.

2d SANS

The SANS data was corrected for transmission, background and detector efficiency using a program called Grasp [14]. Figure 5.6.1 shows the scattering patterns from Co/Ag samples after different heat treatments with a 1T field parallel to the plane of the film and perpendicular to the incident beam.

The qualitative nature of the scattering changes very little from the non-annealed to annealing temperatures up to 300°C. However, as the annealing temperature increases toward 420°C a noticeable change in the scattering pattern can be observed. This change in the scattering pattern can be attributed to the change in the scattering length density of the Co particles and its surrounding matrix. This will be discussed in more detail later in this chapter.

A very interesting feature was observed when the detector was placed at a larger distance, 4m, from the sample, i.e. at lower Q. Extra scattering intensity was observed *parallel* to the field direction, see Figure 5.6.2. This was observed for all samples with annealing temperatures up to 300°C. However, the effect disappears for the sample annealed at 420°C. The scattering parallel to the applied field is believed to originate from the spin-misalignment [15] between the magnetic particle and the magnetic matrix and this is commonly observed for magnetic alloy systems like Co/Ag [16,17]. The disappearance of this scattering after annealing at 420°C is due to the removal of the cobalt impurities within the silver matrix. This results in a decrease in the magnetic scattering length density of the matrix, and in turn reduces the effect of spin-misalignment scattering. This result is in good agreement with the high-angle x-ray diffraction data, where the cobalt and silver undergo phase separation at high annealing temperatures.

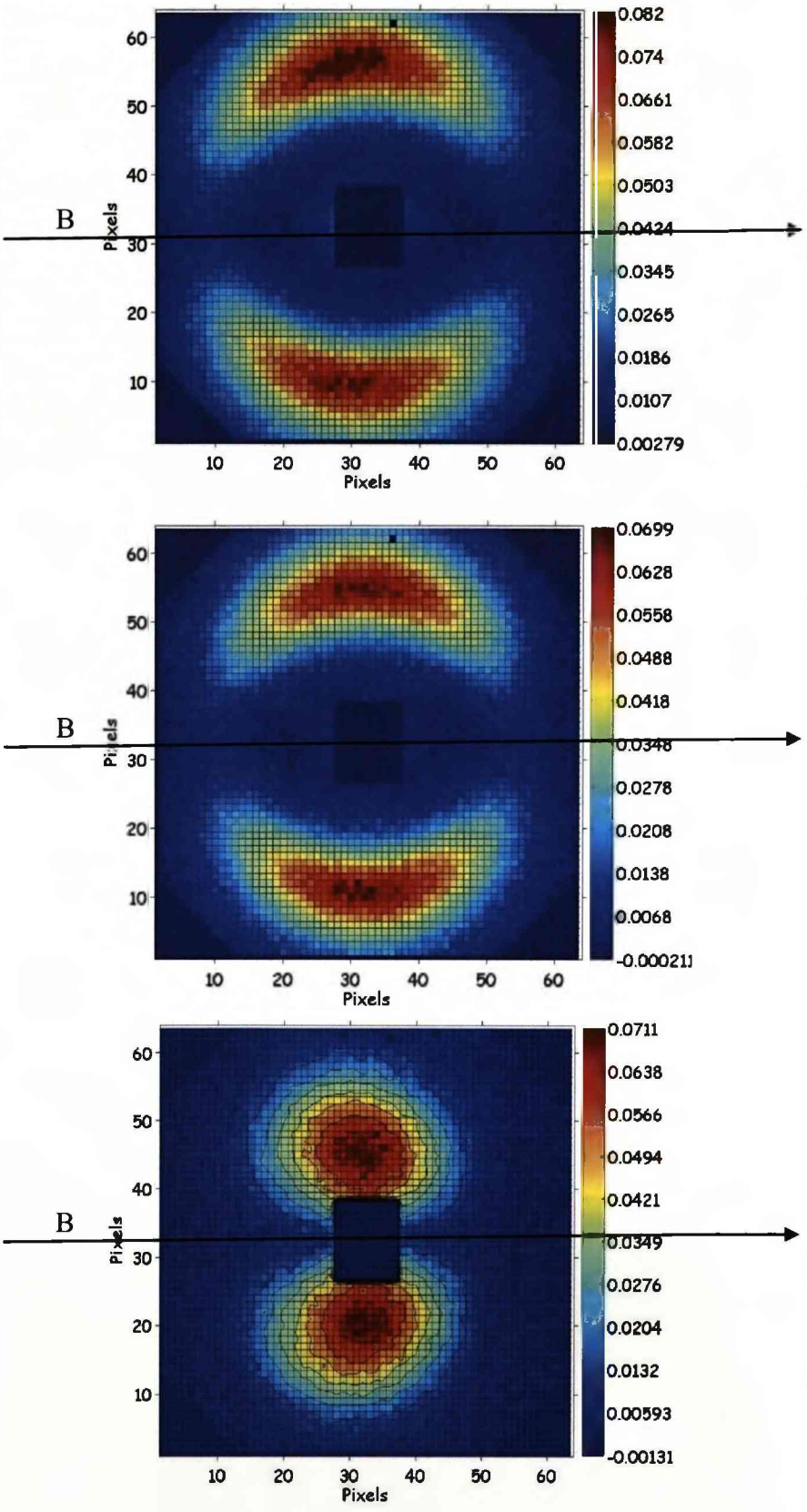

Figure.5.6.1: 2D scattering patterns from Co/Ag nanogranular system with detector positioned at 1.2m and 1T applied field after different annealing temperatures: (top) as deposited; (middle) annealed at 300°C; (bottom) annealed at 420°C.

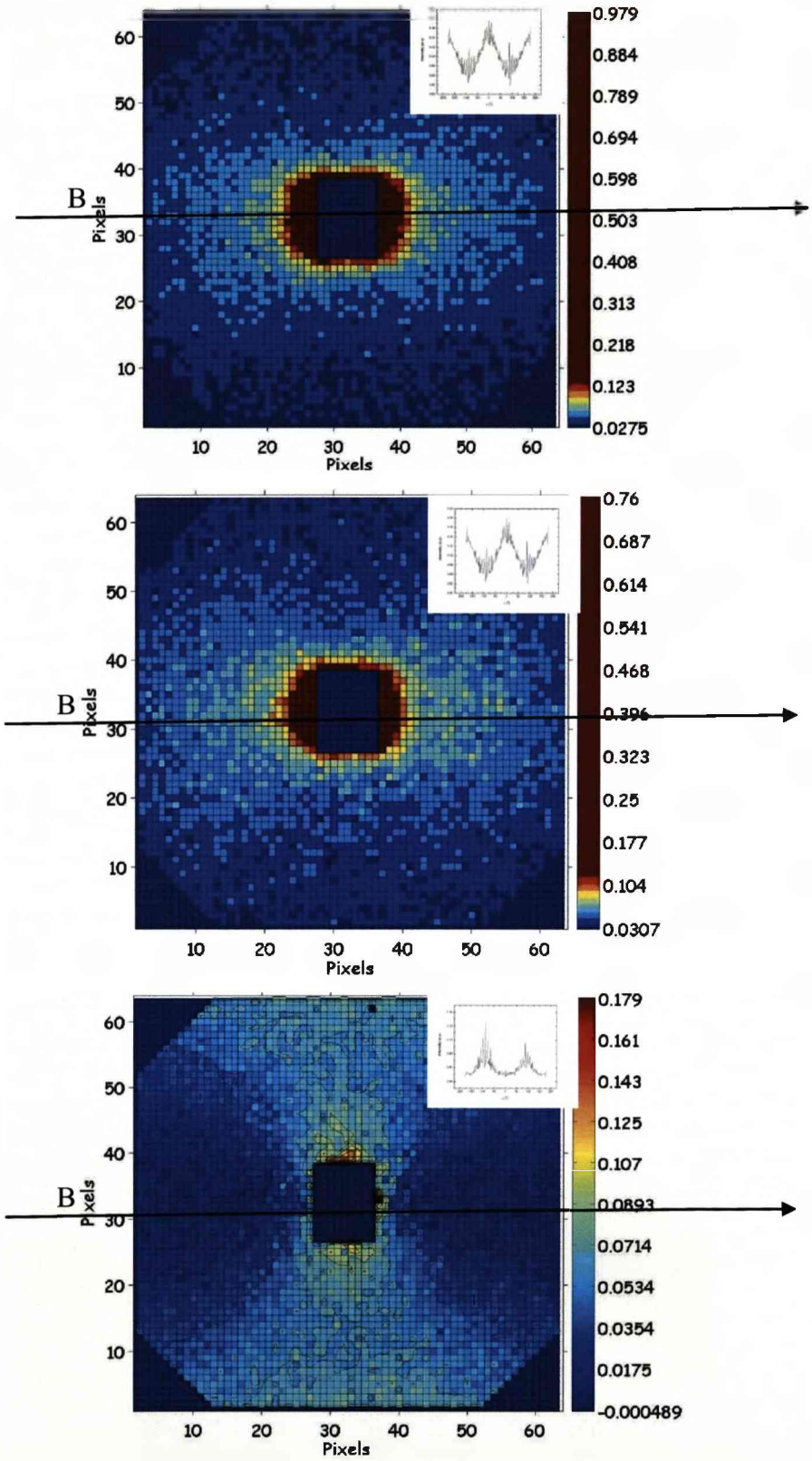

Figure 5.6.2: 2D scattering patterns from Co/Ag samples under a 1T field and with the detector at 4m: (top) as deposited; (middle) annealed at 300°C; (bottom) annealed at 420°C. Inserts show intensity as a function of α.

1d SANS

The Grasp software was also used to reduce the 2d data with applied field into more manageable 1d data sets by fitting

$$I = A(Q) + B(Q)\sin^2(\alpha+\varphi) \qquad (5.6.1)$$

to the 2d data at constant Q, which allow A(Q) and B(Q) to be separated. Where $B(Q)$ gives the magnetic scattering amplitude, $A(Q)$ gives the nuclear scattering amplitude and the value of φ indicates the offset in the magnetic moment direction. Figure 5.6.3 shows θ for the three different annealing temperatures. φ shifts at Q=0.12Å^{-1} from φ=0° to 90° for the two samples with annealing temperatures below 420°C. This suggests that there is a change in magnetic scattering length density contrast parallel to the applied field direction. However as the sample was annealed further, up to 420°C, the transition to 90° disappeared, which implies that the magnetic scattering length contrast parallel to the applied field vanishes as the sample is annealed at 420°C. When φ=90° there is substantial spin-misalignment scattering, when φ=0° there is not. Due to the difficulty in handling the spin-misalignment scattering, in the subsequent data analysis I shall only include measurements where φ=0°.

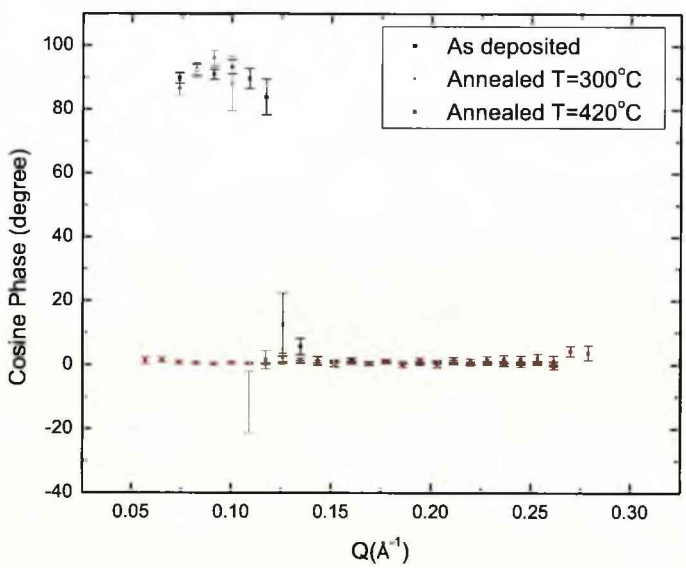

Figure 5.6.3: Variation in φ as a function of Q for different annealing temperatures.

Attempts to fit the scattering using simple single-particle and core-shell models were unsuccessful. Figure 5.6.4 compares the data from the sample annealed at 300 °C with single-particle and core-shell simulations. Single-particle models fail to generate the peak width observed in the experimental data. Furthermore, the size of the particle obtained using this model is a radius of 3.1nm, and this is more than twice the size estimated by magnetization measurements. In contrast the plot for the core-shell model shows very good agreement with the data and produces parameters in good agreement with the size estimated by magnetization. However diffusion-zone model is used over the core-shell model for the simple reason that a less sharp diffused interface is a more realistic model to describe this nanogranular/alloy system [18], and for these reasons the single-particle and core-shell models were rejected.

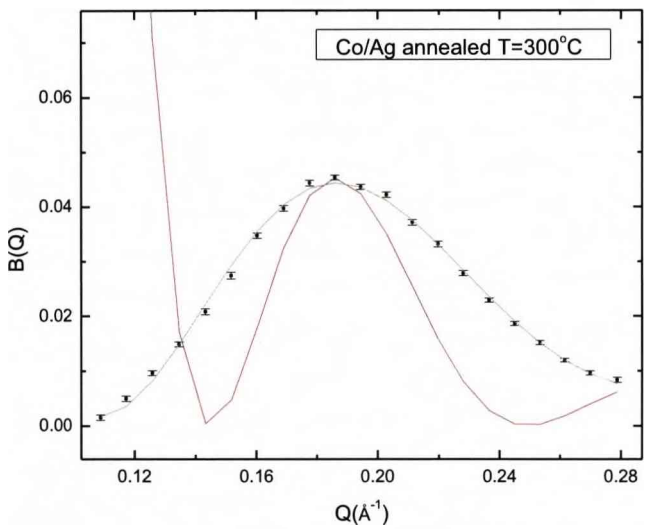

Figure 5.6.4: The data points show the reduced 1d magnetic scattering from the sample annealed at 300 °C by fitting the 2d data using equation . The red and green lines are the calculated scattering intensity using single-particle and core-shell models, respectively.

Figure 5.6.5 shows the magnetic scattering intensity from the sample after different heat treatments. Up to annealing temperatures of 300°C the changes to the scattering are subtle, with the peak moving slowly to lower Q. However, there is a dramatic change for the sample annealed at 420°C, with a large shift of the peak to lower Q and substantial broadening.

The lines through the data points are least square fits obtained using the polydisperse diffusion-zone particle model [18] described in section 3.1.4. Detailed modelling of the data suggests that the Co particles are imbedded in a magnetic matrix. This matrix is formed due to the large amount of Co impurities within the Ag matrix after growth and before any annealing. The variation of the magnetic scattering length density as a function of distance from the core centre within this system for different annealing temperatures is shown in Figure 5.6.6. The fitted parameters are summarised in Table 5.6.1.

The average particle size increases with annealing temperature, from 1.4±0.1 nm in radius for the as-prepared sample to 1.62±0.1 nm when the annealing temperature reaches 420°C. The heat treatment also causes the diffusion zone to reduce in size, from 0.52±0.1 nm down to 0.42±0.1nm. As well as changes in the particle size, the particles become more polydisperse. The size distribution was modelled using a lognormal distribution and it was found that the sigma of the distribution increases from 0.07 for the as prepared sample to 0.18 for the sample annealed at 420°C. Furthermore, as the annealing temperature was increased the magnetic scattering length density of the matrix was found to decrease, whereas the magnetic scattering length density of the particles increased. This is due to the Co atoms leaving the Ag matrix to join up with the Co particles (phase separation). The changes in magnetic scattering length density (MSLD) are plotted as a function of annealing temperature in figure 5.6.7. The MSLD of the diffusion zone was held fixed for all three temperatures. Although the MSLD of the diffusion zone can be allowed to vary or set at any level below the MSLD of the matrix and core. However, changing the MSLD of the diffusion zone only causes the MSLD of both the core and matrix to adjust so that the MSLD as a function of radius looks essentially the same, as shown in figure 5.6.7.

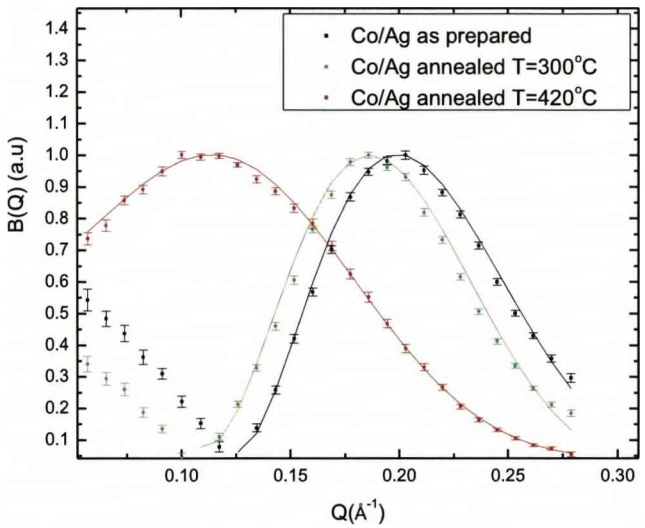

Figure 5.6.5: 1d magnetic scattering intensity for Co/Ag nanoparticles system with 1T applied field after different annealing temperatures, lines through data are fits using a polydisperse diffusion-zone particle model.

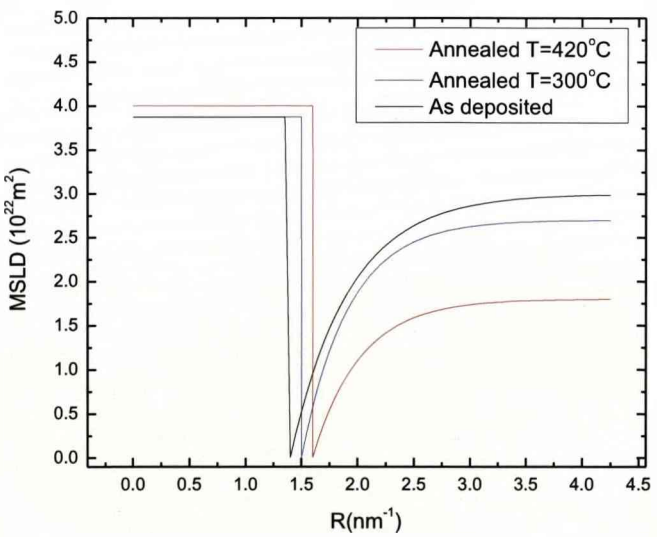

Figure 5.6.6: The MSLD as a function of distance from the centre of the core for different annealing temperatures.

Annealing temperature °C	Particle radius ± 0.1nm	Diffusion zone ± 0.1nm	MSLD particle ± 0.1 $(\times 10^{14})m^{-2}$	MSLD diffusion zone $(\times 10^{14})m^{2}$	MSLD matrix ± 0.1 $(\times 10^{14})m^{2}$	Sigma ± 0.02
As prepared	1.40	0.52	3.7	0.0	2.9	0.07
300	1.52	0.44	3.8	0.0	2.7	0.08
420	1.62	0.42	4.0	0.0	1.8	0.16

Table 5.6.1: Summary of all the fitted parameters for different annealing temperatures. The MSLD of the diffusion zone was fixed at zero for all three annealing temperatures.

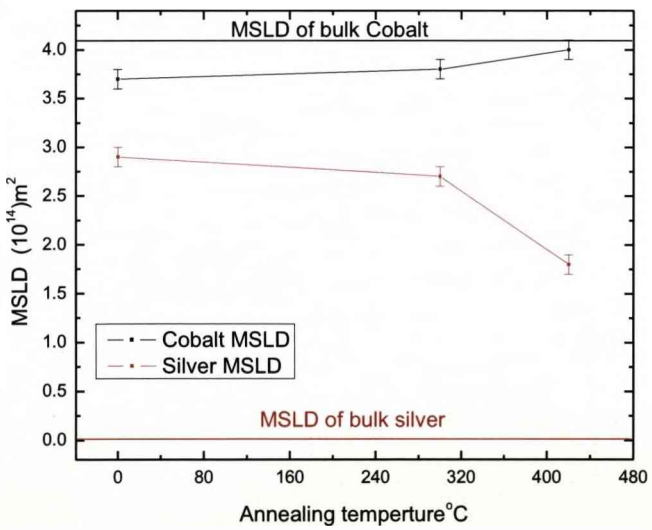

Figure 5.6.7: MSLD as a function of annealing temperature, red and black lines are for Ag and Co, respectively.

Figure 5.6.8 shows the 2d SANS data with no applied field for the three different annealing temperatures. The magnetization data indicate that the samples are paramagnetic at room temperature. Since the magnetic moments are randomly oriented. Thus, the scatting patterns in fig 5.6.8 are completely symmetrical.

Figure 5.6.9 shows the one-dimensional data obtained by taking the circular average at constant Q. The solid lines in this figure show fits of the same polydisperse diffusion-zone particle model used to model the magnetic scattering. Both the average particle radius and the diffusion zone size were fixed at the values obtained using the magnetic scattering and the fits are in excellent agreement with the structural scattering in figure 5.6.9. Figure 5.6.10 shows the structural scattering length density (SLD) as a function of distance from the core, and Table 5.6.2 summarizes the fitted parameters.

One can see that the changes in scattering length density (SLD) are similar to the magnetic case. Without any heat treatment the particles and the matrix consist of a mixture of both Co *and* Ag with a diffusion zone in between containing mainly Ag. In contrast to the magnetic case where the Co has the highest SLD, in the structural case Co has the lowest value of SLD. Despite the very different scattering contrasts, this model reproduces the data for both magnetic and structural scattering. As the sample is annealed at increasingly higher temperatures the SLD of the matrix increases from $2.54\times10^{14}\,\mathrm{m}^2$ towards the bulk Ag value, $3.31\times10^{14}\,\mathrm{m}^2$. at the same time the SLD of the core decreases from $2.48\times10^{14}\,\mathrm{m}^2$ towards the bulk value of Co. The SLD of the diffusion zone was fixed at the bulk Ag value. Figure 5.6.11 shows the changes in the SLD as a function of temperature, the SLD of the core decreases towards the bulk value of Co, at the same time the SLD of the matrix increases to the Ag bulk value.

In summary, SANS measurements revealed that the Co/Ag systems consist of a magnetic particle core with a small, less-magnetic diffusion zone imbedded in a magnetic matrix. Before any heat treatment there are contaminations of Ag atoms within the Co particles, and Co atoms within the Ag matrix. As the sample is annealed phase separation occurs so that the Co atoms within the Ag matrix leave the Ag to join up with the Co particles to form bigger particles. At the same time the Ag atoms inside the Co particles are able to diffuse and combine with the silver in the matrix. The result of this separation is that the Co particle size increases and the MSLD increases at the expense of the matrix. Furthermore the increase in the sigma of the

size distribution is to be expected since, as well as phase separation, the agglomeration of particles determined using x-ray diffraction will increase the range of particle sizes. The small increase in average particle size found using SANS and the large increase obtained using x-ray diffraction are consistent since the crude average of the latter overestimates the contribution of the largest particles, since they have the largest scattering power. Finally, the approach to bulk lattice parameters for high annealing temperatures, the reduction in the MSLD in the matrix and the disappearance of the spin-misalignment scattering are all consistent with the proposed phase separation.

Annealing temperature °C	Particle radius	Diffusion zone	SLD particle ± 0.1 $(\times 10^{14})m^2$	SLD diffusion zone	SLD matrix ± 0.1 $(\times 10^{14})m^2$	Sigma ± 0.05
As prepared	1.40	0.34	2.48	3.31	2.54	0.39
300	1.52	0.44	2.43	3.31	2.67	0.39
420	1.62	0.42	2.32	3.31	2.90	0.39

Table 5.6.2: Summary of the structural fitting parameters for different annealing temperatures.

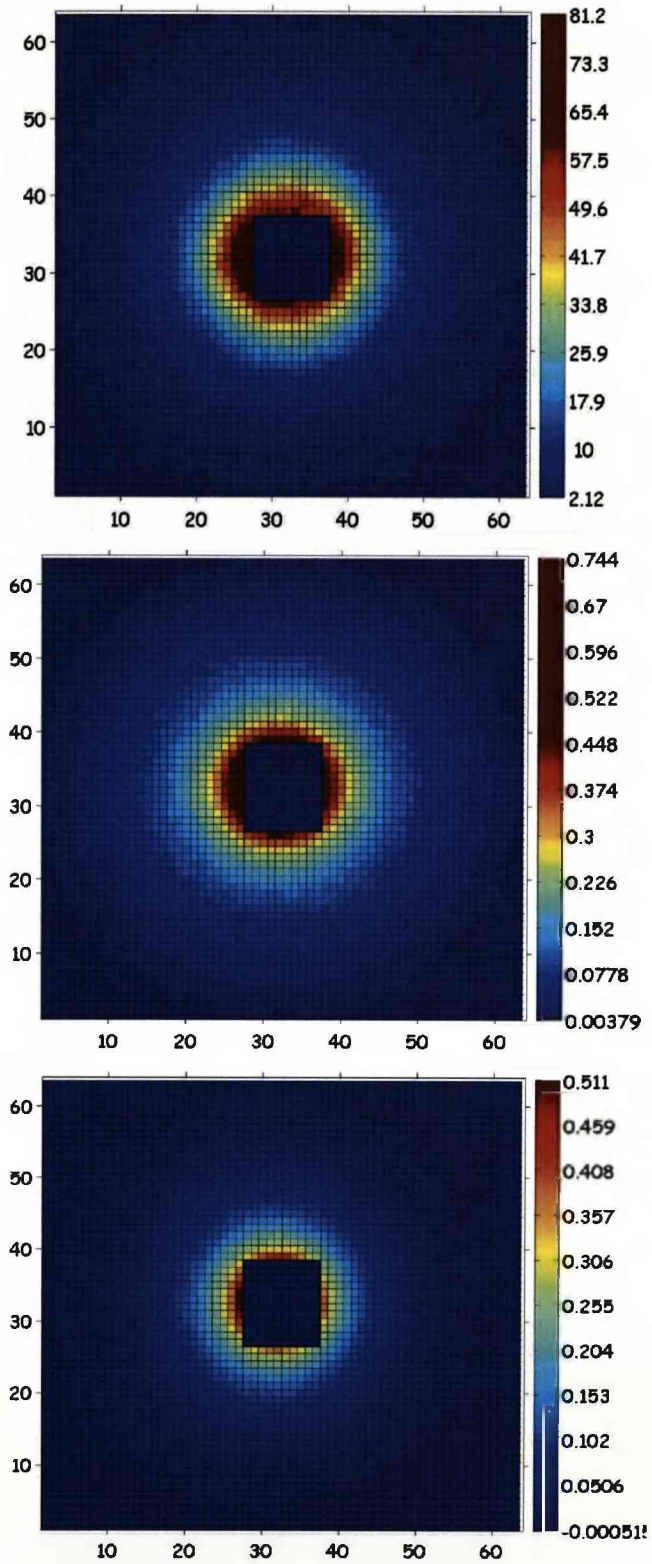

Figure 5.6.8: 2D scattering patterns from Co/Ag with no applied field after different annealing treatments: (top) as deposited; (middle) annealed at 300°C; (bottom) annealed at 420°C.

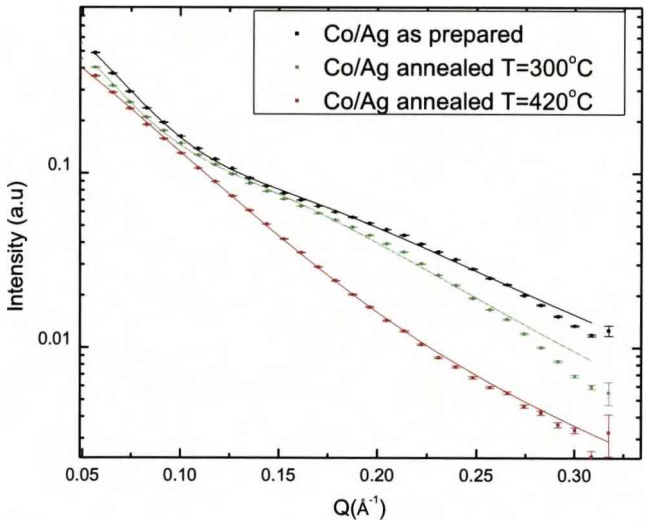

Figure 5.6.9: Structural scattering intensity for Co/Ag nanoparticles systems after different annealing treatments, lines through data points are fits using the polydisperse diffusion-zone particle model.

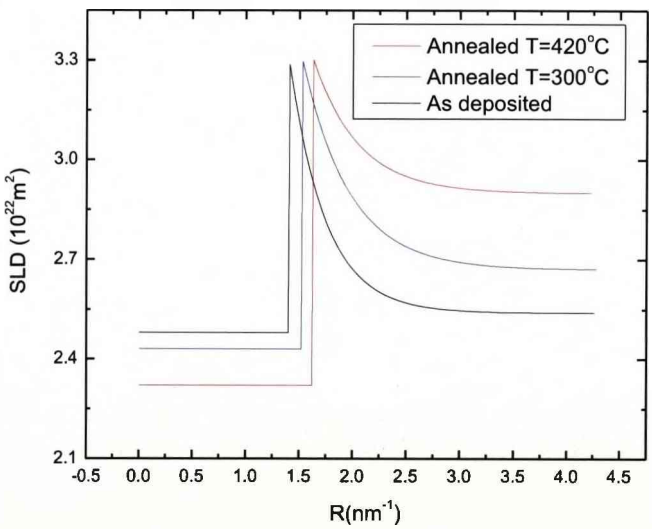

Figure 5.6.10: The SLD as a function of distance from the centre of the core for different annealing temperatures

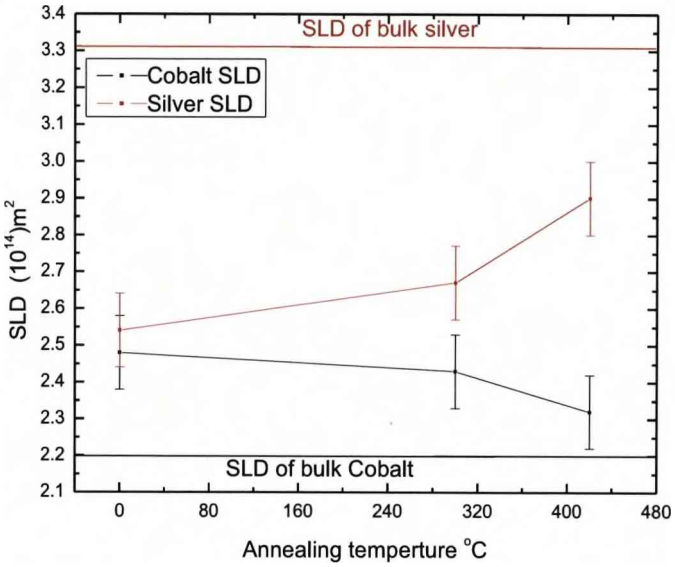

Figure 5.6.11: Structural scattering length density as a function of annealing temperature, red and black lines are for Ag and Co, respectively.

5.7 Discussion

In this section I shall try to provide an explanation for the complex behaviour of the GMR ratio as a function of annealing temperature on the basis of the SANS and x-ray diffraction results. However, there is a complication since the large amount of sample required for SANS measurements meant that a new batch of samples were grown and these were annealed during the SANS experiment. [In contrast, the x-ray diffraction measurements were performed on the original samples.] As a result I have preformed magnetisation measurements on the new batch of samples in order to establish the relationship between these newly annealed samples to those used in the GMR measurements. Figure 5.7.1 shows the hysteresis loops for a sample for which the maximum GMR ratio was observed previously and the sample annealed to 420°C for SANS measurements. The fits of the Langevin function revealed that the effective particle magnetic moments for the two samples are similar, 7600±100 μ_b and 7200±100 μ_b for the SANS sample annealed at 420 °C and the maximum GMR

sample, respectively. Furthermore field-cool and zero-field-cool measurements show the two samples have a similar blocking temperature of about 160K, see figure 5.7.2. In addition, figure 5.7.3 shows FC and ZFC measurements for the GMR sample annealed at 420°C. It shows a blocking temperature of about 300K, which is well above the 160K observed for the new batch of SANS sample annealed at 420°C. Therefore, these control magnetization measurements suggest that the annealed 420°C sample used in SANS experiment are in a very similar state to the maximum GMR sample so, for the purpose of the discussion here, I shall refer to both of them as the "maximum GMR sample".

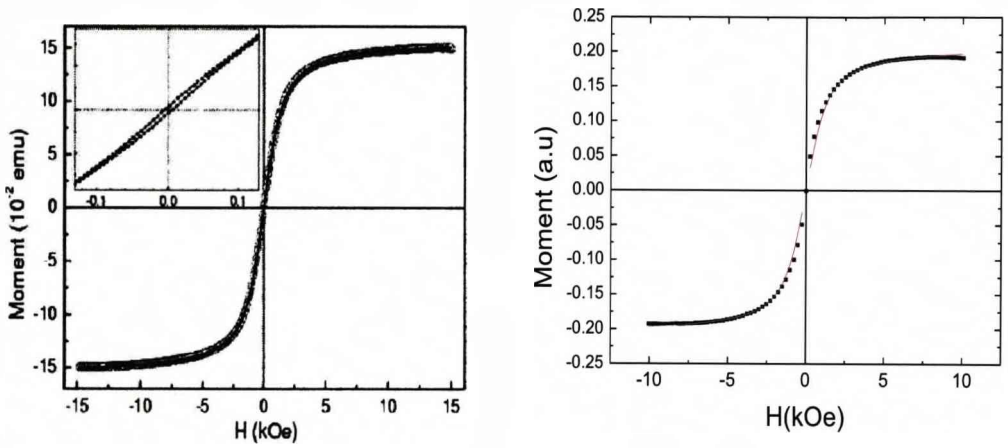

Figure 5.7.1: (Left) hysteresis loop for the maximum GMR sample and (right) hysteresis loop for sample annealed at 420°C during the SANS measurements.

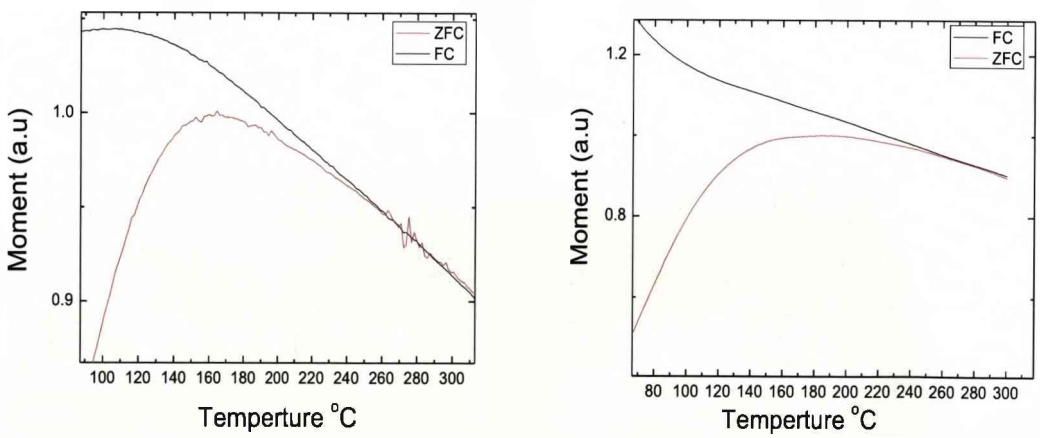

Figure 5.7.2: (Left) field- and zero- field-cool measurements for the maximum GMR sample and (right) field and zero field cool measurements for sample annealed at 420°C.

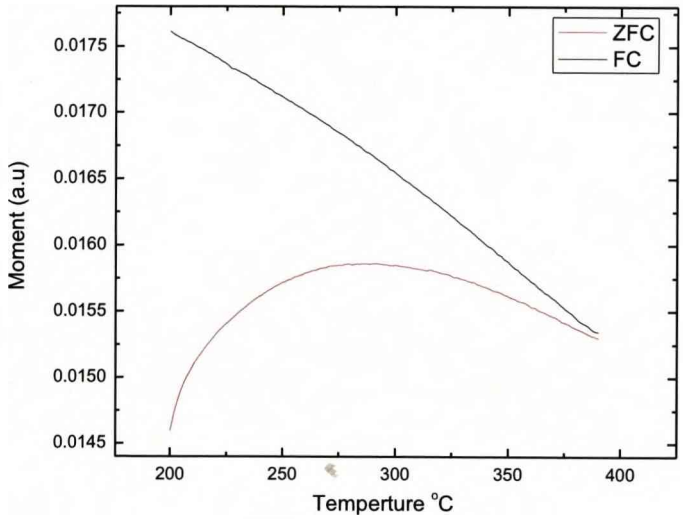

Figure 5.7.3: Field- and zero-field-cool measurements for the 420°C annealed sample used in GMR measurement.

The SANS results here, together with Co/Ag phase separation x-ray results, provide an explanation for the complex GMR behavior as a function of annealing temperature shown in Figure 5.7.4. The level of GMR within the system depends on the interparticle interactions between the Co nanoparticles. Two types of interparticle interactions are expected in this system, an RKKY-like interaction [16] which propagates through the Co impurities within the Ag matrix, and a dipolar interaction between Co nanoparticles. Before any annealing, both interactions are present. However, as the system is annealed phase separation begins and Co nanoparticles increase in size at the expense of decreasing Co impurities within the Ag matrix. For samples annealed below 300°C, the reduction in Co impurity is small compared to the increase in dipolar interaction due to the size increase of the Co nanoparticles. This results in a small overall increase in interparticle interactions within the system, and this causes a small drop in the GMR ratio. As the annealing temperature reaches 300°C (maximum GMR ratio), the majority of the Co impurities within the Ag matrix are removed, and at this point the RKKY-like interaction is greatly suppressed. Thus, the overall interactions between all the particles are at their minimum, and this leads to the observation of the maximum GMR ratio. As the annealing temperature increases further, the Co particles eventually agglomerate, resulting in a large increase in the dipolar interaction, which gives rise to the observed decrease in GMR.

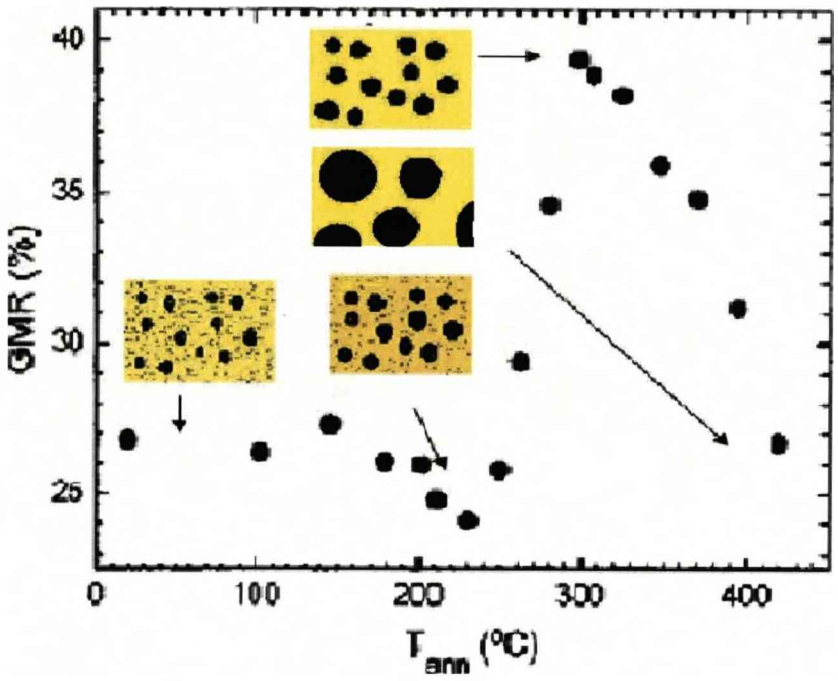

Fig. 5.7.4: GMR as a function of annealing temperatures. The insets show a graphical representation of Co nanoparticles and Co impurities in a Ag matrix after different annealing temperature.

5.8 Conclusion

In summary, I was able to determine the magnetic nanostructures of Co/Ag alloys using SANS, together with x-ray diffraction data. I found that the intricate dependence of GMR on annealing temperature arises from a phase separation between Co and Ag, and this followed by an agglomeration of particles at higher annealing temperatures. These results provide an understanding of the complicated, but highly desirable physical properties of a system that is easy to fabricate and, therefore, with potential for practical applications.

Bibliography

[1] M.N. Baibich, J. M. Broto, A. Fert, F. Nguyen Van Dau, F. Petroff, P. Eitenne, G. Creuzet, A. Friederich, and J. Chazelas, Phys.Rev.Lett. 61,2472 (1988)

[2] Q. Yang, P. Holody, S.-F. Lee, L. L. Henry, R. Loloee, P. A. Schroeder, W. P. Pratt, Jr., and J. Bass, Appl. Phys.Lett. 61. 1855 (1992)

[3] A. E. Berkowitz, J. R. Mitchell, M. J. Carey, A. P. Young, S. Zhang, F. E. Spada, F. T. Parker, A. Hutten, and G. Thomas, Phys. Rev. Lett. 68 3745 (1992)

[4] John Q. Xiao, J. Samuel Jiang, and C. L. Chien, Phys. Rev. Lett. 68 3749 (1992)

[5] John Q. Xiao, J. Samuel Jiang, and C. L. Chien. Phys.Rev. B 46, 9266 (1992)

[6] F. Parent, J. Tuaillon, L. B. Stern, V. Dupuis, B. Prevel, A. Perez, P. Melinon, G. Guiraud, R. Morel, A. Barthélémy, and A. Fert, Phys. Rev. B 55, 3683 (1997)

[7] C.L. Chien, J.Q. Xiao, and J.S. Jiang, J. Appl. 73 5309 (1993).

[8] S. Honda, M. Nawate, M. Tanaka, and T. Okada, J. Appl. Phys. 82, 764 (1997).

[9] Carey, M.J., A.P. Young, A. Starr, D. Rao, A.E. Berkowitz, and J.S. Jiang. Appl. Phys. Lett. 61, 2935 (1992)

[10] K. Ounadjela, S.M. Thompson, J.F. Gregg, A. Azizi, M. Gester, and J.P. Deville, Phys. Rev. B 54 12 252 (1996)

[11] S. Rubin, M. Holdenried, and H. Micklitz, Phys. J.B 5, 23 (1998)

[12] M.B. Stearns and Y. Cheng, J. Appl. Phys. 75, 6894 (1994)

[13] J. A. De Toro, J. P. Andres, J. A. GonZalez, J. P. Goff, A. J. Barbero, and J. M. Riveiro, Phys. Rev. B 70 224412 (2004)

[14] http://www.ill.eu/fileadmin/users_files/Other_Sites/lss-grasp/grasp_main.html

[15] Michael Bischof, Peter Staron, Andreas Michels, Petra Granitzer, Klemens Rumpf, Harald Leitner, Christina Scheu and Helmut Clemens, Acta Materialia 55 2637-2646 (2007)

[16] A. López, F. J. Lázaro, M. Artigas, and A. Larrea. Rev. B 66 174413 (2002)

[17] M. P. Wismayer, S. L. Lee, T. Thomson, F. Y. Ogrin, C. D. Dewhurst, S. M. Weekes, and R. Cubitt, J. Appl. Phys 99, 08e707 (2006)

[18] A. Heinemann and A. Wiedenmann, J. Appl. Cryst. 33, 1386 (2000)

[19]] A. Heinemann, J.Appl. Cryst. 33,1386 (2000)

Chapter 6

Co-CoO/Ag nanogranular systems

6.1 Motivation

Interest in ferromagnetic (FM) nanoparticles has been intense in recent years, owing to the wide range of potential applications, especially for ultrahigh density recording media [1-3]. One of the obstacles to further progress in the field is that below a certain critical size, FM nanoparticles are able to spontaneously change their magnetization direction due to thermal fluctuations, severely restricting their utility for data storage. This limits the size of the nanoparticles, ultimately leading to a limit on the maximum storage density of recording media. This is known as the "superparamagnetic limit".

One proposal to overcome the superparamagnetic limit is to surround the FM core of the nanoparticle with an exchange-biasing AF shell. Skumryev *et al.* have embedded Co particles in a CoO matrix and reported large exchange-bias due to a FM core and AF CoO shell [3]. In contrast to Skumryev *et al.*, who did not observe any exchange bias at all when they buried the core-shell particles in a nomagnetic Al_2O_3 matrix, De Tore and his co-workers achieved substantial exchange bias fields for Co-CoO core-shells in a nonmagnetic Ag matrix [5]. Furthermore, the Co-CoO/Ag nanogranular systems are produced by a simple reactive spattering technique that is more appropriate for applications.

The aim here is to determine the magnetic structure in nanogranular Co-CoO/Ag using small-angle neutron scattering in order to better understand the magnetic interaction and exchange bias.

6.2 Introduction

The results of the magnetisation studies of the Co-CoO/Ag nanogranular system studied here are summarised in Ref. [5]. Figure 6.2.1 shows bulk magnetization as a function of temperature for Co/Ag samples of the same nominal composition, but different oxygen pressures. Peaks in the zero-field cooling curves indicate freezing or blocking temperatures. As the oxygen pressure in the growth chamber increases, the blocking temperature first decreases, and then increases. Figure 6.2.2 shows magnetic hysteresis loops measured after the sample had been cooled in a large field. For large oxygen pressures there is a substantial shift in the hysteresis loop, indicating a large exchange bias field. The dependence of the blocking temperature and the bias field on oxygen pressure is summarised in figure 6.2.3. It is clear that substantial exchange bias fields are only found once the blocking temperature starts to increase.

In this chapter I shall employ SANS to see how the oxygen pressure in the growth chamber affects the magnetic structure of Co-CoO/Ag. In particular, it will be possible to test directly for the presence of an exchange biasing Co-O shell, measure the nanoparticle size distribution, and monitor magnetic impurities in the Ag matrix. These results should shed light on the interplay between exchange bias and blocking temperature in these nanoparticle systems.

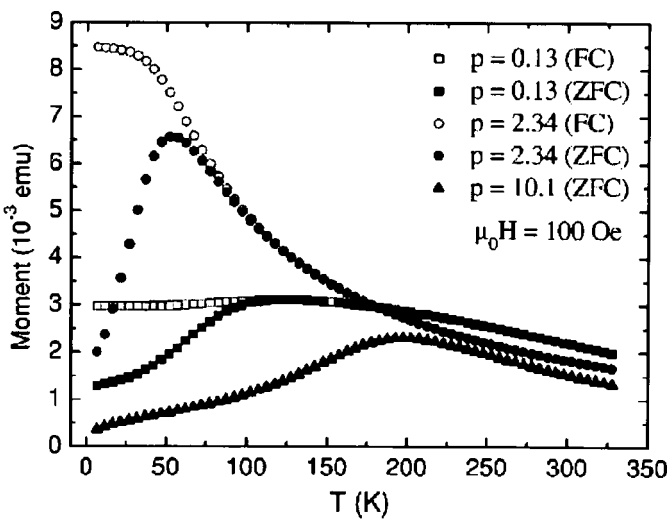

Figure 6.2.1: Field-cooled (FC) and zero-field-cooled (ZFC) magnetization measurements at 100 Oe for samples grown under different oxygen pressures, see text for definition of oxygen pressure, p.

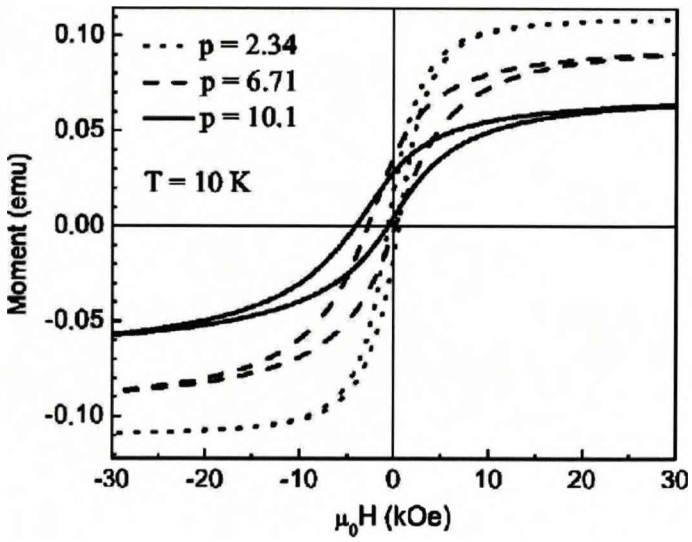

Figure 6.2.2: Hysteresis loops, measured at 10K after cooling from 380K in a field of 40kOe.

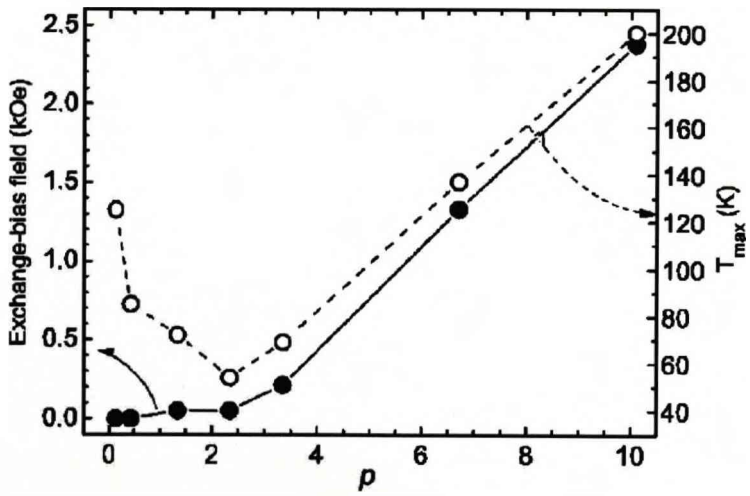

Figure 6.2.3: Oxygen pressure dependence of exchange-bias field and blocking temperature from ZFC measurements.

6.3 Sample growth

Nanogranular alloys of composition $Co_{22}Ag_{78}$ were prepared by Jose De Toro using rf magnetron sputtering at the Universidad Castilla-La Mancha. The samples were synthesized by rf magnetron sputtering using a composite Ag-Co cathode similar to the one used for the Co/Ag samples in the previous chapter. However one major difference is that in this case a controlled amount of oxygen was allowed into the chamber during sample growth. The total pressure in the chamber was 3×10^{-3} mbar comprising mostly Ar. In the following sections, I shall investigate samples, which were grown under an oxygen pressure, p, given by $p=1000P_O/P_{Ar}$=0.13, 1.34, 2.34 and 10.1.

6.4 Experimental procedure

The magnetic structure was studied by small-angle neutron scattering using D11 at the ILL, see chapter 3. In a neutron scattering experiment a large sample volume is required. Therefore due to the small amount of magnetic material in each thin film, it was necessary to form a coupon of samples to increase signal. Furthermore, the films were pealed away from the glass substrates to reduce the background. The stack of Co-CoO/Ag films was fixed together using two pieces of silicone giving a sample area of 28x4mm^2. For each SANS measurement a sample transmission measurement was also made to allow this correction to be made for data analysis.

6.5 Small angle neutron scattering (SANS)

In this section I shall present the results of the SANS measurements together with the modelling of the data.

2d SANS

Figure 6.5.1 gives an overview of the scattering patterns from Co-CoO/Ag samples with different oxygen pressure during growth. The SANS data were corrected for transmission, background and detector efficiency using a program called Grasp [9]. A 1T field was applied in a horizontal direction parallel to the surface of the sample and perpendicular to the incident beam. Since the scattering cross-section of neutrons is only sensitive to components of the magnetic moment perpendicular to Q this gives rise to an asymmetric scattering pattern. One observes as expected the scattering perpendicular to the applied field due to the Co-CoO/Ag particles. This scattering will be discussed in more detail later on in this section. However, also of interest is the scattering parallel to the applied field. Similarly to the Co/Ag system this scattering is attributed to the spin-misalignment scattering due to the Co impurities within the matrix [10]. This spin-misalignment scattering is reduced as the oxygen pressure increases, but, unlike the Co/Ag system, this scattering does not completely disappear as the oxygen ratio reaches p=10.1.

Most of the differences in the 2D plots can be attributed to the different counting statistics for each oxygen pressure, which was determined by the availability of material. For example, for p=2.34 only one film was measured. A more quantitative comparison is made in the next section after reducing the data to 1D.

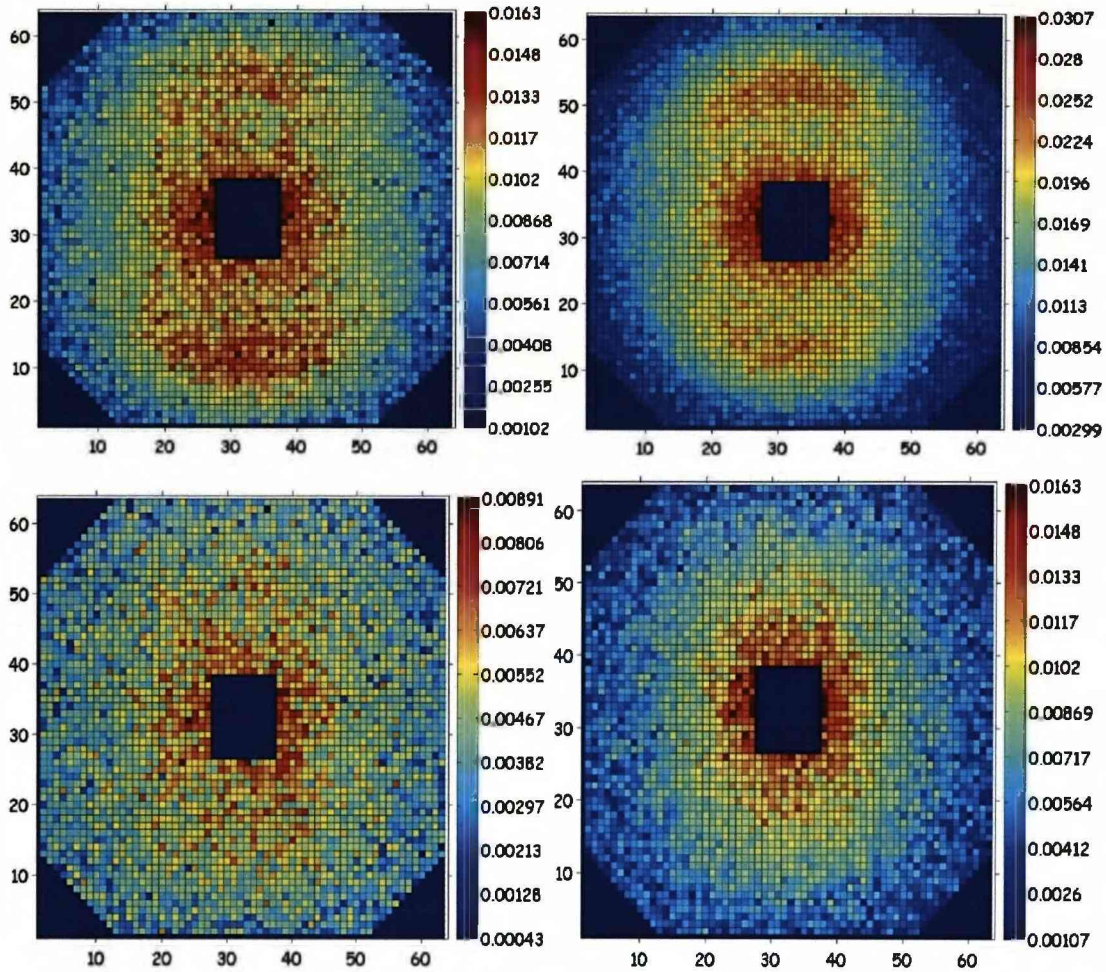

Figure.6.5.1: 2D scattering patterns from Co-CoO/Ag nanogranular samples with a 1T field applied along the horizontal direction: (top left) p=0.13, (top right) p=1.34, (bottom left) p=2.34, (bottom right) p=10.1.

1D SANS

The 2D SANS data was reduced to 1D using Grasp in the same way as described before in the last chapter. Figure 6.5.2 shows the offset φ for the lowest and the highest oxygen pressure sample, it shows that the change in φ is shifted to a lower Q as the oxygen pressure increases. This suggests that the spin-misalignment scattering is reduced due to the decrease in the contrast between the magnetic scattering length density of the Co and the matrix in the direction parallel to the field. However, unlike in Co/Ag system, the spin-misalignment scattering does not

completely disappear. This is presumably due to the matrix still remaining relatively rich in FM Co impurities compared to the Co/Ag sample after annealing at 420°C.

Figure 6.5.3 shows the magnetic scattering intensity for samples grown under different oxygen pressures. Clearly the changes to the scattering are subtle and the qualitative form of the Q dependence remains the same in each case. Nevertheless there are systematic trends in the data, such as the movement of the peak maximum to lower Q as the oxygen pressure is increased.

Although these samples have a different nominal composition, $Co_{22}Ag_{78}$, to those used in the annealing experiments in the previous chapter, $Co_{29}Ag_{71}$, the results for the sample with the residual oxygen level p=0.13 are similar to those from the annealed sample in the previous chapter, see figure 5.7.4. The data sets were, therefore, analyzed using the same polydisperse diffusion-zone particle model used in chapter 5 and described in more detail in chapter 3. The solid lines in figure 6.5.4 are the results of a least-squares fit, and there is excellent agreement between the model and the data for all oxygen pressures.

Figure 6.5.4 shows the variation of the magnetic scattering length density as a function of distance from the centre of the particle for each oxygen pressure, and the fitted parameters are summarized in table 6.5.1. The trends in the fitted parameters for the samples in this chapter are, of course, completely different to those of the previous chapter, because the physical meaning of the parameters is totally different.

The FM particle radii (1.7 – 1.5nm) obtained from fits of the Langevin function to magnetization loops [5] are in reasonable agreement with SANS results (1.7 – 1.3nm) in Table 6.5.1. The fact that the results of the more sophisticated model here is consistent with the simpler magnetization model is encouraging. The reduction in size of the FM particles has a simple interpretation. An increased oxygen pressure will result in increased oxidation of the surface of the Co nanoparticles. Since CoO is AF this naturally leads to a reduction in the radius of the FM nanoparticles. The remaining FM core is found to have a fixed SLD.

In this chapter the diffusion zone is interpreted as a CoO shell. Since CoO is AF the magnetic scattering length density of the shell is fixed at zero. The size of the diffusion zone increases with increasing oxygen pressure. Again this result is checked for consistency with the magnetization data. The reduction in the size of the total moment of the nanoparticles obtained in fits of the Langevin function gives an estimate of the shell thickness of ~ 0.4nm for p=10.1[5]. The fitted shell size using the

more extensive SANS modelling is ~ 0.6nm, and this is at least comparable to the simpler magnetization result.

The fact that the particle sizes and the shell sizes are consistent with the bulk magnetization data gives confidence when dealing with parameters of the model that cannot obtained using bulk techniques, such as the particle size distribution and the magnetic impurities within the matrix.

The width of the particle size distribution is seen to increase steadily with increased oxygen pressure. This is by no means an obvious result. It is telling us that, all particles do not oxidise at the same rate, giving the same shell thickness. Instead, for a given oxygen pressure, different particles oxidise at different rates. One way in which this could happen would be if the formation of an oxide layer eventually formed a barrier to further oxidation. This would prevent the larger particles from being oxidise extensively, leaving big particles, while smaller particles could be almost completely oxidised, leaving small particles and extending the range of sizes. The large distribution of sizes means the comparison of particle size and shell thickness with bulk magnetization studies is only approximate.

Finally, in order to fit the data, a substantial reduction in the magnetic scattering length density of the matrix is required, see table 6.5.1. Again this has a natural interpretation in the present model. The Co impurities in the Ag matrix will also be further oxidised at greater oxygen pressure. The tiny islands of CoO will tend to have no net moment, so that the average magnetic moment in the matrix decreases.

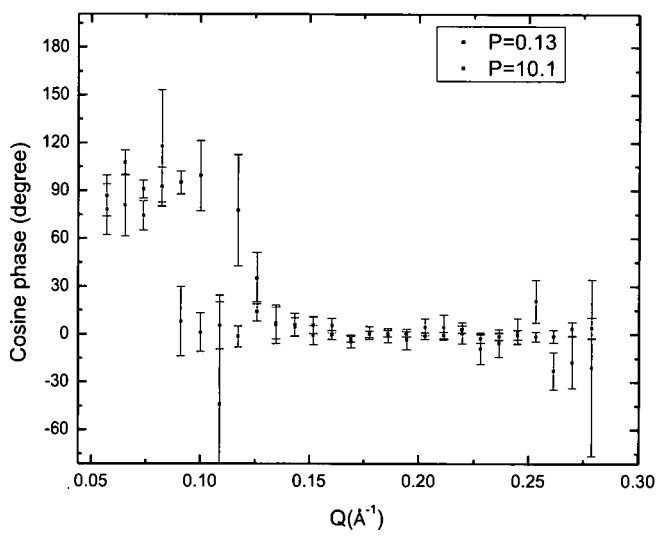

Figure 6.5.2: Variation in θ as a function of Q for different oxygen pressures.

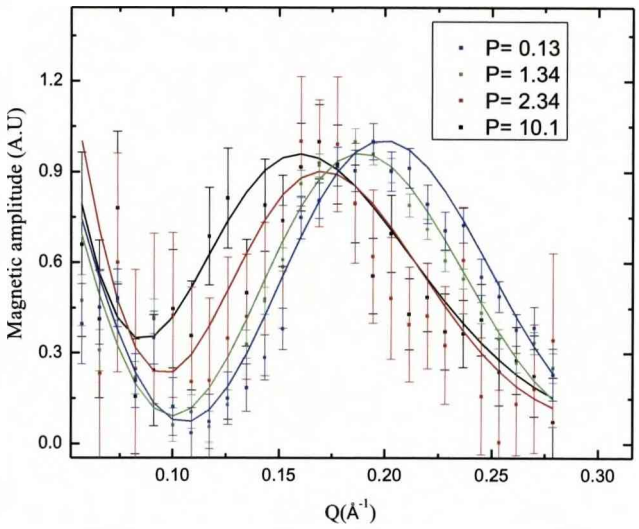

Figure 6.5.3: Magnetic scattering intensity of the Co/Co-O/Ag nanoparticle system with 1T applied field. Lines through data points are fits using a polydisperse diffusion-zone particles model.

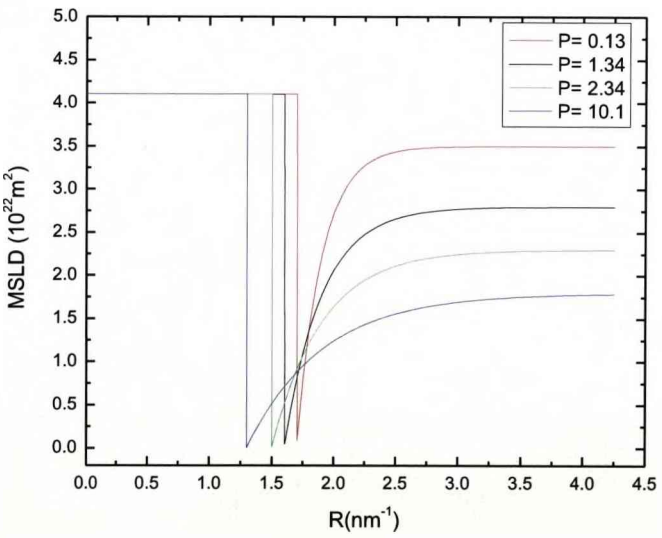

Figure 6.5.4: The magnetic scattering length density as a function of distance from the centre of the FM core for samples with different oxygen ratios during growth.

P_O/P_{AR}	Particle radius ± 0.2nm	Diffusion zone ± 0.1nm	MSLD particle ± 0.2 $(\times 10^{14})m^2$	MSLD diffusion zone $(\times 10^{14})m^2$	MSLD matrix ± 0.2 $(\times 10^{14})m^2$	Sigma ± 0.01
0.13	1.7	0.2	4.1	0.0	3.5	0.07
1.34	1.6	0.3	4.1	0.0	2.8	0.09
2.34	1.5	0.4	4.1	0.0	2.3	0.14
10.1	1.3	0.6	4.1	0.0	1.8	0.17

Table 6.5.1: Summary of all the fitted parameters for different growth oxygen ratios.

6.6 Discussion

The polydisperse diffusion-zone particle model is the simplest model that is able to reproduce the observed SANS data. As was described in the previous chapter, simpler models such as particles in a matrix with no diffusion zone are unable to capture all aspects of the scattering. Furthermore, the polydisperse diffusion-zone particle model yields a self-consistent set of fitted parameters that agree with bulk magnetization results. The SANS experiment yields more detailed information than can be obtained from fits of Langevin functions to magnetization loops. For example SANS allows one to construct a complete magnetic structure of the system, provides information on particle core and shell size as well as MSLD of the core, shell and matrix, whereas magnetization measurement can only yield the magnetic particle core size (less accurately as exchange biasing introduce extra anisotropy). As will be discuss later in this section the ability to determine the shell size and how MSLD changes as a function of oxygen pressure is essential to the understanding of the changes in the magnetic behaviour within this system.

The neutron results allow us to understand all of the behaviour displayed in figures 6.2.1, 6.2.2 and 6.2.3. First, the initial drop in the freezing temperature as oxygen is introduced into the chamber, see figure 6.2.1 and 6.2.3, can readily be explained by the oxidation of the Co impurities in the Ag matrix. Co impurities passivated by oxidation to CoO, since the AF impurities are unable to mediate the RKKY-like interaction. The accompanying reduction in interactions between

nanoparticles results in a lowering of the freezing temperature, this is in good agreement with the SANS result where a drop in matrix MSLD was observed indicating the removal of magnetic material. Secondly, the fact that a critical oxygen pressure is required before the observation of exchange bias could mean that the oxide shell needs to reach a certain thickness before it is able to pin the Co core. For thicker shells and higher oxygen pressure the dynamics will be dominated by exchange bias rather than interaction between particles. This view is supported by the fact that the onset of exchange bias occurs at the same point as the minimum in freezing/blocking temperature in figure 6.2.3. Again this is well supported by our SANS data where it shows the CoO shell size increases as a function of increasing oxygen pressure.

The observation of core-shell Co-CoO here in a nonmagnetic Ag matrix is a much cleaner result than that reported earlier for Co-CoO in a CoO matrix [3]. In fact, the observation of exchange bias for Co in CoO matrix is hardly surprising since that is the system investigated by MeikleJohn and Bean [12]. Here we are addressing a new phenomenon.

6.7 Conclusions

We are able to study the oxidation processes for Co nanoparticles in a Ag matrix grown using a rather messy reactive sputtering technique. We obtain very clean measurement using SANS since the result of oxidising FM Co is to produce AF CoO, with strongly contrasting magnetic signal. Oxidation first reduces interactions between particles due to the removal of FM Co impurities in the matrix. Then, once the CoO shell around the nanoparticle is sufficiently thick, exchange bias takes over.

Bibliography

[1] L. Del Bianco, Dino Fiorani, Alberto M. Testa. Ennio Bonetti, Luca Signorini, Phys. Rev. B 70 052401 (2004)

[2] J. Nogués and I. K. Schuller, J. Magn. Magn. mater. 192, 203 (1999)

[3] Skumryev, S. Stoyanov, Y. Zhang, G. Hadjipanayis, D. Givord, and J. Nogues,, Nature (London) 423, 850 (2003)

[4] K. Liu, S. M. Baker, M. Tuominen, T. P Russell and I. K. Schuller, Phys. Rev B 63 060403 (2001)

[5] M. Riveiro, J. A. De Toro, J. P. Andre's, J. A. Gonza'lez, T. Mun~oz, and J. P. Goff, App. Phys. Lett. 86, 172503 (2005)

[6] J.B. Yi, **J**. Ding, B.H. Liu, Z.L. Dong, T. White and Y. Liu, J. Magn. Magn. mater. 285, 224 (2005)

[7] J. A. De Toro, J. P. Andrés, J. A. González, P. Muñiz, T. Muñoz, P. S. Normile, and J. M. Riveiro, Phys. Rev. B 73 094449 (2006)

[8] P. S. Normile, J. A. De Toro, T. Muñoz, J. A. González, J. P. Andrés, P. Muñiz, R. E. Galindo, and J. M. Riveiro, J App. Phys. 100, 064312 (2006)

[9] http://www.ill.eu/fileadmin/users_files/Other_Sites/lss-grasp/grasp_main.html

[10] M. Bischof, P. Staron, A. Michels, P. Granitzer, K. Rumpf, H. Leitner, C. Scheu and H. Clemens, Acta Materialia 55 2637-2646 (2007)

[11] A. Heinemann and A. Wiedenmann, J. Appl. Cryst. 33, 1386 (2000)

[12] W. H. MeikleJohn and C. P. Bean, Phys. Rev. 105, 904 - 913 (1957)

Chapter 7

Nanoparticle systems

7.1 Motivation

Magnetic nanoparticles have a wide range of potential application in diverse area such as data storage [1-3], sensors [4] and medical drug delivery systems [5]. Often the interactions between these nanoparticles cause them to behave collectively and limit their potential in model applications. The interaction will limit the size and distance between the particles, thus reducing the maximum obtainable recording density for nanoparticles. One motivation for the study of ordered arrays is that, the formation of ordered arrays can potentially maximise the distance between particles and, therefore, minimise interactions between them. Studies were performed for Co nanoparticles, where a core-shell model is required as for chapter 5 and 6. Control measurements were also performed for Fe_2O_3 nanoparticles, which do not have the complication of a shell.

7.2 Introduction

In this chapter I shall present detailed structural and magnetic studies of self-assembled Co and Fe_2O_3 nanoparticles, where interparticle interactions are expected. I shall start with details of the sample growth and experimental techniques. This will be followed by a description of a Transmission Electron Microscopy (TEM) study, which yields information on the shape, size, nanoparticle coverage, and size distribution of the two nanoparticle systems. However, TEM studies only cover a relatively small area of the sample. Therefore, after the TEM study I shall present SANSPoL studies which provide more information on the shape, size and particle size distribution, as well as their packing fraction, statistically averaged over the whole sample. Furthermore owing to the magnetic spin moment of the neutrons, SANS techniques also provide unique information about the magnetic structure of the

system. The use of polarised neutrons in SANSPoL dramatically increases sensitivity to the magnetic ordering. To create a complete picture of the magnetic structure and interactions of these systems I shall present field cooled and zero field cooled magnetisation measurements, together with hysteresis loops for the two nanoparticle systems after field- and zero-field-cooling from above their blocking temperatures.

7.3 Sample growth

All samples studied in this chapter were grown in the Department of Chemistry at the University of Liverpool by Ian Robinson and Thanh Nguyen. A simple one-step method was used for the synthesis of monodisperse magnetic nanoparticles coated with a thermo-responsive polymer [7,8]. After growth the nanoparticles are stored in a toluene solution.

Due to the low penetration length of elections in materials, TEM measurements can only be performed on one to two monolayers of nanoparticles. TEM samples were created from a toluene solution containing Co or Fe_2O_3 nanoparticles. 1 ml of the diluted solution was deposited on a Cu TEM grid at room temperature giving thin layers of nanoparticles on the surface. The TEM gird was then placed on top of some absorbing paper to take away any excess solution. After deposition the TEM grid was covered by a glass lid to slow down the evaporation rate.

Samples for SANSPoL measurements were produced in a similar way, but instead of dropping the diluted solution onto a TEM grid, a $25\text{mm} \times 10\text{mm}$ silicon (111) surface with thickness of 2mm was used. Due to the larger surface area of the silicon 4-5 of the 1 ml drops were used. Silicon wafers are almost perfect crystals with very few imperfections. They, therefore, give very little scattering at low angles and, they give very low background in SANS measurements. Furthermore, even with the extra drops, the amount of nanoparticles deposited on any given silicon surface is still very small. Therefore, in order to improve the signal, 12 pieces of silicon with nanoparticle arrays were stacked together to increase the scattering intensity.

7.4 Experimental procedure

TEM was performed in the Department of Engineering at the University of Liverpool using a high resolution TEM (JEOL FX2000) operated at 200kV, allowing the observation of Co and Fe_2O_3 nanoparticles. TEM pictures were taken using a digital camera and the pictures were analysed using the ImageJ graphic analysing software [9].

Magnetisation measurements were performed using a Quantum Design SQUID magnetometer with a temperature range 2-400K and a maximum field of 7T. Hysteresis loops were measured after field-and zero-field cooling from above the nanoparticles blocking temperature. The temperature dependence of the field-cooled and zero-field-cooled magnetization was also measured. Due to the high sensitivity of SQUID measurements only small amounts of sample are required. Therefore, the TEM grids with deposited nanoparticles were sufficient for the SQUID measurements.

Polarised small angle neutron scattering (SANSPoL), was performed on both nanoparticles system, using the V4 SANS instrument at HMI, Berlin, see chapter 3 for further details on V4. The samples were mounted with the silicon surface perpendicular to the direction of the incident neutron beam and a 1.1 T field was applied in the horizontal direction parallel to the surface. The incident beam was polarised along the field direction and a flipper was employed to switch between parallel and anti-parallel states. The scattering from the two different incident neutron spin states was measured separately, and all the measured data were corrected for detector efficiency, transmission and background before data reduction. All of the correction and reduction of the data was done by using analysis software called BerSANS [10].

7.5 TEM results

This section presents the results of the TEM measurements on Co and Fe_2O_3 nanoparticle arrays, giving their shape, size and size distribution over small regions of the sample. The Cu TEM grid contains 300×300 squares each with dimensions of $250\text{nm} \times 250\text{nm}$. Figure 7.5.1 shows an overview of an empty TEM grid. The dark lines are the copper grid and the lighter squares are the carbon coating.

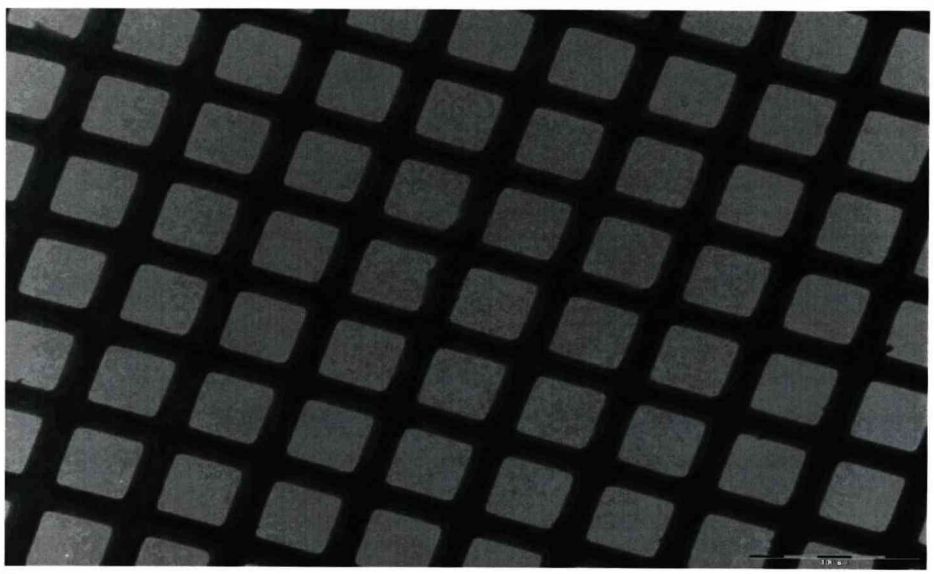

Figure 7.5.1: TEM picture of a Cu TEM grid.

Co nanoparticles

Figure 7.5.2 shows a TEM image, which presents an overview of the TEM grid with Co nanoparticles deposited on the surface. We have found over many different grids that the Co nanoparticle area coverage is over 50%. The brightest square in the picture is believed to be a broken carbon grid and no nanoparticles were found in the bright part of that square. The dark patches in the picture contain highly dense regions of nanoparticles grown in island mode. Because of the high density very few electrons penetrate and, therefore, it appears to be very dark on the picture.

Figure 7.5.3 shows an area where the grid was undamaged and with a low enough number of nanoparticle layers for electrons to pass through. The image shows that the Co nanoparticles are mostly spherical and form hexagonally ordered clusters. The majority of the grid contains such ordered arrays of nanoparticles but there are some patches where the nanoparticles are not ordered. Figure 7.5.4 shows an image

where the nanoparticles are ordered on the right but disordered on the left. The disorder seems to be accompanied by a higher density of nanoparticles, possibly due to the formation of more than one layer. After many TEM measurements it was found that if the nanoparticles are left for a long time before deposition onto a surface, it becomes more difficult to obtain an ordered array. Presumably over time an increase in oxidation causes the nanoparticles to become more polydisperse, as each particle may oxidise at a different rate. The accompanying increases in width of the particle size distribution may cause the creation of disordered arrays.

After the pictures were taken an analysis program called ImageJ was used to extract the mean particle size and their size distribution. Figure 7.5.5 shows the fitted size distribution of the nanoparticles as extracted from the TEM image. The analysis of the TEM image also shows that the nanoparticles have a mean radius of 4.1±0.1nm.

Finally, it is worth noting that, due to the lack of electron absorption contrast, TEM cannot distinguish between the Co core and CoO shell in the particles, and cannot see the solvent and organic shell.

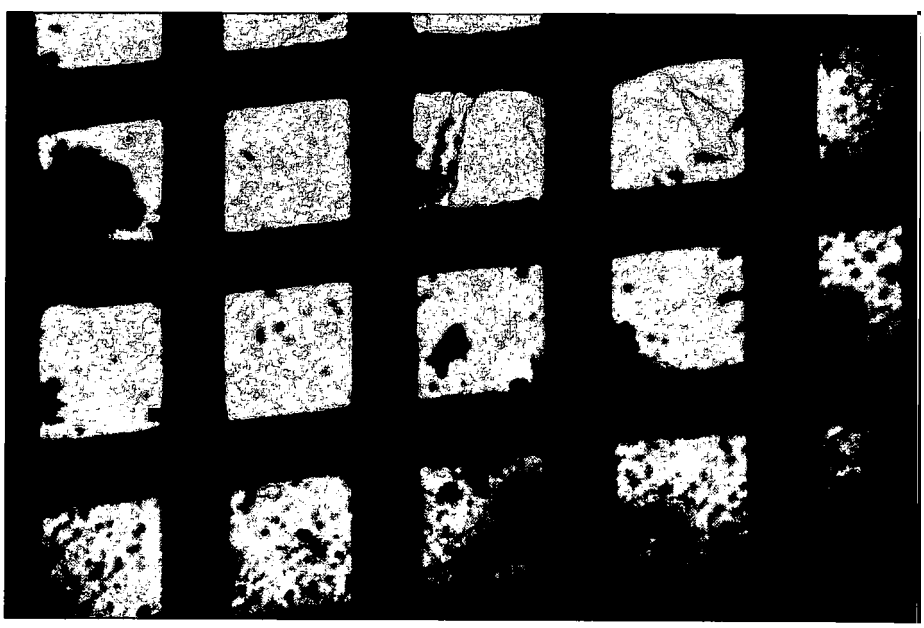

Figure 7.5.2: TEM image of Co nanoparticles deposited on a Cu TEM grid, showing both breakage of the carbon coating and some dark patches of island growth.

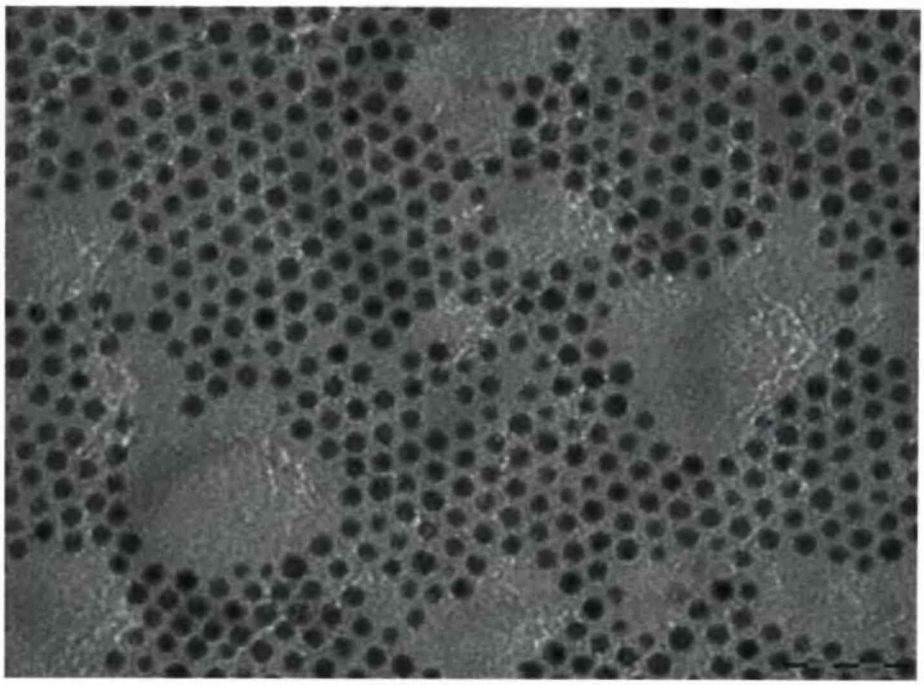

Figure 7.5.3: TEM image of Co nanoparticles deposited on a Cu TEM grid, showing a high level of hexagonal ordering.

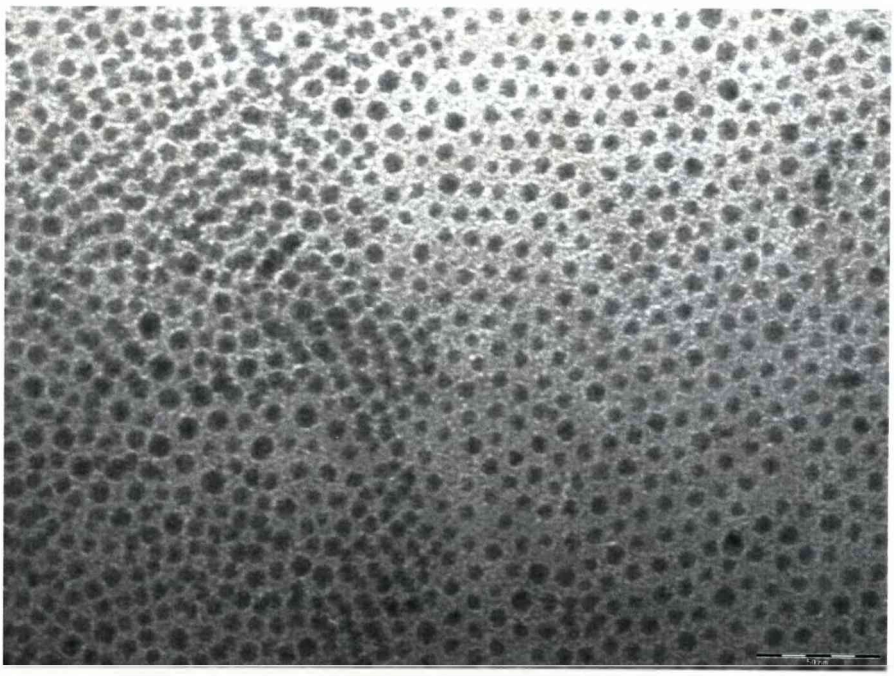

Figure 7.5.4: TEM image showing an ordered region on the right and a disordered region of Co nanoparticles on the left.

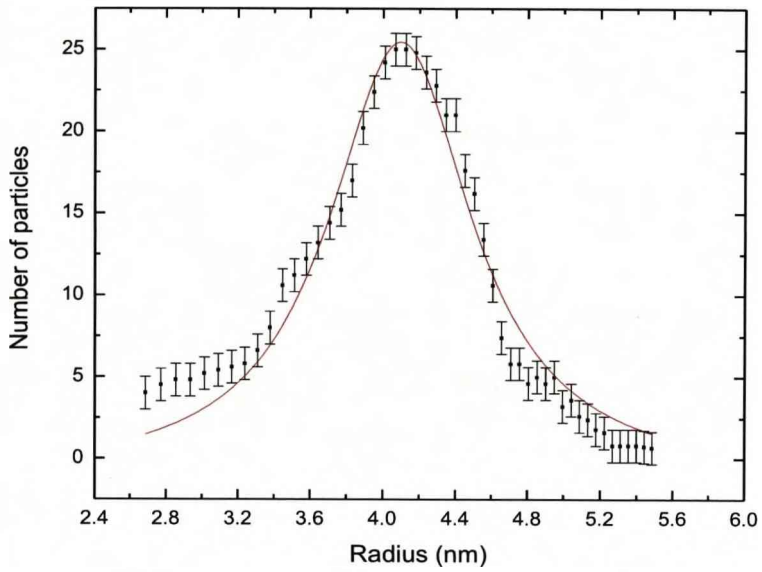

Figure 7.5.5: Co nanoparticle size distribution extracted from a TEM image.

Fe_2O_3 nanoparticles

Figure 7.5.6 is a TEM image showing an overview of the Fe_2O_3 nanoparticles. Fe_2O_3 nanoparticles do not order as easily as the Co nanoparticles. However, some small clusters of ordered arrays can be found on some parts of the TEM grids, see for example figure 7.5.7. The Fe_2O_3 nanoparticle area coverage is in the range 40-50%, and is similar to, but slightly lower than that observed for the Co nanoparticles. These TEM images also show that Fe_2O_3 nanoparticles are again mostly spherical. The dark spots in figures 7.5.6 and 7.5.7 may be due to larger particles, or even particles directly above one another. Analysis using ImageJ showed that the mean nanoparticle radius is 4.4±0.1nm, but the size distribution of the particles displayed in Figure 7.5.8 is noisier than the corresponding data for the Co nanoparticles.

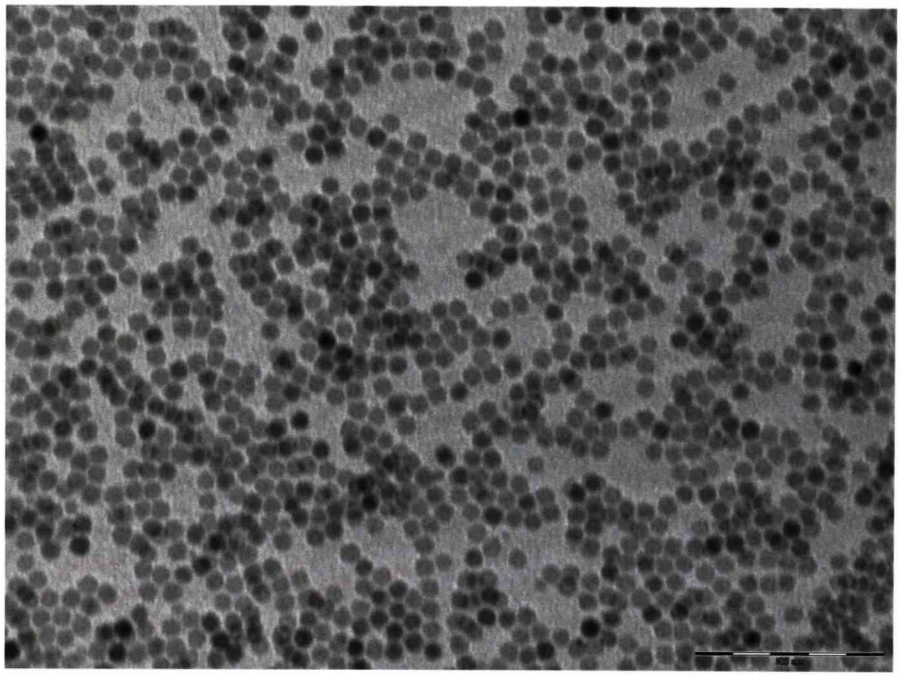

Figure 7.5.6: *TEM image of Fe_2O_3 nanoparticles deposited on a TEM grid.*

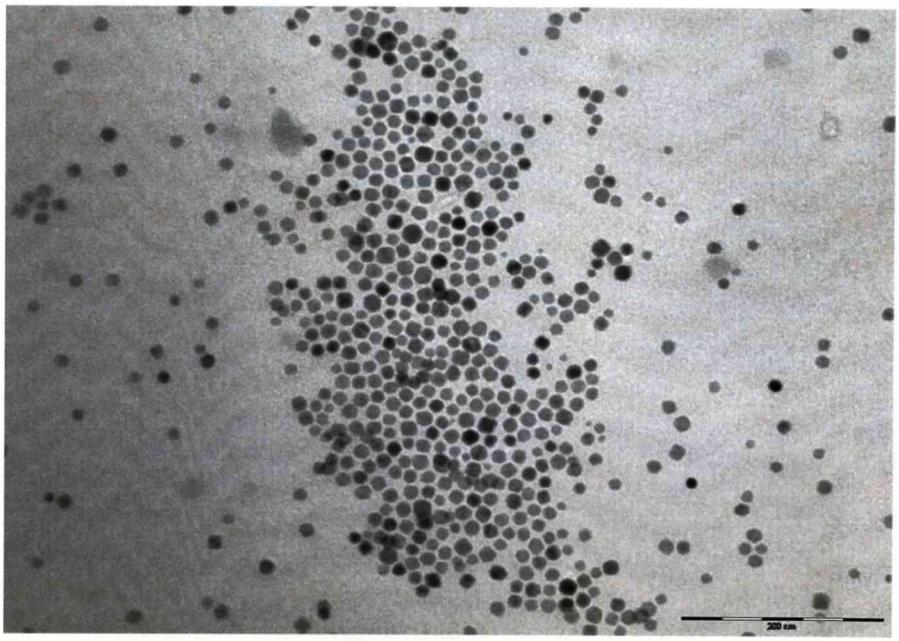

Figure 7.5.7: TEM image of Fe_2O_3 nanoparticles deposited on a TEM grid.

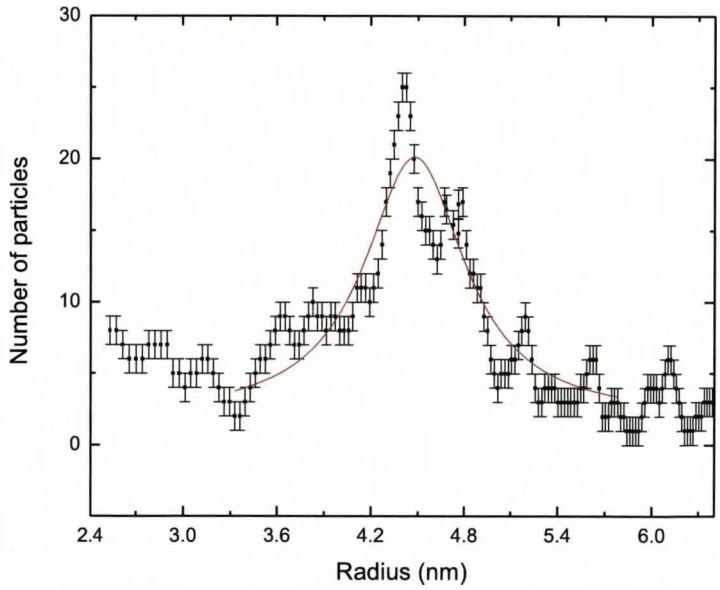

Figure 7.5.8: Fe_2O_3 nanoparticle size distribution extracted from a TEM image.

7.6 Magnetometry results

Co nanoparticles

Figure 7.6.1 shows zero-field and field-cooled magnetisation measurements, The Co nanoparticles exhibited a higher than expected blocking temperature, T_B~235K. For 4.1nm nanoparticles the expected blocking temperature was estimated to be 209K by using the relationship $T_B = \frac{KV}{25k_B}$, where K is 2.5×10^5 J/m^3 using the anisotropy constant for bulk FCC cobalt, V is the volume of the particles, and k_B is Boltzmann's constant. One possible explanation for the higher than expected blocking temperature is that the outside of the Co nanoparticles is surrounded by an AF cobalt oxide shell. This antiferromagnetic oxide layer gives rise to exchange-bias interaction in the same way as described in the previous chapter, and this provides extra anisotropy energy for the Co nanoparticles. Using the mean size of the nanoparticles obtained from TEM and later this chapter using SANSPoL, together with the blocking temperature obtained here, the anisotropy energy of the Co nanoparticles is estimated to be 2.8×10^5 J/m^3. The result of this extra anisotropy energy is that a higher

temperature is needed to thermally overcome the energy barrier for the nanoparticles to change their moment direction due to thermal fluctuation and, therefore, become superparamagnetic. Figure 7.6.2 shows the hysteresis loop for Co nanoparticles after zero-field-and field-cooling from 350K to 2K. The shift of the hysteresis loop of more than 1000 Oe in the field-cooled measurement provides direct confirmation of the exchange-bias interaction within this system.

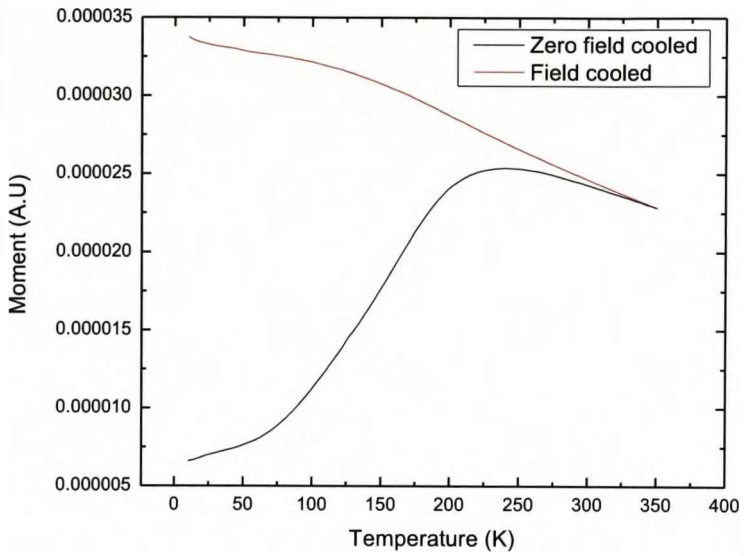

Figure 7.6.1: Magnetisation measurements for the Co nanoparticle system.

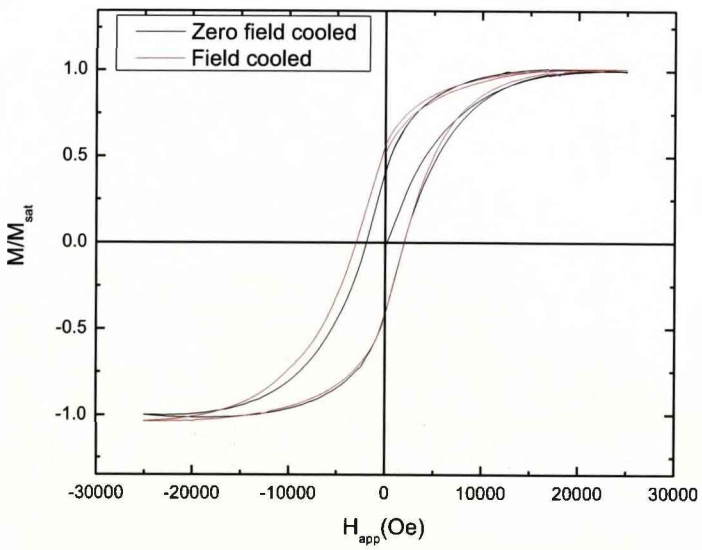

Figure 7.6.2: Hysteresis loops for the Co nanoparticle system at 2K. There is a shift in the hysteresis loop so that it is no longer centred on zero after cooling in a field.

Fe_2O_3 nanoparticles

Figure 7.6.3 shows the field-cooled and zero-field-cooled magnetization measurements for Fe_2O_3 nanoparticles, which has a blocking temperature of about 75K. This is much lower then the calculated value of 124K assuming the bulk gamma-Fe_2O_3 anisotropy constant of 1.2×10^4 J/m^3. Since Fe_2O_3 nanoparticles do not have an AF shell around the core, there is no possibility of an exchange-bias interaction to stabilise the Fe_2O_3 nanoparticles. Direct evidence for the absence of exchange biasing comes from the hysteresis loops for the Fe_2O_3 nanoparticles at 2K, figure 7.7.4 shows these hysteresis loops after cooling the sample in a 2T field and without a field to 2K. The fact that there is no shift in the hysteresis loop after field cooling confirms the absence of the exchange-bias interaction for this system.

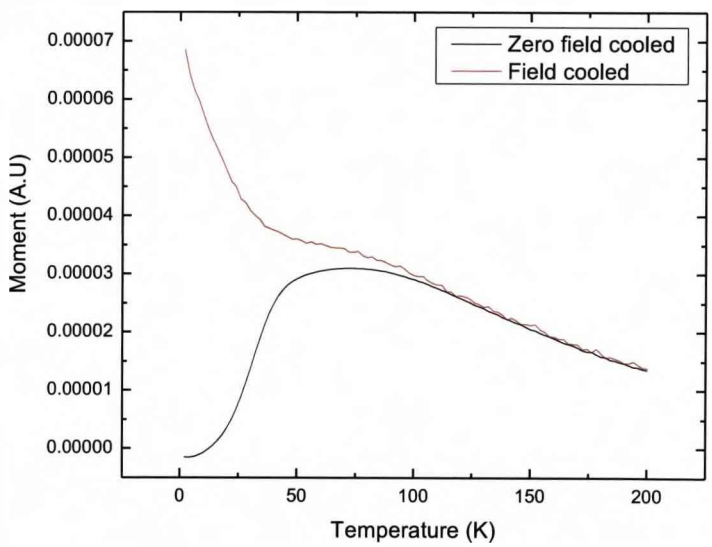

Figure 7.6.3: Field cooled and zero field cooled measurements for the Fe_2O_3 nanoparticle system.

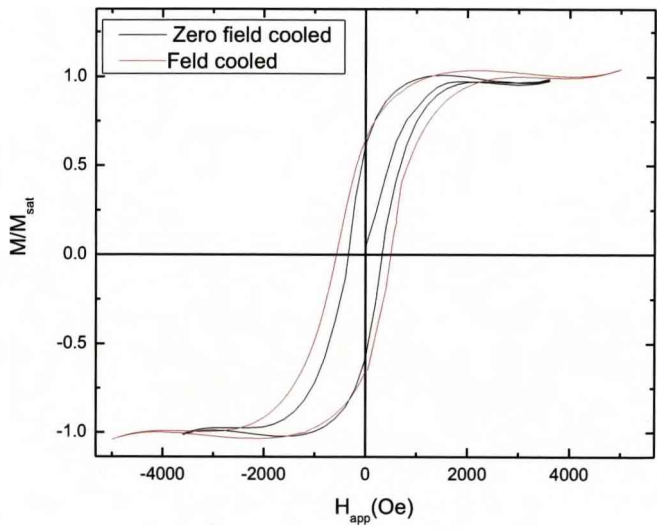

Figure 7.6.4: Hysteresis loops for the Fe_2O_3 nanoparticle system at 2K. In this case there is no shift in the hysteresis loop after cooling in a field.

7.7 SANSPoL results

In this section I shall present the results of the SANSPoL measurements on Co and Fe_2O_3 samples. The advantage of SANSPoL over conventional SANS is that SANSPoL makes use of the two different incident spin polarizations of the neutrons. The two spin states have a different magnetic scattering cross-section, which provides extra magnetic contrast during scattering experiments. Therefore, it is ideal for nanoparticle systems where the magnetic scattering signal is small due to the tiny amount of nanoparticles. In this section I shall present the SANSPoL data and try to obtain a model for the magnetic structures of the two nanoparticle systems.

Co nanoparticles

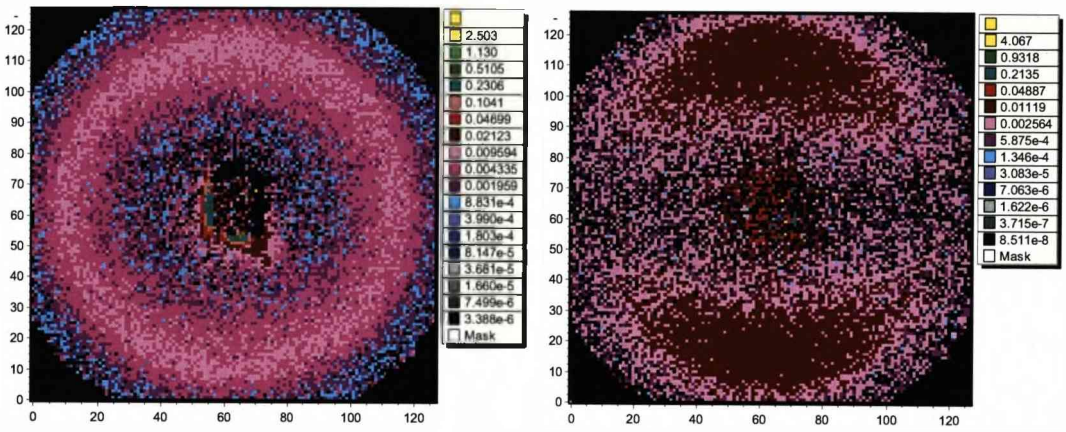

Figure 7.7.1: SANSPoL from a Co nanoparticle sample with a 1.1T applied field. The plots show 2D data after correction for transmission and background. Left is the sum of the SANSPoL with flipper on and off, right is the difference between flipper on and off.

Figure 7.7.1 shows the 2D SANSPoL for Co nanoparticles under a 1.1T saturating field. The plot on the left shows the sum of the scattering intensity for incident polarised neutron moment anti-parallel (flipper on) and parallel (flipper off) to the field. The right hand plot shows the scattering intensity for flipper on minus flipper off. Taking the sum of the two cross sections gives the unpolarised result, see equation (3.1.4.20), and one observes both the structural and magnetic scattering. However, as the structural and purely magnetic scattering cross sections are the same for the two neutron polarization states, by taking the difference in scattering intensity

between the two polarization states one obtains the structural-magnetic cross term, see equation (3.1.4.21). The magnetic scattering and the structural-magnetic cross term have the same angular dependence.

Thus, the 2D SANS data was reduced to 1D by fitting the function $A(Q)+B'(Q)Cos^2\alpha$ at constant wave-vector transfer Q. Figure 7.7.2 contains the reduced structural scattering data. The line through the data points is the best fit to a core-shell particle model [11] with a hard sphere Percus-Yevick structure factor [12-13], as described in chapter 3. Many attempts to describe the data with a simpler single core particle model with or without Percus-Yevick structure factor were unsuccessful, as the simpler model was unable to capture the 2nd maximum at 1.3nm^{-1} wavevector transfer. Figure 7.7.3 shows the best fit using a single particle model with Percus-Yevick structure factor. Figure 7.74 shows the simulation of a core-shell model without any structural factor, and this clearly demonstrates the need to include interparticle correlations. Figure 7.7.5 shows the structure factor obtained by calculating the Fourier Transform of the nanoparticle positions given by TEM measurements and the resultant S(Q) shows reasonable agreement with the S(Q) calculated using Percus-Yevick structure factor displayed in figure 7.7.6. Furthermore, from TEM images like those in Figures 7.5.3 and 7.5.4 the interparticle separation of the hexagonally ordered regions is estimated to be 10nm. Thus, sharp diffraction peaks are expected for the hexagonal {1,0}, {1,1} and {2,0} reflections at Q ~ 0.73, 1.26 and 1.46 nm^{-1}, respectively. These sharp Bragg reflections are not observed and the broad peaks in Figure 7.7.2 are instead consistent with the short-range order that arises from a hard-sphere model. Detailed modelling of the data reveals that the nanoparticles are closely packed with a packing faction of 0.49±0.02, and the nanoparticles consist of 4.0±0.2nm core radius, with a 0.4±0.1nm shell surrounding it. The core of the nanoparticles is mostly cobalt with a scattering length density of $2.2\pm0.1\times10^{14}\ m^2$ similar to those observed in other Co systems and the Co/Ag system in the previous chapters. More interestingly the model shows the scattering length density of the shell is $3.3\pm0.2\times10^{14}\ m^2$, which is lower than expected for cobalt oxide, which suggests the shell is not pure cobalt oxide as cobalt oxide has a scattering density of $4.27\times10^{14}\ m^2$. However it is possible that the organic shell that surrounded the nanoparticles mixed with some of the cobalt oxide or

not all the cobalt at the shell is oxidised, resulting in the small reduction of the scattering length density of the shell.

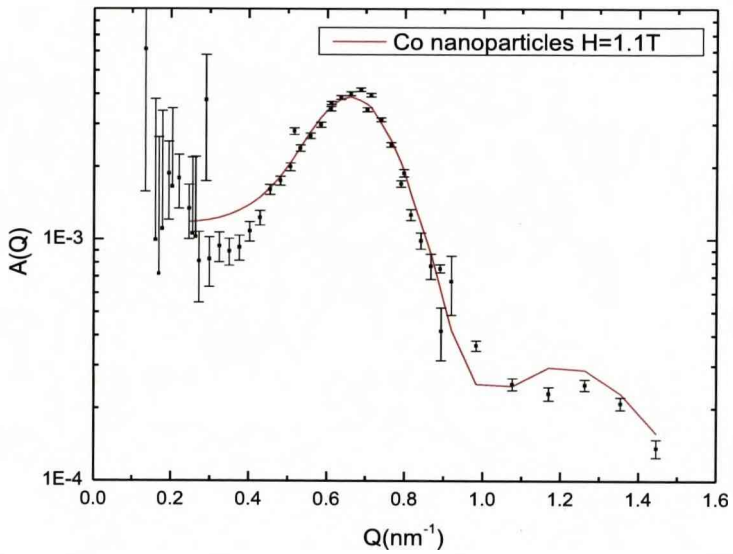

Figure 7.7.2: Structural scattering from Co nanoparticles system, the line through the data points is the best fit to a close packed polydisperse core-shell particle model.

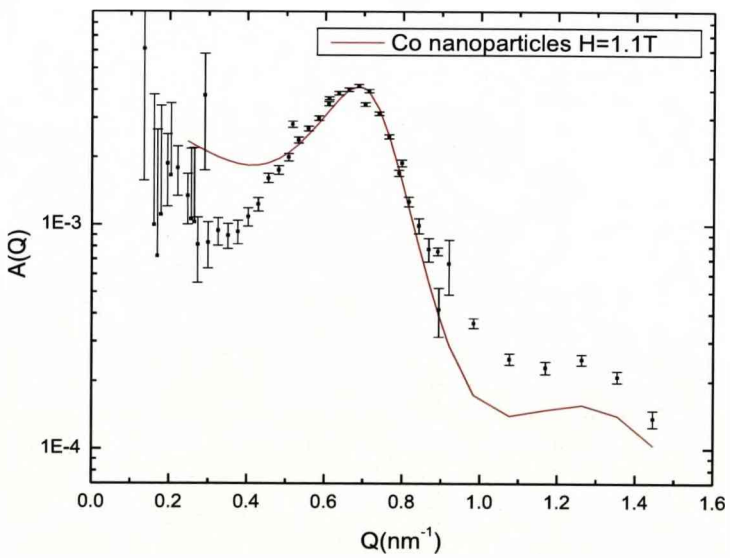

Figure 7.7.3: Structural scattering from Co nanoparticles system, the line through the data points is the best fit to a close packed polydisperse single core particle model.

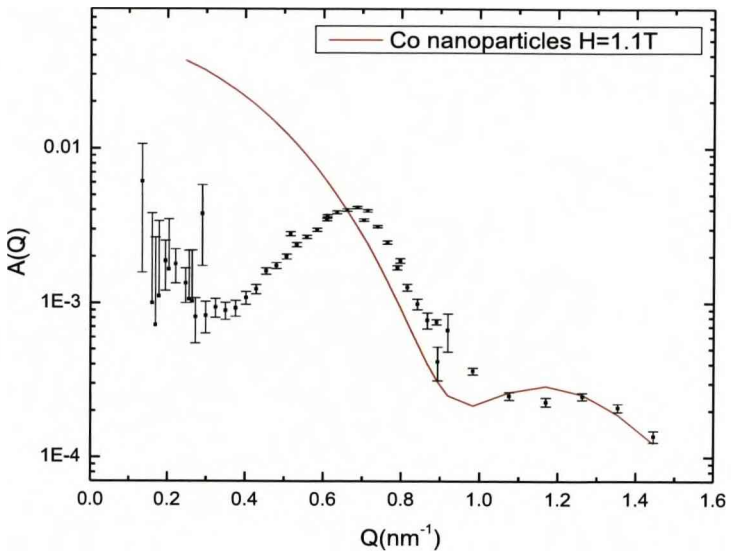

Figure 7.7.4: Simulation of core-shell model without any structural factor.

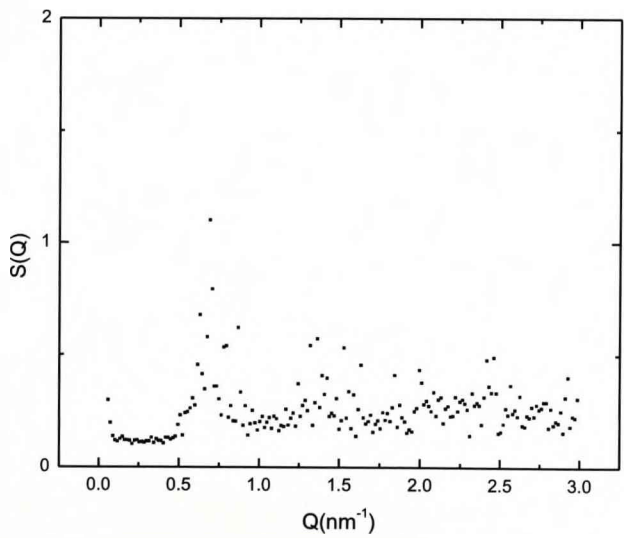

Figure 7.7.5: Fourier transforms of nanoparticles positions given by TEM analysis.

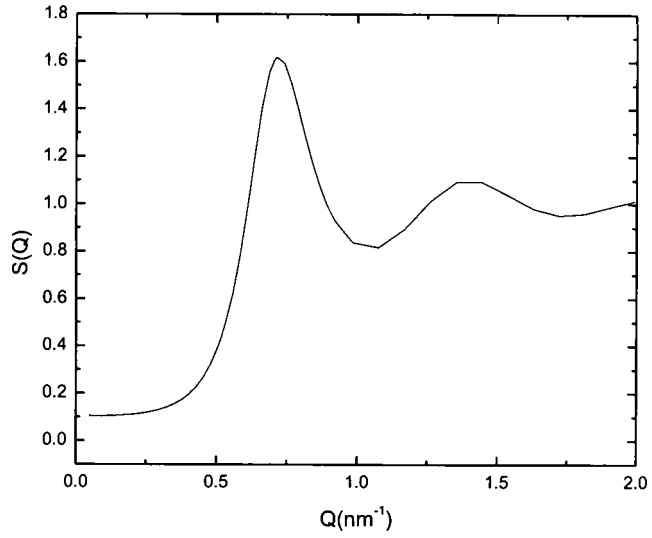

Figure 7.7.6: Calculated Percus-Yevick structure factor.

Figure 7.7.7 shows the magnetic scattering B(Q) from the Co nanoparticles for the scattering cross-section $I^{+}+I^{-}$. The data were modelled using the same method employed for the structural data. As expected, all the parameters stay the same, with the only change being the size distribution increase slightly from 0.13 to 0.21 and the scattering length density for the matrix and the shell reduced very close to zero as neither cobalt oxide nor the organic material give rise to any magnetic scattering. Therefore, the magnetic scattering observed is predominantly due to the 4.0±0.2nm magnetic core. Figure 7.7.7 also shows the scattering cross-section for $I^{+}-I^{-}$. The line through the data points is calculated using (3.1.4.21) together with $F_N(Q)$ and $F_M(Q)$ obtained from the modelling of A(Q) and B(Q). The result suggests that the structural and magnetic form factors are highly correlated. The fact that it is necessary to reproduce the scattering from the structural, magnetic and cross terms, which are all different, means that it is possible to further constrain the model.

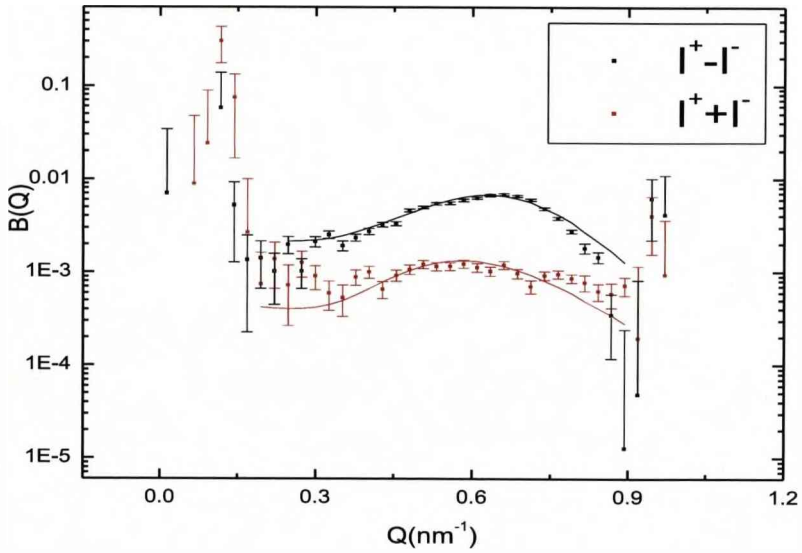

Figure 7.7.7: Magnetic scattering from the Co nanoparticle system, the lines through the data points are best fits to a close packed polydisperse core-shell particle model.

Fe_2O_3 nanoparticles

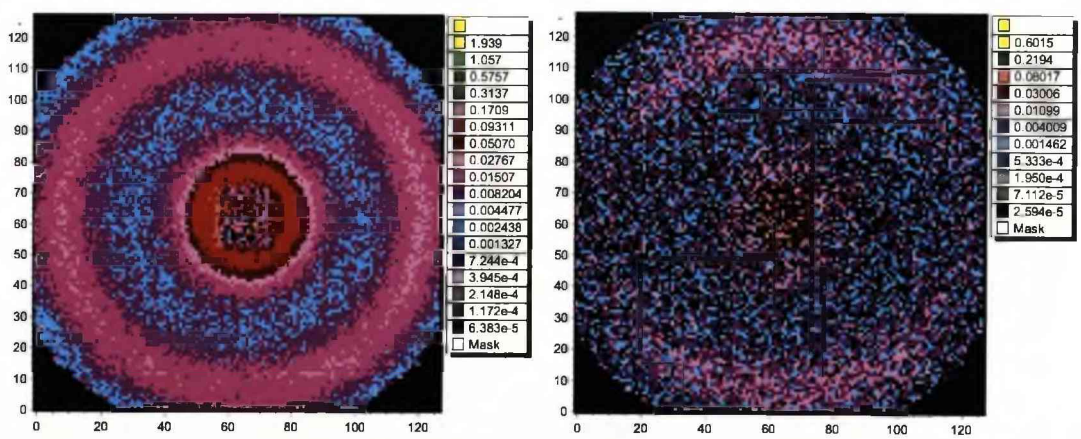

Figure 7.6.8: SANSPoL from a Fe_2O_3 nanoparticle sample with a 1.1T applied field, plots show 2D data after correction for transmission and background. Left is the sum of the SANSPoL with flipper on and off, right is the difference between flipper on and off.

Figure 7.6.8 shows the 2D SANSPoL for Fe_2O_3 nanoparticles under a 1.1T applied field, on the left is the sum of the scattering intensity for both incident neutron polarisations and on the right is the difference in scattering intensity between the two spin states. The data were reduced in exactly the same way as described above for Co and the 1D data are shown in figure 7.6.9 and figure 7.6.10. Lines through data points are fits to data using the core nanoparticle model with a Percus-Yevick distribution. Note that one of the simplifying features of this system is that, since it is already an oxide, it will not have an oxide shell. From the structural scattering A(Q) the core size of the nanoparticle is 4.3±0.1nm in radius with a packing fraction of 0.49±0.2. Unfortunately due to the small signal we were unable to extract B(Q) from the $I^+ + I^-$ scattering. However, $I^+ - I^-$ scattering data shows a clear result with the core size estimated to be 4.4±0.2nm in radius, and the packing faction of 0.49, ±0.2. Thus the model for the magnetic scattering agrees with the structural scattering within experimental uncertainty. The fact that the $I^+ - I^-$ cross-section is almost identical to $F_N(Q)^2$ suggests that the structural and magnetic form factors are almost perfectly correlated. Thus, when magnetic signals are too small to detect using unpolarised neutrons, SANSPoL offers an excellent opportunity to gain information on the magnetic nanostructures.

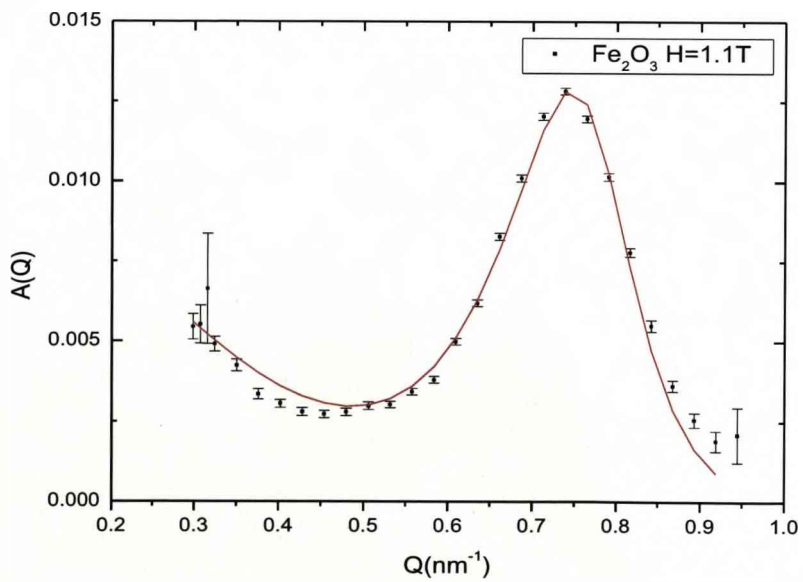

Figure 7.6.9: Structural scattering from the Fe_2O_3 nanoparticle system, the line through the data points is the best fit to a close packed polydisperse particle model.

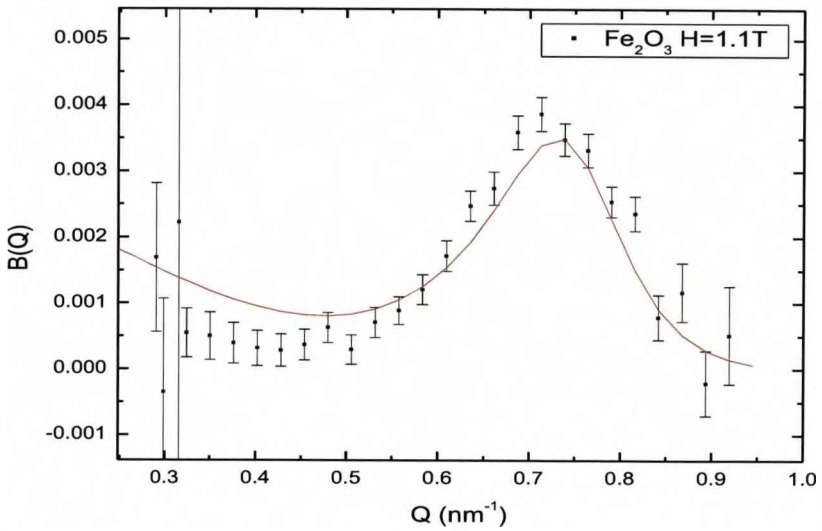

Figure 7.6.10: Magnetic scattering from the Fe_2O_3 nanoparticle system, the line through the data points is the best fit to a close packed polydisperse particle model.

7.8 Discussion

One of the aims in this chapter was to investigate the effect on the SANS of interparticle interactions. In order to reproduce the observed scattering an interparticle structure factor is required in each case. For the Co nanoparticles the use of self-assembly techniques produces arrays that look hexagonally ordered over small areas in TEM images. It is, therefore, rather surprising that it is possible to fit the data with a Percus-Yevick distribution that simply avoids overlap of hard spheres. Thus the conditions for long-range order are rather more stringent than expected.

The use of SANSPoL is found to be highly effective and leads to two main advantages over unpolarised SANS. First, in addition to the pure structural and magnetic terms obtained from unpolarised measurements, the difference data give information on the structural-magnetic cross term, giving a more stringent test of the theoretical model. Secondly, for weakly magnetic systems like the Fe_2O_3 nanoparticles, where it is difficult to resolve the magnetic component using unpolarised neutrons, the much greater sensitivity of the difference data makes it much easier to detect a magnetic signal. Even though this signal is combined with the

structural cross section, it still yields useful data for comparison with models of the magnetic order.

The TEM measurements of the two nanoparticle systems have revealed that the size of the Co and Fe_2O_3 nanoparticles are 4.1nm and 4.4nm, respectively. Studies using SANSPoL gives reasonable agreement with the TEM results and detailed modelling of the SANSPoL data suggests that the Co nanoparticles have a more complex structure than the Fe_2O_3 nanoparticles. The magnetic structure of Co nanoparticles consists of a magnetic core and a nonmagnetic shell, whereas the Fe_2O_3 nanoparticles only have a single magnetic core. Although the nanoparticles have a similar magnetic core size they are shown to have very different blocking temperatures. Co nanoparticles have a blocking temperature of 235K whereas Fe_2O_3 nanoparticles only have a blocking temperature of 75K. They also behave very differently when cooled under a field. Co nanoparticles exhibit an exchange-bias effect, but none was observed for Fe_2O_3 nanoparticles. This exchange-bias in the Co nanoparticles provides an explanation for the higher than expected thermal stability for the Co nanoparticles. The effect of exchange biasing most likely comes from the interaction between the Co core and its shell. The shell consists partly of cobalt oxide. Since Fe_2O_3 nanoparticles do not form an AF shell when they come in contact with the atmosphere, they do not exhibit an exchange-bias effect at all.

It is interesting to finish the discussion with a note on the Co nanoparticle system. The behaviour of this system is very similar to the Co-CoO/Ag system studied in the previous chapter, the only difference being that the Co-CoO/Ag system has Co nanoparticles embedded in a matrix with CoO and Co impurity. A question that naturally arises is whether the CoO shell or the matrix is the main contributing factor for the exchange-bias effect. Here we have removed the complex matrix and showed that exchange biasing can be observed with just a Co nanoparticle core and its cobalt oxide shell. The exchange bias field observed here, about 2000Oe, is comparable to the 3000Oe found in Co-CoO/Ag in the previous chapter. This suggests that the CoO shell is most likely to be the dominating factor for exchange biasing in Co nanoparticle systems.

7.9 Conclusions

SANSPoL is found to be very useful in studying magnetic nanostructures. In common with unpolarised SANS, it enables the interparticle correlations to be studied in much more detail than TEM. The more sophisticated statistical averaging of this technique, suggests that caution should be used when extrapolating promising ordering is TEM images to longer range. The use of polarised neutrons allows further constraint of the model, and in the case of Fe_2O_3 nanoparticles, provides the only means to see a magnetic signal at all. SANSPoL shows that the Co and the Fe_2O_3 particles have a similar size, 4.1nm and 4.4nm in radius, respectively. However, their magnetic response is very different. Field-cooled measurements of Co nanoparticles show a blocking temperature of 235K, whereas Fe_2O_3 particles only have a blocking temperature of 75K. Furthermore exchange bias was observed for Co nanoparticles, but not for Fe_2O_3 nanoparticles. This result suggests that the AF shell of the Co nanoparticles provides extra anisotropy to stabilise Co nanoparticles from thermal excitation. Finally, by comparing the result here with the result obtained for Co-CoO/Ag in the previous chapter, we have found that the exchange bias effect is predominantly due to the FM-AF core-shell structure of the Co nanoparticles.

Bibliography

[1] L. Del Bianco, D. Fiorani, A.M. Testa, E.Bonetti, L.Signorini. Phys. Rev. B 70 052401 (2004)

[2] J. Nogues J, and I.K. Schuller. Magn. Magn. mater. 192, 203 (1999)

[3] V. Skumryev, S. Stoyanov, Y. Zhang, G. Hadjipanayis, D. Givord, and J. Noguacs, Nature (London) 423, 850 (2003)

[4] V. Kurlyandskaya, M. L. Sanchez, B. Hernando, V. M. Prida, P. Gorria and M. Tejedor, App Phys. Lett. 82, 3053 (2003)

[5] F. Scherer et al., Gene Ther. 9, 102 (2002)

[6] K. Liu, Shenda M. Baker, Mark Tuominen, Thomas P. Russell, and Ivan K. Schuller. Phys. Rev B 63 060403 (2001)

[7] I. Robinson, C Alexander, Le T.Lu, Le D. Tung, D G. Fernig, and N.T.K Thanh, Chem. Commun., 2007, 4602-4604 (2007)

[8] Nguyen T.K. Thanh, V. F Puntes, Le D Tung and D G Fernig. JoP Conference series 17 (2005) 70-76.

[9] http://rsb.info.nih.gov/ij/

[10] http://www.hmi.de/bereiche/SF/SF3/arbeitsg/nanomaterialien/bersans_en.html

[11] A Wiedenmann, Physica B 297 (2001) 226-233

[12] W.L Griffith, R Triolo, and A. L Compere, Phys Review A 33 3 (1985)

[13] W.L Griffith, R Triolo, and A. L Compere, Phys Review A 35 5 (1986)

Chapter 8

Conclusions

The work presented in this thesis made use of a combination of x-ray and neutron scattering, TEM and magnetometry to study the magnetic structures and interactions in different nanoscale magnetic systems. This section summarizes the findings of the previous chapters and indicates how these studies may be extended.

X-ray diffraction and TEM studies of Fe/MgO multilayer concluded that the structural interfaces between Fe and MgO are atomically sharp. However, the structural coherence is confined within two bilayers. This low structural coherence is due to a wavy roughness, which also results in a substantial variation in the barrier thickness. Furthermore, PNR results show that for thick MgO layers (20Å) the system forms a coherent FM coupled structure. In contrast, thinner MgO layers (6Å) give no magnetic correlation in the virgin state, but show frozen in FM moments when returned to the coercive state. The finding of FM interactions in both virgin and coercive states is an important one, as this will limit the maximum attainable TMR.

Details of the magnetic order of Co/Ag nanoparticle were obtained using SANS, and the chemical structure using x-ray diffraction. The data provide an explanation for the complex GMR dependence on annealing temperature. The dependence arises from a phase separation between the Co nanoparticle core and the Ag matrix for annealing temperatures below 300°C, followed by agglomeration of particles at higher annealing temperatures.

The exchange-biased nanoparticle system, Co-CoO/Ag, was also examined. We have studied the change in the magnetic structure of the Co nanoparticles after different levels of oxidation, and its effect on the nanoparticle blocking temperature. We found that oxidation first reduces interactions between particles due to the removal of FM Co impurities in the matrix. This reduces the RKKY-like interactions, resulting in a small drop in blocking temperature. Then, once the CoO shell reaches a

critical thickness, exchange bias takes over and a sharp increase in blocking temperature was observed.

Ordered nanoparticle arrays were studied using TEM and SANSPoL. TEM pictures show self-assembled nanoparticles form small clusters of ordered arrays. However, in all cases the SANSPoL data can be modelled using a hard-sphere Percus-Yevick model, indicating only short-range order. Furthermore, exchange bias was observed for uncontrolled oxidation of Co nanoparticles and an increase in magnetic anisotropy due to the AF CoO shell was detected. In contrast, Fe_2O_3 nanoparticles of the similar size were also studied where no AF shell can be from by oxidation and, as a result, no exchange biasing was detected.

Many of these studies can be extended, in particular the study of TMR junctions. It would be interesting to investigate the change in the coupling strength as a function of MgO thickness and correlate that with structural details such as interfacial roughness, especially for thin MgO layers where both AF and FM coupling co-exist within the system. In the ideal case if a coherent AF structure could be obtained, Fe/MgO multilayer could be the most natural way of combining two or more TMR junctions together, therefore substantially increase the TMR ratio for potential applications.

It would be interesting to find out whether the loss of crystalline coherence is a general feature of multilayers very different out-of-plane lattice parameters. The materials used for the magnetic component could be varied to cobalt or permalloy, or a different oxide barrier could be used such as sapphire.

For the two Co/Ag nanogranular systems it would also be interesting to perform field dependent SANS measurements, as the change in the spin-misalignments scattering should provides more detailed information on the magnetic matrix as well as the particles.

The studies of nanoparticle systems illustrated that the magnetic structure of rather messy systems, like the Co/Ag nanogranular systems can be obtained by SANS. This is very encouraging as some of the new nanoscale magnetic devices are highly ordered and structurally much less complex than the nanogranular system. If the self-assembly techniques could be improved to give more ordered structures, it might be possible to determine how magnetic interactions change in the cross-over region from two-dimensional to three-dimensional structures.